UNIVERSITÀ DEGLI STUDI DI CAGLIARI

DOTTORATO DI RICERCA IN FISICA
Ciclo XXIV

First Principle Description of Correlated Transition-Metal Oxides

Settore scientifico disciplinare di afferenza
FIS/03 Fisica della Materia

Presentata da:	Danilo Puggioni
Coordinatore Dottorato:	Prof. G. Bongiovanni
Relatori:	Prof. V. Fiorentini e Dr. A. Filippetti

Esame finale anno accademico 2010-2011

First Principle Description of Correlated Transition-Metal Oxides

Danilo Puggioni

Anno Accademico 2010/2011

A Cinzia, mia madre e mio padre che mi guarda dal cielo

Acknowledgements

This work has been supported by MiUR through project PON-Cybersar and by the EU through projects ATHENA and OXIDES. Calculations were performed on CASPUR (Rome) and Cybersar clusters.

I would like to sincerely thank Prof. Vincenzo Fiorentini and Dr. Alessio Filippetti for their continuous support, motivation and interested attention during these years. Special thanks go to Pietro Delugas, Giuseppe Colizzi, Giorgia Lopez and Marco Scarrozza for their useful suggestions. I would like to acknowledge all the co-authors of scientific papers related to present thesis work.

Contents

List of Figures

List of Tables

Introduction & Scope

The word correlation appears for the first time in a book by Francis Galton (Hereditary Genius, 1869 [1]), without being further defined ("the characteristic of strong morality and moral instability are in no way correlated"). Although the term is relatively new correlations of various type have always been an integral part of human life. Typical examples of correlation are for example the dependence between the color of the eyes of offspring and their parents (and in general all the hereditary traits), the relationship between income and education, or simply traffic jams. From the mathematical point of view the correlation is a causal, complementary, parallel, or reciprocal relationship, especially a structural, functional, or qualitative correspondence between two comparable entities.

In the case of solid state physics, for two independent electrons we have that the probability density of finding the first electron at $\mathbf{r}$ and the second electron at $\mathbf{r}'$ is

$$\langle \hat{\rho}(\mathbf{r})\hat{\rho}(\mathbf{r}')\rangle = \langle \hat{\rho}(\mathbf{r})\rangle\langle \hat{\rho}(\mathbf{r}')\rangle \tag{1}$$

where $\hat{\rho}(\mathbf{r})$ is the electron density operator and the outer brackets express the expectation value of the operator. If these two electrons are correlated, then the probability of finding the first electron at a certain position in space depends on the position of the second electron, and vice versa. In other words, the product of their independent density functions does not describe correctly the real situation:

$$\langle \hat{\rho}(\mathbf{r})\hat{\rho}(\mathbf{r}')\rangle \neq \langle \hat{\rho}(\mathbf{r})\rangle\langle \hat{\rho}(\mathbf{r}')\rangle \tag{2}$$

We can say that the uncorrelated electrons tend to avoid each other or in the same way that at large distances, the uncorrelated pair density is too small, and at small distances, the uncorrelated pair density is too large.

Introduction & Scope

This thesis attempts to explain the behavior of some strongly correlated[1] materials from first principles. Correlated compounds have attracted much attention in the last decades. The reason for their popularity is due to their rich and exotic phenomenology such as charge / orbital / magnetic ordering; strong Jahn-Teller effects; high T_c superconductivity, polaronic phenomena, multiferroicity etc.

From 1963 (when Hubbard introduced his Hamiltonian for the description of correlation effects in *d*- and *f*-bands [2]) to the present day, research has made great strides, theoretically as well as experimentally. Modern spectroscopy techniques like x-ray absorption, spectroscopy angular resolved photoemission spectroscopy (ARPES), neutron scattering experiments, measurements of the optical conductivity or more advanced ellipsometry, various microscopy techniques, and many more related approaches or combinations of them provide data which must be interpreted and understood by means of reliable theoretical calculations. In this thesis, in order to obtain realistic data, we propose and develop a new methodology (Pseudo-Self-Interaction Correction [3, 4, 5]) that proves to be a reliable and accurate theoretical tool.

We point out that the increasing knowledge about correlated systems from the theoretical point of view offers the possibility of designing materials according to our needs. On the other hand, this requires the development of theoretical techniques that can capture the essence of the new experimental data produced.

The remainder of this thesis is organized as follow:

- In the first chapter of this thesis we discuss the PSIC approach, and present the new Variational Pseudo-Self-Interaction formulation (VPSIC).

- Chapter two is devoted to cuprates. In particular we will approach the problem of Shubnikov-de Haas (SdH) and de Haas-van Alphen (dHvA) quantum oscillation observed in mildly underdoped ($\sim$0.1 holes per CuO_2 unit) ortho-II $YBa_2Cu_3O_{6.5}$ based on band structure calculations. We will suggest that the experimentally observed pockets are a characteristic of some form of ordering (probably magnetic) causing a Fermi surface reconstruction.

---

[1] We use the term "strongly correlated" to describe systems whose electron charge retains atomic-like features such as strong space localization, poorly dispersed band energies, and large on-site Coulomb energies.

In the following, starting from a recent experiment [6], we will clarify theoretically the properties of a possible stable structures of bulk rocksalt-like CuO.

- In chapter three we will test the new VPSIC formalism on the electronic and structural properties of the magnetic perovskites $YTiO_3$ and $LaTiO_3$. We show that the new approach furnishes a coherent guideline to understand the differences between $YTiO_3$ and $LaTiO_3$, and correctly describes their different magnetic ordering of the two systems.
- In chapter four we will present a detailed theoretical analysis of MnO and NiO magnetic properties under hydrostatic pressures, carried out by an array of both standard (LDA and PBE) and advanced first-principles methods (VPSIC and the Heyd, Scuseria and Ernzerhof (HSE) hybrid functional approach). We will show that the results provided by VPSIC and HSE are quite satisfying and explain experimental data.
- The last chapter of this thesis is divided in two parts:
    - In the first part of the chapter we will approach the problem of charge disproportion in *ab inito* calculation. We analyze the charge imbalance in the double perovskite La_2NiMnO_6, where Ni is nominally 2+ and Mn nominally 4+, using different methodologies such as partial DOS integration, Bader analysis, etc. Our results confirm that quantifying the charge transfer unambiguously is tricky.
    - In the second part we will analyze the possibility of finding a nickel based heterostructure with properties similar to cuprate. Specifically with our VPSIC calculations we will focus on the 1/1 layered system $LaAlO_3/LaNiO_3$ for which we find the desired cuprate like Fermi surface structure in the paramagnetic state. However, we find that the system has an antiferromagnetic metallic ground state. Our results clarify the origin of the peculiar properties of $LaAlO_3/LaNiO_3$ superlattices.

1

Pseudo-self-interaction correction

The local (spin) density (LDA, LSDA) to density functional theory (DFT) has allowed accurate first-principles simulations for several decades, and provided a deep understanding of many condensed matter systems. Although the successes of LDA and LSDA are innumerable, there are cases where these approximations fail systematically, in particular in magnetic and strongly correlated systems.

Typical examples of LSDA failures (or severe difficulties) are the series of transition-metal monoxides [7], improperly described in LSDA as either small-gap exchange-antiferromagnetic insulators [8, 9] (MnO, NiO) or even ferromagnetic and nonmagnetic metals (FeO, CoO, CuO) [8, 10] whereas according to experiments these materials are charge-transfer antiferromagnetic wide-gap insulators. A similar situation occurs for the high-T_c parent compounds La_2CuO_4 and $YBa_2Cu_3O_6$ which in LSDA are nonmagnetic metals rather than antiferromagnetic insulators [11] and for the perovskite manganites (e.g., $La_xCa_{1-x}MnO_3$) [11, 12] for which the LSDA fails to predict the correct magnetic and orbital orderings. In general, LSDA favors metallic and ferromagnetic ground states over the observed antiferromagnetic insulating ground states. This is particularly harmful in the case of hexagonal $YMnO_3$, which is antiferromagnetic and ferroelectric, but is described as a metal within LSDA [13], thus preventing the possibility of calculating any ferroelectric properties at all.

One, though not the only, reason for these failures is that the approximate exchange-correlation functional contains a residual electron self-interaction (SI), not canceling out as it does in Hartree Fock, for example. This effect is marginal in many cases, but it can be dramatic for $3d$ and even $2p$ states, which are very localized near atomic nuclei.

One consequence is that LSDA overestimates electron delocalization to reduce the self-interaction (SI) repulsion, and in some cases converts what should be an insulator into a metal. More generally, it can be said that the SI adulterates, and exaggerates, the on-site repulsion. There are several techniques that attempt to correct this effect, such as L(S)DA+U [14] or Hybrid-functionals [15], but in this context we consider the Pseudo-Self-Interaction Correction (PSIC) [3, 4].

This chapter is organized as follow: in Sec.1.1 we show the origin of SI in LSDA, in Sec.1.1.1 we discuss the influence of SI on the band-theory description of strongly correlated materials, in Sec.1.2 we review the main features of earlier work on Self-Interaction Correction (SIC) implementation in LSDA, in Sec.1.3 We describe the PSIC formulation and in Sec.1.4 we describe the new variational PSIC approach.

1.1 LSDA and self-interaction

In the LSDA approach the electron energy (i.e. Hartree plus exchange-correlation) $E_{hxc}[n(\mathbf{r})]$, and the single-particle effective potential $V_{hxc}[n(\mathbf{r})]$ depend solely upon the local value of the electron density. This assumption allows the practical study of many-body system with a remarkable reduction of the computational effort and makes practicable the formulation and the algorithmic coding of the most disparate physical properties which can be determined in a self-consistent manner. On the other hand, the local dependence on the single-particle electron density entails a SI, i.e. the interaction of a particle with its self-generated potential. The SI can be quantitatively determined [16], and the expression of the screening potential is

$$\begin{aligned} V_{hxc}(\mathbf{r}) = \quad & \sum_{i=1}^{N-1} \int d\mathbf{r}' \frac{|\psi_i(\mathbf{r}')|^2}{|\mathbf{r}-\mathbf{r}'|} + V_{xc}[n(\mathbf{r})] - V_{xc}[n_N(\mathbf{r})] + \\ & + f_N \int d\mathbf{r}' \frac{|\psi_N(\mathbf{r}')|^2}{|\mathbf{r}-\mathbf{r}'|} + V_{xc}[n_N(\mathbf{r})], \end{aligned} \tag{1.1}$$

where the third term and the fourth term on the right hand are the Hartree and exchange-correlation SI contributions of the N_{th} particle, and $n_N(\mathbf{r}) = f_N|\psi(\mathbf{r})|^2$ is the charge density and f_N the orbital occupation of the same particle. The Hartree SI depends linearly on f_N and dominates the LSDA $V_{xc}[n(\mathbf{r})] \sim n_N^{1/3}$. At this point we can define the SI to the LSDA energy functional contribution as:

$$E^{SI} = \sum_i E_{hxc}[n_i(\mathbf{r})], \tag{1.2}$$

where $E_{hxc}[n_i(\mathbf{r})]$ is the Hartree plus exchange-correlation energy of orbital i. This is certainly one of the major weaknesses of LSDA potential.

We note that the presence of SI is due to the local dependence of the electron density. Indeed in any exact-exchange theory, for example Hartree Fock, self-exchange counterbalances the Hartree contribution.

1.1.1 Self-interaction and strong correlated materials

The presence of self-interaction in the LSDA is a major cause of the incorrect description of strongly correlated materials. LSDA is usually regarded as an uncorrelated theory; however, the LSDA energy and effective potential include correlation, although in an approximate local form. As a matter of fact, for a free atom, we can compare the contribution of the correlation energy, which can be isolated from other energy contributions, with experiment. In this way [17, 18, 19] it was shown that the magnitude of the exchange is underestimated by 10-15% in LSDA while the magnitude of the correlation energy is overestimated by as much 100-200%. Luckily, for properties connected to total energy changes (such as e.g. the first atomic ionization potential potential [18]) these two errors compensate each other and LSDA produces results in good agreement with the experiments. Unfortunately, error cancellation is not as good in the screening potential. Indeed the diagonal part of the Hartree potential is markedly greater than the local exchange, and this results in a SI contribution which causes a difference between measured electronic removal energy and LSDA eigenvalue.

1.2 Previous Work

In this section, as anticipated, we review briefly the main features of earlier work on SIC implementation in LSDA.

1.2.1 PZ-SIC

A key contribution is that by Perdew and Zunger [17, 20]. Their SIC recipe is quite simple: subtract the SI contribution from the total LSDA energy functional E^{LSDA}. In this way they recover a good agreement between photoemission data and eigenvalues, although there is no exact relation of eigenvalues and extraction energies. This approach, hereinafter referred to as PZ-SIC, for free atoms takes the form

$$E^{SIC}[n] = E^{LSDA}[n] - \sum_i (E_h[n_i] + E_{xc}^{LSDA}[n_i]), \tag{1.3}$$

where $i = n, l, m, \sigma$ is a collective index for the atomic quantum numbers, and the (spin-polarization dependent) exchange-correlation energy is referred to the fully polarized state. Applying the Kohn-Sham minimization to eq.(1.3) we obtain a nearly SI-free single-particle for particle i

$$V^{SIC}[n, n_i] = V^{LSDA}[n] - V_h[n_i] - V_{xc}^{LSDA}[n_i]. \tag{1.4}$$

Indeed, the potential V^{SIC} still contains a residual contribution of SI due to the non-linear dependence of the exchange-correlation on the charge density.

In the case of extended systems (i.e. where we assume a Bloch view) in which electronic charge is delocalized in the system and cannot be associated with a specific ion, except for some special cases (e.g. molecular solids), the behavior of PZ-SIC undergoes a radical change. The extension of the PZ-SIC formulation to extended systems was accomplished by different approaches, for example by implementing the method in the LMTO (linear-muffin-tin-orbital) basis [21, 22, 23], as well as in the ASA (atomic sphere approximation) [24, 25], or using the properties of Wannier functions [26, 27, 28]. In general, whatever the specific strategy, PZ-SIC tends to enhance the charge localization and leads to an overcorrection of single-particle energies with respect to their LSDA energies. This is because the energy stabilization induced by the SI potential in the PZ form is so strong that the electronic charges generally evolves in order to maximize their localization, with the effect that any localized charge configuration is always at least a local minimum of the PZ-SIC functional. Configurations with delocalized Bloch states (e.g. the O p states in manganites) at lower energies [21] seem to occur due to the artificially enforced spherical approximation, rather than to the ability of the PZ-SIC functional to detect the correct electronic ground state.

1.2.2 VKP approach

In the PSIC the SI is parameterized in terms of its atomic counterparts. With this approach the Bloch's vision is completely preserved, and it is assumed that some degree of localization, and thus an “effective” SI, is present in the Bloch states and must be removed. In 1996 Vogel, Krüger and Pollmann [29] (VKP-PSIC) suggested to extract the SI contribution from the band energies of wide-gap (III-V and II-VI) insulators exploiting the pseudo-potential (PP) formalism. They modified the usual PP generation procedure to include the angular moment-dependent atomic SI into each PP projector, making it SI-free by construction:

$$V_l^{pSIC}(r) = V_l^{PS}(r) - V_H[n_l(r)] - V_{xc}^{LSD}[n_l(r)], \tag{1.5}$$

where V_l^{PS} is the ion-core PP (minus a long-range local part which is treated separately), and the other terms are the atomic SI for angular moment l (only l-dependence survives because the radial symmetry is assumed), and $n_l = |\phi_l|^2$ is the corresponding atomic charge. Using the Kleinman-Bylander [30] (KB) form the PP projector acting on Bloch states takes the form

$$\hat{V}^{pSIC} = \sum_l \frac{|V^{pSIC}\phi_l\rangle\langle\phi_l V_l^{pSIC}|}{\langle\phi_l|V_l^{pSIC}|\phi_l\rangle}. \tag{1.6}$$

SIC projectors are typically short-ranged, so the correction is fairly localized around the ion core and can be treated by conventional plane wave codes without additional difficulties. The VKP-PSIC approach improves the agreement between experimental excitations and computed band energies for a series of wide-gap semiconductors [29, 31, 32]. To understand the reason for this success we analyze the specific case of bulk ZnO. The valence bands have a well-defined atomic-angular character and each of them (Zn 3s, 3p, 3d, and O 2s, 2p) is purged of its own atomic self-interaction, in agreement to eq.(1.6). This assumption works quite well for II-IV wide-gaps. In the general case the bands with a dominant angular character are subject to a smaller SI than the corresponding orbitals in the free atom, for various reasons:

- charge spreading dilutes the effects of SI
- bands with a well-defined orbital character are rare, and hybridization among different atomic states is common
- regardless of their occupation and degree of localization, all bands (high localized Zn 3d, and O 2s, moderately localized O 2p and weakly localized Zn 3s, 3p are corrected by the full atomic SI. This, obviously, is questionable because SI should vanish for empty states

Based on these considerations it follows that the approach VKP-PSIC is applicable only to a limited number of cases.

1.3 Pseudo-SIC formulation

Filippetti and Spaldin [3] developed an approach that extends the applicability of VKP to a large variety of cases, particularly useful for strongly correlated materials. The key concepts of this generalization are:

- the SI projector cannot be merely atomic, but must somehow depend on the specific chemical environment to effectively simulate the charge distribution of the real system;
- the approach should retain the advantages of LSDA, no explicit state dependence, locality of the effective single-particle potential and eigenstate invariance under unitary transformations;
- even the PP formalism, an atomic SI projector is a generally valid form that can be built and used in a single-particle scheme;
- just like in the ordinary PP formalism, the SIC projector must be transferable, and fixed once and for all for each atomic species.

From these concepts Filippetti and Spaldin proposed the following KB-type PSIC projector:

$$\hat{V}^{\sigma}_{SIC} = \sum_{i} \frac{|\Upsilon^{\sigma}_{i}\rangle\langle\Upsilon^{\sigma}_{i}|}{C^{\sigma}_{i}} \tag{1.7}$$

where

$$\Upsilon^{\sigma}_{i}(r) = V^{\sigma}_{HXC}[n^{\sigma}_{i}(r)]\phi_{i}(r) \tag{1.8}$$

is the usual KB projection function, but now with V^{σ}_{HXC} in place of the usual PP, and

$$C^{\sigma}_{i} = \langle\phi_{i}|V^{\sigma}_{HXC}[n^{\sigma}_{i}(r)]\phi_{i}\rangle \tag{1.9}$$

the normalization factor of the KB PP. The pseudo-SIC Kohn-Sham (KS) equations are

$$[-\nabla^{2} + \hat{V}_{PP} + \hat{V}^{\sigma}_{HXC} - \hat{V}^{\sigma}_{SIC}]|\psi^{\sigma}_{nk}\rangle = \epsilon^{\sigma}_{nk}|\psi^{\sigma}_{nk}\rangle, \tag{1.10}$$

where $\hat{V}_{PP}$ is the PP projector, and ϵ_{nk}^{σ} are the KS eigenvalues.

In the VKP approach $V_{HXC}^{\sigma}[n_i^{\sigma}(r)]$ is just the atomic potential of the i_{th} state at full occupation. Filippetti and Spaldin, instead, introduce in $V_{HXC}^{\sigma}[n_i^{\sigma}(r)]$ the dependence on the chemical environment writing

$$n_i^{\sigma}(r) = p_i^{\sigma}|\phi_i(r)|^2, \tag{1.11}$$

where ϕ_i is the atomic orbital. The occupation number p_i^{σ} can be calculated self-consistently as atomic orbital projections of the manifold of the occupied Bloch states:

$$p_i^{\sigma} = \sum_{nk} f_{nk}^{\sigma} \langle \psi_{nk}^{\sigma} | \phi_i \rangle \langle \phi_i | \psi_{nk}^{\sigma} \rangle, \tag{1.12}$$

where f_{nk}^{σ} are Fermi occupation number. For unoccupied state ($p_i^{\sigma} = 0$) and the KS equation reduce to that of LSDA. For fully occupied states (p_i^{σ}=1) the pSIC correction is completely atomic-like. In a nutshell the p_i^{σ}'s are localization parameters for the Bloch states. Of course the introduction of p_i^{σ} implies the recalculation of $V_{HXC}^{\sigma}[n_i^{\sigma}]$ at each cycle of self-consistency for each angular component and atom, resulting in an increase of the computational cost. In order to reduce the computational effort, the SI potential is assumed linearly dependent on the occupation numbers:

$$V_{HXC}^{\sigma}[n_i^{\sigma}] = p_i^{\sigma} V_{HXC}^{\sigma}[n_i^{\sigma}; p_i^{\sigma} = 1], \tag{1.13}$$

so that only the p_i^{σ} must be updated at each iteration of the self-consistency. The above equation implies that all states are corrected by the full atomic SI. This is of course unrealistic, as the SI will be screened to some extent by the environment. The full SI ($p_i \sim 1$) only applies in an atomic (or molecular) limit. There is a necessity to introduce an "orbital relaxation contribution". Filippetti and Spaldin [3] proposed an argument based on the Janak theorem [16]. In DFT the energy required to remove a fraction p of an electron from a localized state is [16, 17, 21]

$$\Delta E(p) = E(p) - E(0) = \int_{t=0}^{t=p} dt \epsilon(t) \tag{1.14}$$

where ϵ is the corresponding KS eigenvalue. In LSDA due to the dominance of the Hartree term we have: $\epsilon(p) \sim \epsilon(0) + p\delta\epsilon$, with $\delta\epsilon = \epsilon(1) - \epsilon(0)$. In PZ-SIC the linear dependence is largely (although not completely) canceled, and $\epsilon(p) \sim \epsilon(1)$. The associated relaxation energy that must be provided to the system to extract one electron from the single particle state is $\Delta E(1) = \epsilon(1)$. In PSIC, instead, only the atomic SI part (not the whole LSDA Hamiltonian) depends on orbital occupation, hence the energy relaxation associated to the SI survives and must be accounted for. Assuming a linear scaling of the SI potential, we get from equation 1.14

$$\Delta E^{SI}(1) = \epsilon^{SI}(0) + \frac{1}{2}\delta\epsilon^{SI} \tag{1.15}$$

Imposing $\epsilon^{SI}(0) = 0$, i.e. that the SI vanish at zero occupation, we have $\Delta E^{SI}(1) = \epsilon^{SI}/2$, i.e. the SI energy associated to the removal of one electron charge from the considered state is one half the atomic SI at full occupancy. This energy must be subtracted off the LSDA eigenvalue to compare it with some observed extraction energy. This is achieved by rescaling the SI as

$$V^{\sigma}_{HXC}[n^{\sigma}_i] \rightarrow \frac{1}{2}V^{\sigma}_{HXC}[n^{\sigma}_i] \tag{1.16}$$

1.3.1 Total energy

Filippetti and Spaldin use an expression for the total energy that is not related to Eq.(1.10) by a variational principle. (It is, by construction, within LSDA and PZ-SIC). In PZ-SIC the energy functional is [17]

$$E_{SIC}[n,m] = E[n,m] - \sum_{i,\sigma} E_{HXC}[n^{\sigma}_i] \tag{1.17}$$

where $E[n,m]$ is the LSDA energy functional and $E_{HXC}[n^{\sigma}_i]$ the Hartree exchange-correlation energy of the i_{th} fully spin-polarized electron charge

$$E_{HXC}[n^{\sigma}_i] = \int d\mathbf{r} n_i(\mathbf{r})(\frac{1}{2}V_H[n^{\sigma}_i(\mathbf{r})] + \mathcal{E}_{XC}[n^{\sigma}_i(\mathbf{r})]) \tag{1.18}$$

where V_H is the Hartree potential and $\mathcal{E}_{XC}$ is the local exchange-correlation energy density. For the pseudo-SIC total energy Filippetti and Spaldin adopt expression as Eqs.(1.17) and (1.18), with the orbital charges n^{σ}_i given by Eqs.(1.11) and (1.12). The Euler-Lagrange derivative of equation 1.18 yields

$$\frac{\delta E_{HXC}[n^{\sigma}_i]}{\delta \psi^{*\sigma}_{n\mathbf{k}}} = \frac{\delta E_{HXC}[n^{\sigma}_i]}{\delta p^{\sigma}_i}\frac{\delta p^{\sigma}_i}{\delta \psi^{*\sigma}_{n\mathbf{k}}} = f^{\sigma}_{n\mathbf{k}}|\phi_i\rangle C^{\sigma}_i\langle\phi_i|\psi^{\sigma}_{n\mathbf{k}}\rangle \tag{1.19}$$

where

$$\frac{\delta E_{HXC}[n^{\sigma}_i]}{\delta p^{\sigma}_i} = C^{\sigma}_i \tag{1.20}$$

represents the Janak theorem [16] applied to the SIC contribution, since C_i^σ (Eq.1.9) is the SI part of the atomic eigenvalue.

Is the non-variational character of the pSIC approach may be acceptable? The non-variationality in the logic of PSIC is entirely justified: while LSDA (or GGA) starts from a total energy functional, and the KS equations are formally only a device for functional minimization, the PSIC aim is to provide an accurate description of the electronic properties, and then, once single-particle energies and wavefunctions are in hand, to select an expression for the total energy. Without variationality, the total energy (Eq.1.17) is selected on the sole criterion of accuracy, which derives from the accuracy of the LSDA functional itself. In effect, the PSIC energy correction (second term of Eq.1.17) is a slowly-varying function of the Hamiltonian external parameters, to which it is only sensitive through smooth changes in the orbital occupations p_i. In practice, the most relevant physical trends are still dictated by the LSDA energy functional, now depending on eigenstates solutions of the PSIC-KS equations.

$$\begin{aligned} E_{SIC}[n,m] &= \sum_{i,\sigma} f^\sigma_{n\mathbf{k}} \epsilon^\sigma_{n\mathbf{k}} - \sum_\sigma \int d\mathbf{r} n^\sigma(\mathbf{r}) V^\sigma_{HXC}[n(\mathbf{r}),m(\mathbf{r})] \\ &+ E_{HXC}[n,m] + E_{ion} \\ &+ \frac{1}{2}\sum_{n\mathbf{k},\sigma} f^\sigma_{n\mathbf{k}} \langle \psi^\sigma_{n\mathbf{k}} | \hat{V}^\sigma_{SIC} | \psi^\sigma_{n\mathbf{k}} \rangle - \sum_{i,\sigma} E_{HXC}[n_i^\sigma] \end{aligned} \tag{1.21}$$

where E_{ion} is the usual Ewald term. $\sum_{i,\sigma} E_{HXC}[n_i^\sigma]$ produces a soft modification to the LSDA energy functional whereas the fifth term in Eq.(1.21) is a strongly varying contribution which compensates the same contribution present in the pseudo-SIC eigenvalues. Without this compensation, Eq.(1.21) would give very inaccurate total energies which would be unphysically far from the LSDA values as you can see in fig.

1.4 Variational pseudo-self-interaction formulation

In this Section we sketch the generic variational formulation [5], not related to any specific basis function implementation.

1.4.1 VPSIC energy functional and related Kohn-Sham equations

We start from the following VPSIC energy functional:

$$E^{VPSIC}[\{\psi\}] \;=\; E^{LSD}[\{\psi\}] - \frac{1}{2}\sum_{ij\nu\sigma} \mathcal{E}^{SI}_{ij\sigma\nu}\, P^{\sigma}_{ji\nu} \tag{1.22}$$

where E^{LSD} is the usual LSDA energy functional:

$$E^{LSD}[\{\psi\}] = T_s[\{\psi\}] + E_H[n] + E_{xc}[n_+, n_-] + E_{ion}[\{\psi\}]$$

written as sum of (non-interacting) kinetic (T_s), Hartree (E_H), exchange-correlation (E_{xc}), and electron-ion (E_{ion}) energies (ψ are single-particle wavefunctions, n_+ and n_- up- and down-polarized electron densities, and $n=n_+ + n_-$). Eq.(1.22) follows the spirit of the original PZ-SIC procedure[17], and subtracts from the LSDA total energy a SI term written as a sum of effective single-particle SI energies ($\mathcal{E}^{SI}$) rescaled by some orbital occupations P. Here i, j are sets (l_i,m_i, l_i,m_j) of atomic quantum numbers (typically relative to a minimal atomic wavefunction basis set) while σ and ν indicate spin and atomic site, respectively (non-diagonal formulation is necessary to enforce covariancy, thus i=(l_i,m_i), j=(l_i,m_j)).

Most of the peculiarity of the VPSIC approach resides in the way the second term of Eq.(1.22) is written for an extended system whose eigenfunctions are Bloch states ($\psi^{\sigma}_{n\mathbf{k}}$). The orbital occupations are then calculated as projection of Bloch states onto localized (atomic) orbitals (hereafter indicated as $\{\phi\}$):

$$P^{\sigma}_{ij\nu} = \sum_{n\mathbf{k}} f^{\sigma}_{n\mathbf{k}}\, \langle\psi^{\sigma}_{n\mathbf{k}}|\phi_{i,\nu}\rangle\, \langle\phi_{j,\nu}|\psi^{\sigma}_{n\mathbf{k}}\rangle, \tag{1.23}$$

where $f^{\sigma}_{n\mathbf{k}}$ are Fermi occupancies. For the effective SI energies we adopt a similar approach:

$$\mathcal{E}^{SI}_{ij\sigma\nu} \;=\; \sum_{n\mathbf{k}} f^{\sigma}_{n\mathbf{k}}\, \langle\psi^{\sigma}_{n\mathbf{k}}|\gamma_{i,\nu}\rangle C_{ij} \langle\, \gamma_{j,\nu}|\psi^{\sigma}_{n\mathbf{k}}\rangle \tag{1.24}$$

where $\gamma_{i,\nu}$ is the projection function associated to the SI potential of the i^{th} atomic orbital centered on atom ν:

$$\gamma_{i\nu}(\mathbf{r}-\mathbf{R}_\nu) \;=\; V_{Hxc}[n_{i\nu}(\mathbf{r}-\mathbf{R}_\nu), 0]\, \phi_{i\nu}(\mathbf{r}-\mathbf{R}_\nu), \tag{1.25}$$

where $n_{i\nu}(\mathbf{r})$=$\phi^2_{i\nu}(\mathbf{r})$. We can express the Hartree plus exchange-correlation atomic SI potential V_{Hxc} in radial approximation:

$$V_{Hxc} = V_H[n_{l_i\nu}] + V_{xc}[n_{l_i\nu}, 0] = \partial E_{Hxc}[n_{l_i\nu}]/\partial n_{l_i\nu} \tag{1.26}$$

(calculated at full polarization: n=n$_+$, n$_-$=0). Finally, the C_{ij} are normalization coefficients:

$$C^{-1}_{l_i,m_i,m_j} = \int d\mathbf{r}\, \phi_{l_i m_i}(\mathbf{r})\, V_{Hxc}[n_{l_i,\nu}(r), 0]\, \phi_{l_i m_j}(\mathbf{r}) \tag{1.27}$$

with l_i=l_j. They are purely atomic and do not depend on the atomic positions. The use of projectors γ in Eq.(1.24) is aimed at casting the SI energy in fully non-local form (analogous to the fully-non local pseudopotential form due to Kleinman and Bylander [30]) which consent a huge saving of computational effort when calculated in reciprocal space.

To grab the idea behind Equations 1.24, 1.25, and 1.27, notice that in the limit of large atomic separation, the Bloch states $\psi_{n\mathbf{k}}$ are brought back to atomic orbitals $\phi_{i\nu}$, and $\mathcal{E}^{SI}_{ij\sigma\nu}$ to atomic SI energies ϵ^{SI}_i (discarding spin and atomic index):

$$\epsilon^{SI}_i = \int d\mathbf{r}\, n_i(\mathbf{r})\, \left(V_H[n_i(\mathbf{r})] + V_{xc}[n_i(\mathbf{r}), 0]\right) \tag{1.28}$$

Thus, the orbital occupations $P^\sigma_{ij\nu}$ (if suitably normalized) act as scaling factors for the atomic SI energies, assumed as the upper limit of the SI correction amplitude.

We remark that in the atomic limit Eq.(1.22) goes back to the PZ-SIC total energy expression only for what concern the Hartree SI part, while our SI exchange-correlation energy density $(1/2)V_{xc}[n_i, 0]$ departs from the PZ-SIC expression $\epsilon_{xc}[n_i, 0]$, since $V_{xc} = \epsilon_{xc} + n_i \partial\epsilon_{xc}/\partial n_i$.

From Eq.(1.22) we can obtain the corresponding VPSIC Kohn-Sham equations through the usual Euler-Lagrange derivative:

$$\frac{\partial E^{VPSIC}}{\partial \psi^*_{nk\sigma}} = \tilde{\epsilon}_{nk\sigma}\, \psi_{nk\sigma}$$

$$= \hat{h}^{LSD}_\sigma \psi_{nk\sigma} - \frac{1}{2}\sum_{ij\nu} \left\{ \frac{\partial \mathcal{E}^{SI}_{ij\sigma\nu}}{\partial \psi^*_{nk\sigma}} P^\sigma_{ji\nu} + \mathcal{E}^{SI}_{ij\sigma\nu} \frac{\partial P^\sigma_{ji\nu}}{\partial \psi^*_{nk\sigma}} \right\} \tag{1.29}$$

where $\tilde{\epsilon}_{nk\sigma}$ are VPSIC eigenvalues, and;

$$\begin{aligned} h_\sigma^{LSD}(\mathbf{r}) &= -\frac{\nabla_\mathbf{r}^2}{2} \\ &+ V_H[n(\mathbf{r})] + V_{xc}[n_+(\mathbf{r}), n_-(\mathbf{r})] + V_{ion}(\mathbf{r}) \end{aligned} \tag{1.30}$$

is the usual KS LSDA Hamiltonian, and:

$$\frac{\partial \mathcal{E}_{ij\sigma\nu}^{SI}}{\partial \psi_{nk\sigma}^*} = |\gamma_{i,\nu}\rangle C_{ij\nu} \langle \gamma_{j,\nu}|\psi_{n\mathbf{k}}^\sigma\rangle; \tag{1.31}$$

$$\frac{\partial P_{ji\nu}^\sigma}{\partial \psi_{nk\sigma}^*} = |\phi_{j,\nu}\rangle \, \langle \phi_{i,\nu}|\psi_{n\mathbf{k}}^\sigma\rangle. \tag{1.32}$$

The first sum term in curly bracketsin Eq.(1.29) corresponds to the SI potential projector written as in the original PSIC Kohn-Sham equations. In practice they give similar results when applied onto the Bloch state. Thus Eq.(1.29) describes an energy spectrum substantially similar to that of the non-variational scheme, but with the added bonus of originating from the VPSIC energy functional.

In DFT methods it is customary to rewrite the total energy in terms of eigenvalue sums. Indicating with $\epsilon_{nk\sigma}$ the LSDA eigenvalues, it is immediate to verify that

$$\begin{aligned} \sum_{n\mathbf{k}\sigma} f_{n\mathbf{k}}^\sigma \, \tilde{\epsilon}_{nk\sigma} &= \sum_{n\mathbf{k}\sigma} f_{n\mathbf{k}}^\sigma \, \langle \psi_{n\mathbf{k}}^\sigma | \frac{\partial E^{VPSIC}}{\partial \psi_{nk\sigma}^*} \rangle \\ &= \sum_{n\mathbf{k}\sigma} f_{n\mathbf{k}}^\sigma \, \epsilon_{nk\sigma} - \sum_{ij\sigma\nu} \mathcal{E}_{ij\sigma\nu}^{SI} P_{ji\nu}^\sigma, \end{aligned} \tag{1.33}$$

Eq.(1.22) can then be rewritten as

$$E^{VPSIC}[\{\psi\}] = \tilde{E}^{LSD}[\{\psi\}] + \frac{1}{2} \sum_{ij\sigma\nu} \mathcal{E}_{ij\sigma\nu}^{SI} \, P_{ji\nu}^\sigma \tag{1.34}$$

where

$$\begin{aligned} \tilde{E}^{LSD}[\{\psi\}] &= \sum_{n\mathbf{k}\sigma} f_{n\mathbf{k}}^\sigma \, \tilde{\epsilon}_{nk\sigma} + E_{Hxc}[n_+(\mathbf{r}), n_-(\mathbf{r})] \\ &+ E_{ion} - \sum_\sigma \int d\mathbf{r} n_\sigma(\mathbf{r}) V_{Hxc}^\sigma[n_+(\mathbf{r}), n_-(\mathbf{r})] \end{aligned} \tag{1.35}$$

is the LSDA energy functional but now including the VPSIC eigenvalues in place of the LSDA eigenvalues. Finally, as in the original PSIC formulation the SI V_{Hxc} potential is rescaled by a relaxation factor α=1/2 accounting for screening (i.e. suppression) of the atomic self-interaction. A careful test on a large series of compounds [33] confirmed that this relaxation value is adequate for most extended bulk systems.

1.4.2 Simplified variants of VPSIC and relation with the original non-variational method

From the general espression of Eq.(1.22) two interesting subcases can be obtained: assumig fixed (i.e. non self-consistent) orbital occupations P_{ij}, in Eq.(1.29) the second term in curl brackets vanishes and the VPSIC-KS equations reduce to those of the original PSIC scheme of Ref.[3] (indeed, it was previously pointed out [4] that the original scheme becomes variational at fixed orbital occupations).

Another useful subcase is obtained replacing Eq.(1.24) with a simplified expression:

$$\mathcal{E}^{SI}_{ij\sigma\nu} = P^{\sigma}_{ij\nu}\epsilon^{SI}_{i\nu} = P^{\sigma}_{l_i m_i m_j \nu}\,\epsilon^{SI}_{l_i\nu} \tag{1.36}$$

where the atomic $\epsilon^{SI}_{l_i\nu}$ (in radial approximation) is given by Eq.(1.28). Using Eq.(1.36), previous Eqs.(1.22) and (1.29):

$$E^{VPSIC_0}[\{\psi\}] = E^{LSD}[\{\psi\}] - \frac{1}{2}\sum_{ij\nu\sigma} P^{\sigma}_{ij\nu}\,P^{\sigma}_{ji\nu}\,\epsilon^{SI}_{j\nu} \tag{1.37}$$

$$= \tilde{E}^{LSD}[\{\psi\}] + \frac{1}{2}\sum_{ij\nu\sigma} P^{\sigma}_{ij\nu}\,P^{\sigma}_{ji\nu}\,\epsilon^{SI}_{j\nu} \tag{1.38}$$

$$\frac{\partial E^{VPSIC_0}}{\partial\psi^*_{nk\sigma}} = \hat{h}^{LSD}_{\sigma}\psi_{nk\sigma} - \sum_{ij\nu} P^{\sigma}_{ij\nu}\frac{\partial P^{\sigma}_{ji\nu}}{\partial\psi^*_{nk\sigma}}\epsilon^{SI}_{j\nu} \tag{1.39}$$

This simplified VPSIC formalism (hereafter indicated as VPSIC$_0$) is a computationally convenient alternative (especially in terms of required memory) to perform structural optimizations in large systems. However it is tipically less accurate for magnetic systems.

1.4.3 Forces formulation

In VPSIC the atomic forces formulation follows from the usual Hellmann-Feynman procedure. It is obtained as the LSDA expression augmented by a further additive contribution due to the atomic-site dependence of the SI projectors:

$$-\frac{\partial E^{VPSIC}[\{\psi\}]}{\partial \mathbf{R}_\nu} = \mathbf{F}_\nu^{LSD} +$$

$$+\frac{1}{2}\sum_{ij,nk\sigma} f_{n\mathbf{k}}^{\sigma}\left\{\langle\psi_{n\mathbf{k}}^{\sigma}|\frac{\partial\gamma_{i,\nu}}{\partial\mathbf{R}_\nu}\rangle C_{ij}\langle\,\gamma_{j,\nu}|\psi_{n\mathbf{k}}^{\sigma}\rangle P_{ji\nu}^{\sigma}[\{\psi\}] + c.c.\right\}$$

$$+\frac{1}{2}\sum_{ij,nk\sigma} f_{n\mathbf{k}}^{\sigma}\left\{\mathcal{E}_{ij\sigma\nu}^{SI}[\{\psi\}]\,\langle\psi_{n\mathbf{k}}^{\sigma}|\frac{\partial\phi_{i,\nu}}{\partial\mathbf{R}_\nu}\rangle\langle\,\phi_{j,\nu}|\psi_{n\mathbf{k}}^{\sigma}\rangle + c.c\right\} \tag{1.40}$$

whereas in the simplified version, we have, in addition to $\mathbf{F}_\nu^{LSD}$ the quantity:

$$\sum_{ij,nk\sigma} f_{n\mathbf{k}}^{\sigma}\left\{P_{ij\nu}^{\sigma}\epsilon_{j\nu}^{SI}\,\langle\psi_{n\mathbf{k}}^{\sigma}|\frac{\partial\phi_{j,\nu}}{\partial\mathbf{R}_\nu}\rangle\langle\,\phi_{i,\nu}|\psi_{n\mathbf{k}}^{\sigma}\rangle + c.c\right\} \tag{1.41}$$

In writing Eqs.(1.40) and (1.41), we have assumed that the force on a given atom ν only depends on the single atomic projector centered on ν. This is not necessarily true if the orbital occupations are to be re-orthonormalized on the cell. This choice complicates appreciably the above formulation.

2

Cuprates

This chapter addresses some issues in relation to cuprates. In particular, in Sec.2.1 we approach the problem of quantum oscillations and in Sec.2.2 we study the electronic and magnetic properties of CuO in the rocksalt-structure.

2.1 Quantum oscillations

The main part of the following discussion is published in the APS Journal "Phys. Rev. B, 79(064519), 2009 [34]" and in the EPS Journal "EPL, 88(67009), 2009 [35]". The section about the non-magnetic phase of ortho-II $YBa_2Cu_3O_{6.5}$ *(Sec.2.1.3) was essentially my own work, or about 90% of the work. In the section about magnetic phase (Sec.2.1.4) my operational contribution was the calculation of the antiferromagnetic phase of* $Y_{1-x}Ca_xBa_2Cu_3O_6$ *(no spinless polarons), or about the 35% of the work. The writing and preparation of the papers was done collaboratively with coworkers and supervisors, as did the planning and assessment of the work.*

2.1.1 Introduction

The existence of a Fermi surface (FS) in underdoped high-T_c superconductors is attested by Shubnikov-de Haas (SdH) and de Haas-van Alphen (dHvA) quantum oscillation observed in mildly underdoped (∼0.1 holes per CuO_2 unit) *ortho*-II $YBa_2Cu_3O_{6.5}$ (henceforth YBCO; *ortho*-II stands for the chain-aligned oxygen configuration with one Cu(1)-O chain per 2×1×1 cell) and $YBa_2Cu_4O_8$ [36, 37, 38, 39, 40] and by angle-resolved photoemission (ARPES) [41, 42, 43, 44]

The oscillations (of resistance and Hall coefficient in SdH, and magnetization in dHvA) correspond to closed sections (pockets) of the FS and they exhibit, as a function of the inverse of the magnetic field, characteristic frequencies related to the cross-sectional area of the pocket (or pockets: their number and location is undetermined). The frequency measured by dHvA experiments (more accurate than SdH) is 540±4 T, corresponding to a small portion (2%) of the Brillouin zone being enclosed by the pockets. The cyclotron mass, deduced from a Lifshitz-Koshevic fit of the oscillation amplitude vs temperature, is m=1.76±0.07 free-electron masses. The oscillations were observed [36, 37, 38] in high field and only at low (4 K) temperature; the sign of the Hall coefficient was seen to become negative from about 25 K downward, and this was interpreted as a signature of the pockets in question being electron-like in nature. A further recent measurement [45] in $YBa_2Cu_3O_{6.51}$ reported, in addition to the same signal of Ref. [36], an oscillation with frequency and mass in the vicinity of 1600 T and 3.4 m_e respectively, allegedly (see Ref.[45], p.201) associated with a hole-like pocket.

On the other hand, angle-resolved photoemission (ARPES) [41, 42, 43, 44] observes large zone-corner-centered cylinders at optimal doping turning into disconnected hole-like arcs near nodal points upon underdoping.

The microscopic nature of the pockets is currently under intense debate. Several hypotheses have been formulated under the general category of a symmetry-breaking FS reconstruction, as suggested for “1/8” compounds [46], among which *d*-density-wave order [40], field-induced long-range magnetic order [47], short-range magnetic order [48, 49, 50], and magnetic polarons [51, 52, 53], but none of them has gained a general consensus yet. Magnetic correlations are popular candidates as, according to various experimental probes [54, 55, 56, 57, 58, 59], antiferromagnetic (AF) correlations coexist with, or survive into, the superconducting (SC) phase over a wide doping range.

A further problem is the discrepancy between SdH pockets and ARPES arcs, and their electron vs hole nature. It is usually supposed in Ockham’s razor fashion that the same single normal (i.e. non superconducting) phase is observed in oscillation and ARPES. Actually, this is far from obvious, because SdH/dHvA are done in high field at low T, and ARPES in zero field and high T. Thus, magnetic fluctuations possibly induced by the field may well be incommensurate, hence not amenable to short-wavelength periodic models. On the other hand, ARPES measurements may be affected by surface contributions or lack of resolution. These issues remarkably complicate the interpretation of the experiments, and even more so the possibility of reconciling their results (see Ref.[60] for a thorough discussion).

As already mentioned SdH and dHvA examine at low temperature a state obtained by applying a high magnetic field to the superconductor. To a first approximation this state is supposed to be the normal (possibly pseudo-gap) state. The simplest hypothesis is that once superconductivity is removed, YBCO is a metallic and non-magnetic Fermi-liquid like system (although more sophisticated options also exist, such as e.g. magnetic fluctuations and polaronic formations in stripe-like morphology [61] and more). Since experiments are often interpreted based on this assumption, an issue to be settled is whether or not the FS of this specific non-magnetic metallic phase exhibits pockets as revealed in experiments. At the same time the hints about the role of magnetism suggest a considerable scope for ab initio band-like quasiparticle calculations, accounting accurately for material-specific information, and for coupling to the lattice.

The remainder of this Section is organized as follow: Subsection 2.1.2 describes briefly the methodologies employed. In Subsection 2.1.3 we analyze the non-magnetic metallic phase of YBCO with three distinct techniques based on DFT: GGA (generalized gradient approximation), GGA+U, and PSIC. Furthermore, we adopt the common practice (discussed below) of applying rigid-band shifts to explore the FS in a wide energy interval surrounding the calculated E_F. Our calculation widen the scope of recent[62] calculations limited to the GGA approach. Our study shows that overall there is no reliable indication that non-magnetic metallic YBCO possesses electron-FS pockets. Specifically, only one technique (the GGA+U) finds an electron-like pocket, appearing however at a –60 meV shift away from calculated E_F. None of the other techniques find any such pocket in a ±100 meV interval around E_F. As we will argue, in fact, there is only scant evidence for hole-like pockets as well.

In Subsection 2.1.4 we present results for the FS of Ca-doped $Y_{1-x}Ca_xBa_2Cu_3O_6$ at hole doping h=x/2=0.125 (thus hole injection only involves CuO_2 planes, without the complicacies due to oxygen doping). In particular we focus on the AF ordering and two other polaronic configurations (as well as the Pauli paramagnetic (PM) phase as a reference) as possible candidate electronic ground-states states in an underdoped cuprate. Our results apparently do not solve the pockets vs. arcs contest, insofar as the calculated FS features partially agree, and partially disagree, with both the experiments. In fact, all the investigated magnetic states exhibit nodal pockets, with calculated areas not far from SdH experiments. However, the calculated pockets are hole-like, in contrast with oscillation results, but in agreement with the totality of ARPES measurements. This prevents an identification and leads us to conclude that the analyzed magnetic configurations are not those observed. We mention two possible solutions to this puzzle. First, as shown below, the FS properties are tied closely to the specific magnetic arrangement, so that different pocket areas and shapes, as well as, possibly, local curvature, will be associated with more complex magnetic correlations; e.g., Jahn-Teller bipolarons [52, 53] or spin-bag-like ferromagnetic polarons [63] (these structures are currently beyond the computational limits of our method, although some of them may become feasible in the near future). Second, the high magnetic field in SdH may produce a state influencing the FS in ways beyond the scope of zero-field calculations [47] such as, e.g. inducing incommensurate magnetic correlations. On the other hand, ARPES results are easier to reconcile with our results, e.g. considering arcs as product of configurationally averaged PM and AF phases. Beside these speculations, here we provide evidence that a first-principle theory can indeed describe the Mott phase of high-T_c compounds at low-doping, and establish a relation, grounded on realistic quantum-mechanical simulations, between magnetic ordering and the presence of small pockets at the FS of high-T_c superconductors.

2.1.2 Technicalities

We calculate the band structure of YBCO in the non-magnetic metallic state with three different DFT-based techniques. We use the GGA (generalized gradient approximation), GGA+U, and the pseudo-self-interaction correction method (PSIC) [3, 4] which correctly describes the physics of several correlated cuprates [64, 65, 66, 67, 68, 69]. In particular the PSIC is able to describe the competition of metallic and insulating phases of $YBa_2Cu_3O_{6+x}$ from x=0 (where it is [69] an antiferromagnetic Mott insulator) across two metal-insulator transitions [68] to metallic x=1, obviating to the failures of plain GGA or similar approaches in this context. Our GGA and GGA+U calculations are carried out using the VASP package [70, 71, 72, 73] with the projector-augmented wave method (PAW) [74, 75]. The PSIC calculation are performed using a custom in-house code with ultrasoft pseudopotentials [76] and a plane wave basis set. The cutoff energy was set at 420 eV. A Monkhorst-Pack [77] 9×19×6 grid was used for the self-consistency cycle. We assumed the crystal structure of $YBa_2Cu_3O_{6.5}$ determined by Grybos *et al* [78, 79]. We intentionally use the in-plane 2×1 periodicity appropriate to chain-ordered *ortho*-II YBCO at this specific doping, since experiments are claimed to be performed in this structure. We tested non-spin-polarized calculations, spin-polarized calculations with small initial moments, and fixed-magnetic-moment calculations with zero imposed magnetization, consistently getting the same results, i.e. a non-magnetic metallic state. The Fermi surfaces are visualized with the Xcrysden package [80, 81].

We used the Dudarev implementation [82] of GGA+U, whereby the relevant parameter is the difference U–J of the effective on-site Coulomb and exchange interactions. U–J was set to 9 eV for the d states of planar Cu, which reproduces the fundamental gap of Mott-insulating antiferromagnetic $YBa_2Cu_3O_6$ as obtained in PSIC [68, 69] or in experiment (no qualitative changes are observed down to U–J=6 eV for YBCO). We underline that the paramagnetic FS calculation is sensitive to U–J via small orbital polarizations (i.e. deviations from exact half-filling) in the partially occupied Cu $d_{x^2-y^2}$ states, and this may affect the details of band morphology in the vicinity of E_F.

For the magnetic phase we use only the PSIC approach. No attempt to describe by first-principles Ca-doped $Y_{1-x}Ca_xBa_2Cu_3O_6$ has been made so far, to our knowledge. A few LDA+U calculations were carried out for the simpler $La_{1-x}Sr_xCu_2O_4$ system [63, 83] (in particular Ref.[63] is the precursor study of polaronic configurations in high-T_c cuprates by first-principles), while model calculations for polaronic configurations are more common (see e.g. the Peierls-Hubbard Hartree-Fock Hamiltonian including electron-phonon coupling [84]).

Our PSIC calculations for $Y_{1-x}Ca_xBa_2Cu_3O_6$ are carried out with a plane waves basis and ultrasoft [76] pseudopotentials (energy cutoff 30 Ryd, 12×12×12 special k-point grids for density of states calculations, 11×11×11 uniform grid for FS calculations). Ca doping is described by explicit Y-Ca substitutions in 2×2×1 supercells, a choice which limits the magnetic patterns that can be simulated to PM and AF orderings, and two Zhang-Rice polaron configurations within AF background.

2.1.3 Non-magnetic phase: *ortho*-II $YBa_2Cu_3O_{6.5}$

In this section we study the FS of metallic, non-magnetic *ortho*-II $YBa_2Cu_3O_{6.5}$ (Fig.2.1) using GGA, GGA+U and PSIC. The calculated Fermi surface exhibits no pockets in GGA+U and PSIC, a minor one in GGA. Upon shifting the Fermi level in the vicinity of the calculated value, we instead observe several pocket structures. We calculate their cross-sectional areas and cyclotron masses. Overall, our calculations show no solid evidence of the existence of electron-like –nor, in fact, of any– Fermi surface pockets in this phase. This suggests that the origin of the pockets should be sought for in other, different phases.

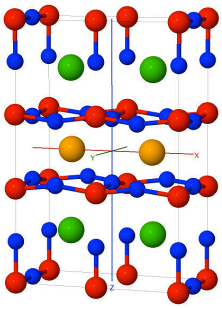

Figure 2.1: Crystal structure of $YBa_2Cu_3O_{6.5}$: yttrium (orange), barium (green), copper (red), oxygen (blue).

2.1.3.1 Band structures

In Fig.2.2 we compare the band structures in the k_z=0 plane, as obtained by the three methods. The dispersion in k_z is weak and not important in the present context. k_x and k_y are in units of the inverse $1/a$ and $1/b$ of the in-plane lattice constants. The leftmost panel (Fig.2.2(a)) displays the bands within the GGA approach. Moving along the ($\pi/2$,0)-($\pi/2$,π) direction, the first band to cross E_F is mainly due to states of the Cu(1)-O chain. This band is very close to being one dimensional. The next four bands crossings E_F come from the CuO_2 planes. There is a splitting between the bonding and antibonding CuO_2 bands of ~0.2 eV along the ($\pi/2$,0)-($\pi/2$,π) line at E_F. Each of these two bands are further split up by the additional $2a$ periodicity (this is most evident close to the point ($\pi/2$,π)). We find that the splitting is 40 meV at E_F along the ($\pi/2$,0)-($\pi/2$,π) direction. In the GGA calculation a fairly flat Cu(1)O chain-O_{apical} band crosses E_F close to the (0,π) point and gives rise to a small tubular quasi-2D hole pocket. This band is 13 meV above E_F at (0,π). In addition, a second band with a similar character lies just 20 meV below E_F at (0,π). Our results are similar to calculations on YBCO reported previously [62, 85].

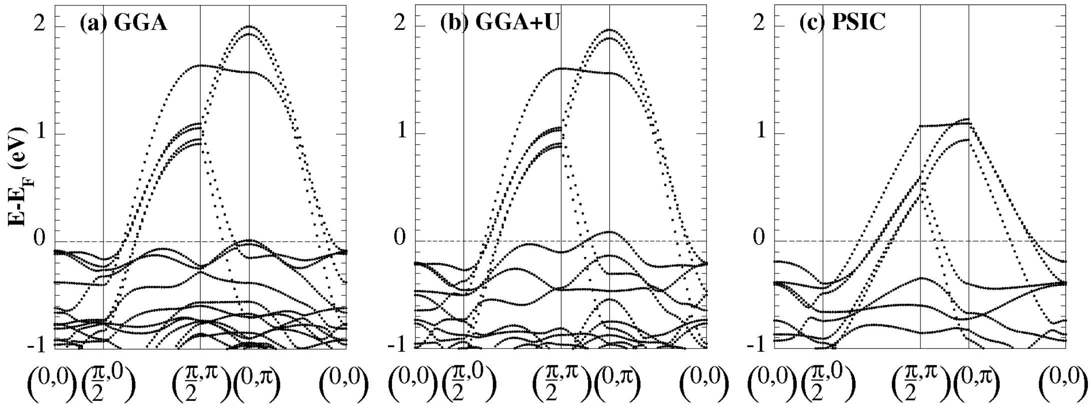

Figure 2.2: Band structures of $YBa_2Cu_3O_{6.5}$ - Band structures of $YBa_2Cu_3O_{6.5}$. (a) GGA, (b) GGA+U with U–J= 9 eV, (c) PSIC.

In the central panel, Fig.2.2(b), we show the GGA+U bands. Overall, the GGA+U rendition appears quite close to those of GGA. This is expected as U only affects magnetic and/or orbital-polarized states, thus the paramegnetic configuration is mildly affected. The main difference with respect to the GGA case is that the flat chain-apical bands crossing E_F near (0,π) are now about 80 meV above E_F and 140 meV below E_F at (0,π), i.e. they are split by more than 200 meV, compared to about 30 meV in GGA. This difference is due to the indirect (i.e. self-consistent) effect of the orbital polarization of in-plane Cu d states on the band manifold [82].

The right panel, Fig.2.2(c), shows our calculation with the PSIC technique. Here we see more radical differences with respect to the other two methods, mainly due to the fact that PSIC corrects for self-interaction Cu d as well as O p states, so that the corrections can be equally sizable for non magnetic and/or non orbitally-polarized states. This description results in generally less dispersed band structure; chain bands are now far from E_F, and the net result is that there are no small pockets in the Fermi surface.

2.1.3.2 Fermi surfaces

Strictly speaking, the theoretical prediction of the FS is based on the calculated electronic structure and Fermi level. Here, however, we also consider how the FS changes upon an upward or downward shift of the Fermi level compared to the calculated value. This is a fairly common practice in band theory studies of superconductors. The first motivation is that, while DFT calculations usually describe well the general features of the band structure of metals, small discrepancies in the relative positions of the bands are common when comparison with experiment is involved. (Generally, this relates to structural details and of course to the DFT description of the electron correlation.) For example, in Sr_2RuO_4, studied in detail with the dHvA technique, the Fermi energy needs to be shifted by 40 meV in either direction [86] to improve the calculated-bands agreement with experiment. Even in MgB_2, shifts of the order of 100 meV are needed [87, 88].

A further motivation pertaining to doped cuprates is that Fermi level shifts roughly simulate doping fluctuations. Of course the shift-doping relation depends on which specific band or bands are or get occupied upon shifting. In our case the maximum shifts applied (∼50–60 meV) correspond to rather substantial doping fluctuation ($\sim\pm0.04$, i.e. a 30% of the nominal doping).

In Fig.2.3 we collect the FS for the three techniques (top to bottom), and upward to downward (left to right) shifts of the Fermi level. The top panel (Fig.2.3(a)) reports GGA results. For ΔE_F=+50 meV the FS consists of just two large hole-like CuO_2 sheets centered on $(\pi/2,\pi)$, plus three quasi-one-dimensional sheets (one from the chains, and two from the planes). As E_F shifts down, a small hole-like pocket develops near the $(0,\pi)$ point, originating from the flat CuO-O_{apical} band discussed earlier. A further lowering of E_F causes this pocket to grow in size and then merge with the antibonding CuO_2 plane sheet. As E_F is further reduced, the second CuO-BaO band crosses the Fermi level, giving rise to another pocket. Eventually, this merges with the bonding CuO_2 plane sheet. Similar results were recently reported in Refs.[62] and [89].

Fig.2.3(b) shows the FS evolution according to GGA+U calculations. In this case for ΔE_F=+50 meV the FS is similar to the GGA calculation, but shows a hole-like pocket near the $(0,\pi)$ point, whose origin is the chain-apical band. This pocket merges with the CuO_2 sheets at zero shift. This trend is again expected given the larger splitting of the chain-apical band at $(0,\pi)$ discussed in connection with Fig.2.2. For ΔE_F=–55 meV, an electron-like pocket appears near $(\pi/2,\pi)$, surrounded by a hole-like sheet. Going back to Fig.2.2, one immediately realizes that this is also due to the enhanced splitting in GGA+U: a similar pocket would appear in GGA for a much larger negative shift of over 200 meV.

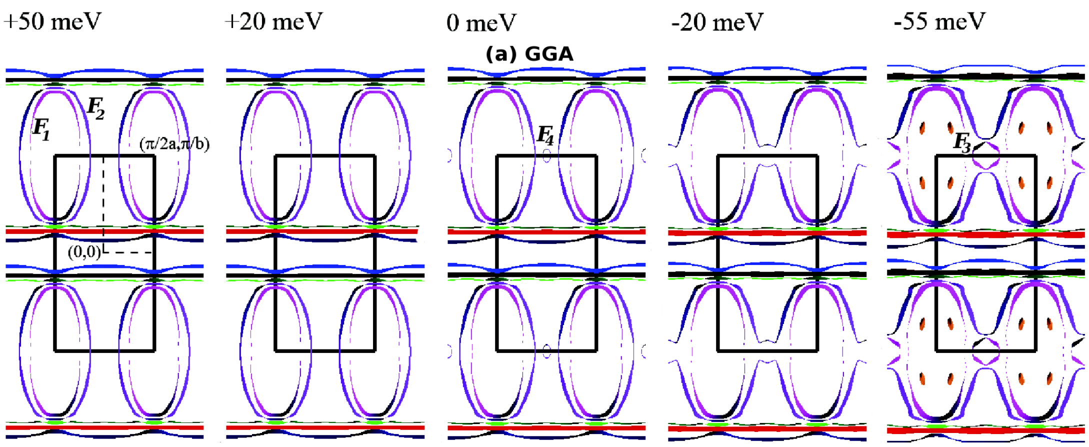
(a) GGA

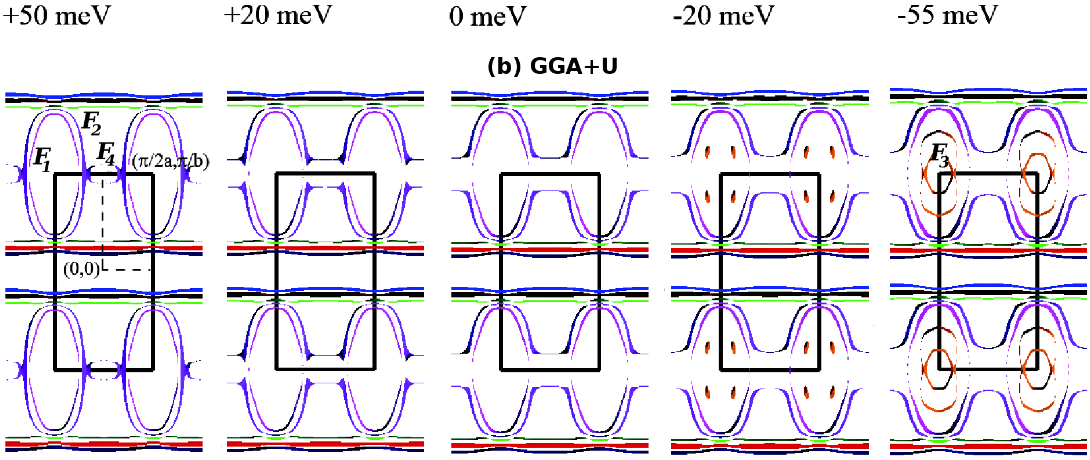
(b) GGA+U

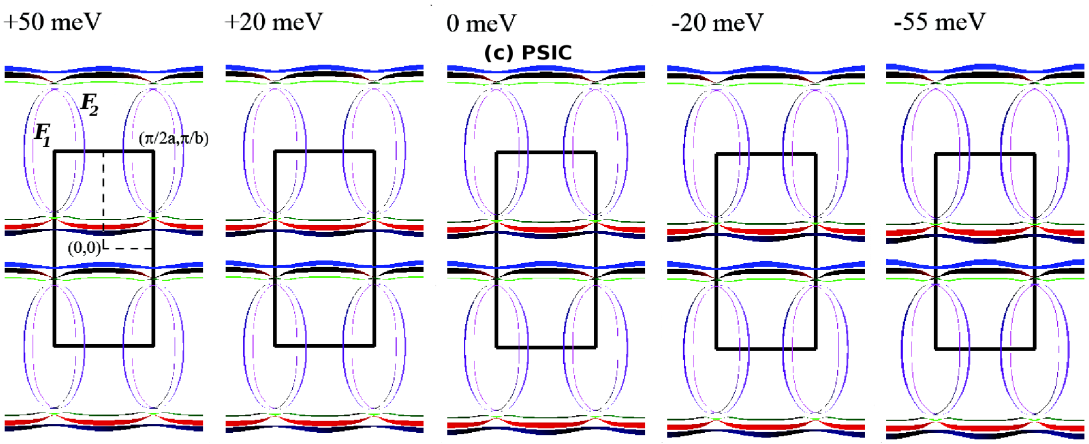
(c) PSIC

Figure 2.3: Evolution of the FS of YBCO - Evolution of the FS of YBCO with Fermi-level shift ΔE_F in the basal plane ($k_z = 0$). The main quantum oscillation orbits (F_n) are marked on the O meV and –55 meV panel for GGA (a), on the +50 meV and –55 meV for GGA+U (b). In PSIC there are no small pockets.

Fig.2.3(c) shows the PSIC results. The only structures in the FS are two large hole-like CuO_2 sheets centered on $(\pi/2,\pi)$. The Fermi level shift only moderately affect their area. No small pockets appear in this shift interval.

Overall Fig.2.3 shows a marked sensitivity of the GGA and GGA+U FS to the relative positions of the bands. This suggests that subtle changes in doping could result in the formation of small FS pockets. On the other hand, the PSIC FS is quite independent of doping, and would lead to predict or expect no small pockets at all.

2.1.3.3 Fermi surface pockets: frequencies and masses

To make contact with the quantum oscillations measured in SdH and dHvA experiments [36, 37, 38, 45], we calculate the quantum oscillation frequencies $F=(\hbar A/2\pi e)$ from the cross-sectional area A of the orbits (i.e. the pockets), and the attendant cyclotron masses $m=\hbar^2(\partial A/\partial E)/2\pi$ for the various structures found by the different techniques. They are reported in Figs.2.4, 2.5, and 2.6 for GGA, GGA+U, and PSIC, respectively.

For all techniques we report the high-frequency oscillations related to large cylinders; for GGA and GGA+U only, low-frequency oscillations related to small pockets are reported in a second panel. Thus, the frequencies shown in Fig.2.4(a), Fig.2.5(a) and Fig.2.6 (F_1 and F_2) are from the main CuO_2 sheet surfaces, whereas those in Fig.2.4(b) and Fig.2.5 (b) (F_3 and F_4) are from the small pockets. We note, first of all, that the frequencies calculated for the main CuO_2 sheets (F_1 and F_2) are similar for GGA and GGA+U with frequencies between 3000 T and 5500 T, whereas the frequencies calculated with the PSIC approach are between 1000 T and 2000 T. The reason of this difference is the lesser dispersion of the band structure as calculated with the PSIC technique. All values are way larger than the experimental one; the masses are typically a factor of two (or more) smaller than in experiment, and always negative. These FS sheets can therefore be ruled out as the origin of the experimental oscillations reported so far.

Next we analyze the small-pocket signals in the frequency range 0 to 900 T. In the GGA calculation, the hole-like pocket F_3 has a frequency between 100 and 600 T depending on the E_F shift; the experimental value would be attained at a shift of about –65 meV. The calculated mass of this pocket is shift-independent, and equal to $\sim$–1.4 m_e. The F_4 pocket has a fairly low frequency of 100 to 300 T and a negative mass similar to F_3. With the GGA+U approach we find the hole-like pocket F_4, with a

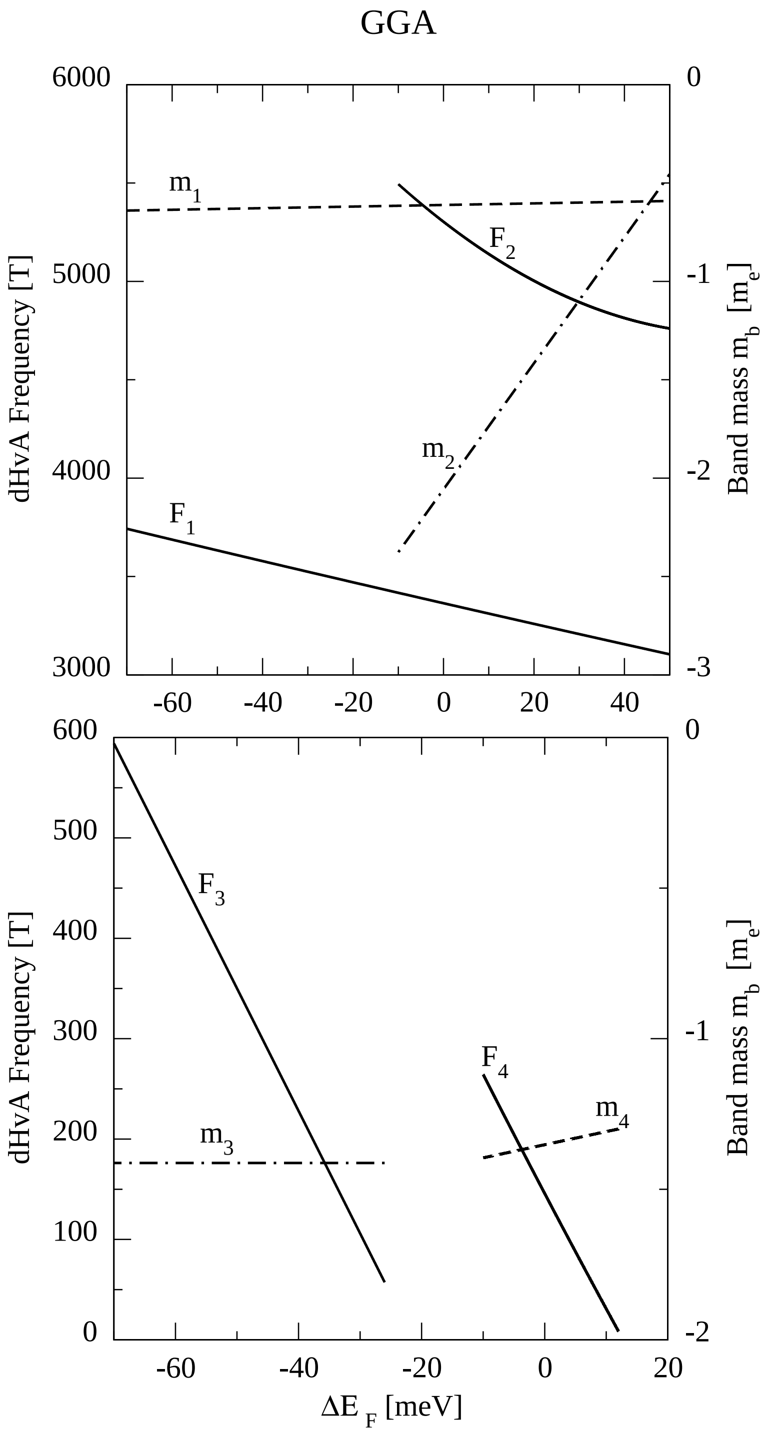

Figure 2.4: GGA extremal dHvA frequencies - GGA extremal dHvA frequencies (solid) for the large hole-like pockets (a) and for the small pockets (b). Dash-dotted lines are the calculated band masses.

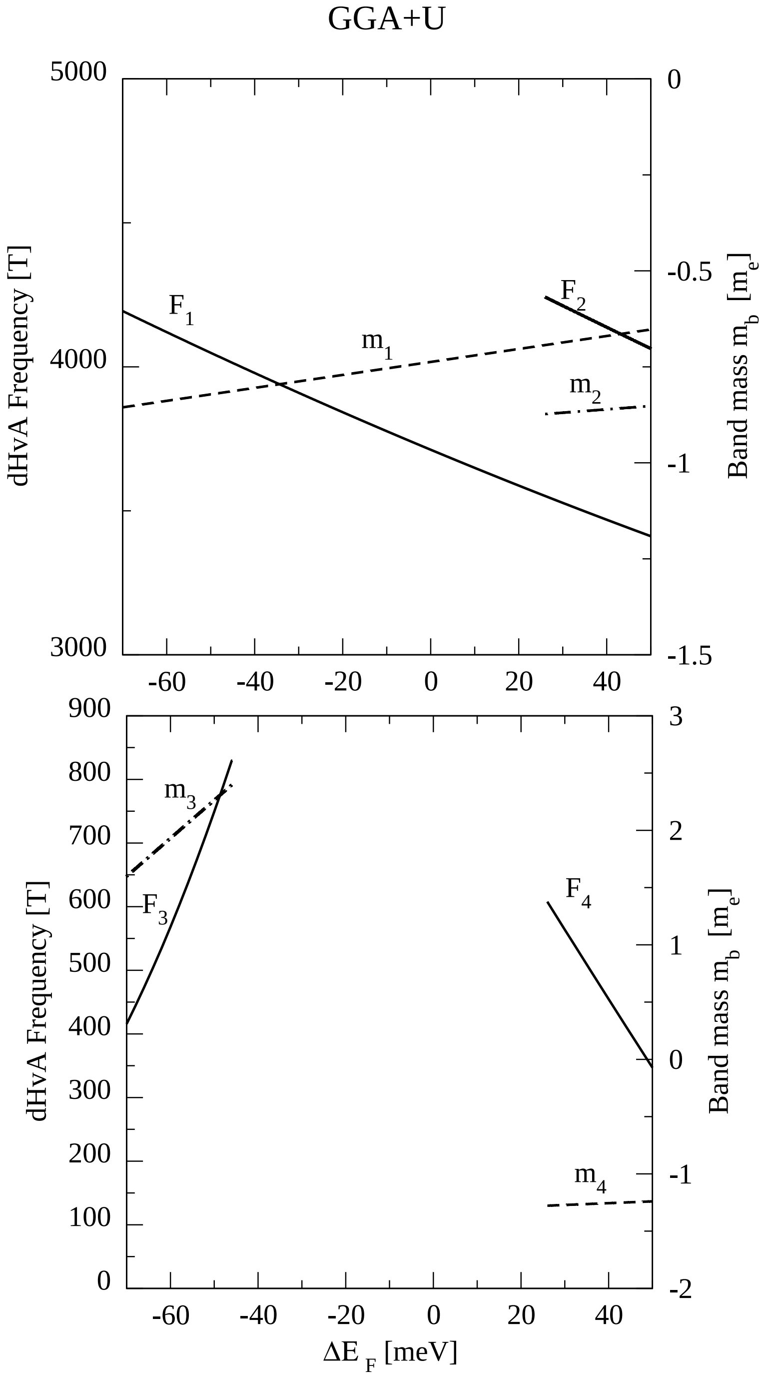

Figure 2.5: GGA+U extremal dHvA frequencies - GGA+U extremal dHvA frequencies (solid) for the large hole-like pockets (a) and for the small pockets (b). Dash-dotted lines are the calculated band masses.

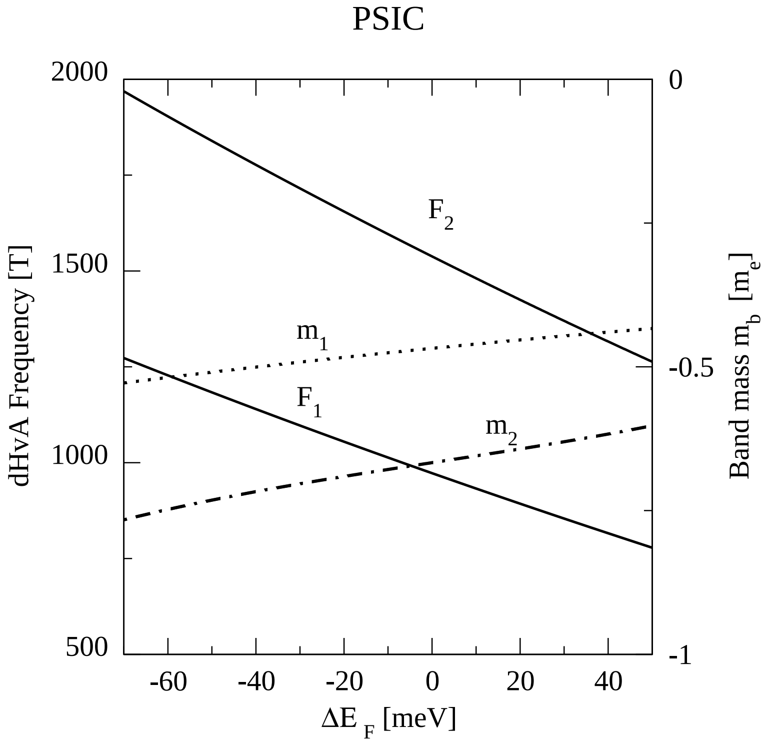

Figure 2.6: PSIC extremal dHvA frequencies - PSIC extremal dHvA frequencies (solid) for the large hole-like pockets. Dash-dotted lines are the calculated band masses.

roughly shift-independent mass of $\sim$–1.25 m$_e$ and frequency in the 400 to 600 T range, and the electron-like pocket F$_3$ with frequency between 400 and 800 T and a sharply varying mass, between 1.5 m$_e$ and 2.3 m$_e$.

Comparing with experiments [36, 37, 38], several of our calculated pockets may seem good candidates. Frequencies and masses (in absolute value) are more or less in the ballpark. If we accept the assumption that the change of sign of the Hall resistance [37] is purely due to the electron-like nature of the pockets, we implictly fix the experimental sign of the mass to a positive value. The frequency *and* mass deduced from observation [36, 37] would then be compatible only with the F$_3$ GGA+U pocket.

A very recent measurement [45] in $YBa_2Cu_3O_{6.51}$ has revealed, in addition to the same signal of Ref. [36], an oscillation with frequency and mass in the vicinity of 1600 T and 3.4 m$_e$ respectively. In Ref.[45] (p.210) the signal is attributed tentatively to a hole-like pocket. In all our calculations, including shifts, there is only one case (GGA+U at large negative shift, rightmost picture in panel b of Fig.2.3) in which hole and electron pockets coexist. Near the (π/2,π) point in the GGA+U calculations, starting at a shift of –55 meV, the structure recognizably involves two distinct pockets: one is the electron pocket F$_3$ discussed above; the other a larger hole-like pocket surrounding F$_3$ itself. Their simultaneous presence is due to a change in curvature of the same band, most notably between (π/2,π) and (π/2,0). The character of this band is, like that of F$_3$, strongly chain-apical. The corresponding calculated frequency is about 2200 T and a mass of –1.4 m$_e$. The frequency is very roughly similar to the 1600 T measured in Ref. [45], while the mass is over a factor two smaller.

Overall, however, we conclude that there is not enough evidence to actually associate our calculated results to the experimental findings of Refs.[36, 37, 38, 45]. The reasons will be discussed in the next Section.

2.1.3.4 Discussion and summary

The calculations just reported have detected several small pockets (mainly hole-like) roughly compatible with the observed oscillation. However, all these small pockets have essentially chain or chain-apical character, and not in-plane character. GGA+U does seemingly finds the “right” pattern of coexisting electron and hole pockets, but (aside from the need for an artificial –60 meV Fermi level shift, corresponding to a 30% over-doping) both pockets have a chain-apical nature even stronger than the corresponding

GGA-calculated band due to the remarkable (perhaps exaggerated) U-induced lowering of in-plane Cu bonding states.

On the other hand, there appears to be experimental evidence that the negative and oscillating Hall resistance at low temperature resulting from electron-like pockets (i.e. a positive mass) be related to states residing in the CuO_2 planes. This is supported [36] by the suppression of *ab*-plane conductivity anisotropy below 100 K, implying that chains do not conduct at low temperatures (and high field).

Further supporting the fact that FS pockets are a plane-related feature, quantum oscillations were observed in $YBa_2Cu_4O_8$ [37, 39, 90]. Calculations [62, 90, 91] for that compound have shown that the GGA-calculated band related to the F_3 hole pocket in $YBa_2Cu_3O_{6.5}$ is now as far as 400 meV below E_F, hence cannot not reasonably invoked to explain the observations.

We further recall that pockets appear only upon appreciably shifting the Fermi energy: the proper calculated Fermi surfaces, i.e. those at zero shift, show no small pockets, except for the GGA F_4 hole pocket of Fig.2.3(a), related to the backfolding in the 2×1 cell of a pocket found by GGA itself in $YBa_2Cu_3O_7$ (not seen by ARPES) [92].

Were we forced to embrace one of the methods applied here and the pertaining conclusions as the most reliable in this context, we would by all means pick PSIC, and conclude that in non-magnetic YBCO simply there are no small pockets, electron-like or otherwise. Indeed, among those used here, PSIC has shown to be by far the most dependable technique in the context of cuprates. For instance, the energy balance of various magnetic phases of $YBa_2Cu_3O_{6+x}$ is correctly described, and so are the general properties of a number of cuprates [64, 65, 66, 67, 68, 69]. Furthermore, in the context of FS determination, PSIC (top of Fig.2.7) matches ARPES perfectly for $YBa_2Cu_3O_7$ [92] whereas GGA (bottom of Fig.2.7) finds, as mentioned, a zone-corner pocket which ARPES does not observe.

In summary, we presented calculations of the electronic structure of YBCO in the non-magnetic state with three different DFT-based approaches: GGA, GGA+U and PSIC. Upon substantial shifts of the Fermi energy, GGA and GGA+U do produce small FS pockets, mostly originating from chain or chain-apical bands, with frequencies and band masses similar to those experimentally observed (one GGA+U pocket has a positive cyclotron mass, i.e. is electron-like), while PSIC shows no small pocket at all.

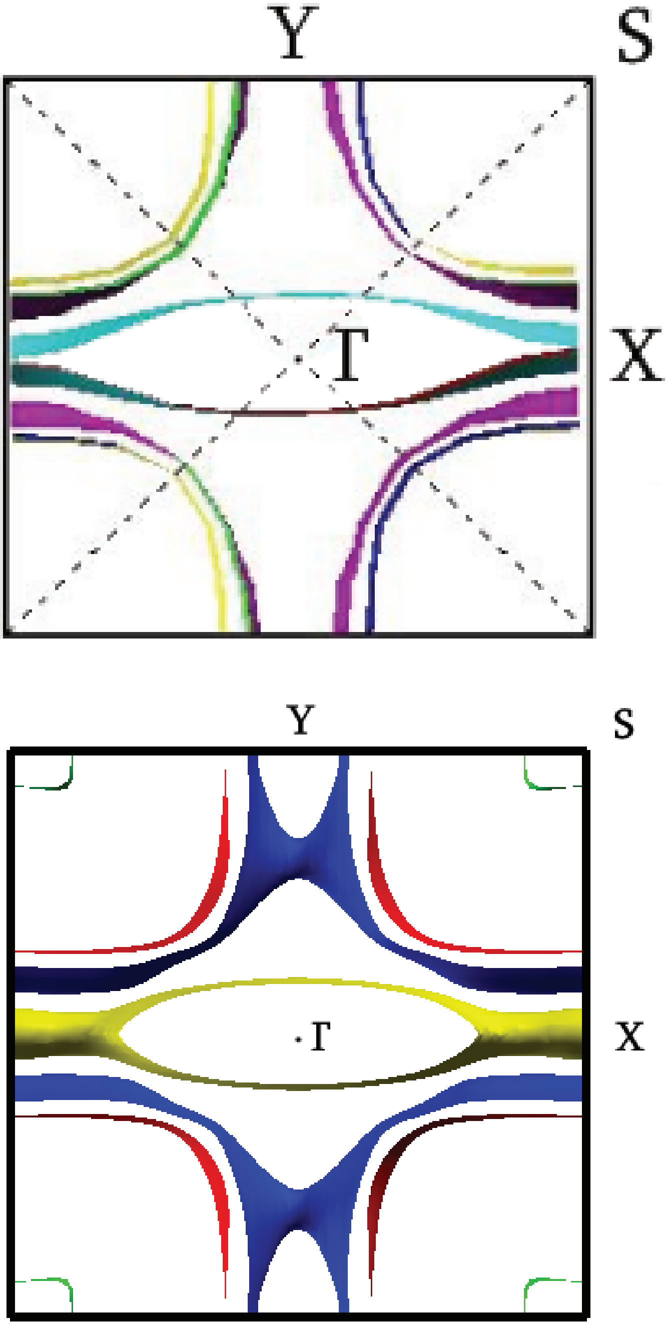

Figure 2.7: PSIC (top) and GGA (bottom) FS for $YBa_2Cu_3O_7$

As discussed, our conclusion is that there is no unambiguous evidence for the existence of electron-like pockets –nor, indeed, of any pockets– in the non-magnetic metallic state of $YBa_2Cu_3O_{6.5}$. In addition, no pockets (either electron or hole) derive from in-plane states. This is a conclusion coherently obtained by three different *ab initio* techniques. We suggest that the experimentally observed pockets are a property of *another* state of YBCO, possibly characterized by some form of ordering (probably magnetic, given its coexistence with superconductivity up to high doping revealed by many experiments) causing a FS reconstruction.

2.1.4 Magnetic phase: $Y_{1-x}Ca_xBa_2Cu_3O_6$

In this section, using the PSIC, we study the FS of underdoped $Y_{1-x}Ca_xBa_2Cu_3O_6$ (Fig.2.8) in a selection of magnetically ordered and polaronic states. Inclusion of doping on the antiferromagnetically ordered CuO_2 planes causes the appearance of small, hole-like Fermi surface pockets centered around the nodal points. The pocket properties (area, mass) depend on the underlying magnetic ordering (e.g. change with polaron formation), although the hole-like character is rather persistent for all the examined magnetic states.

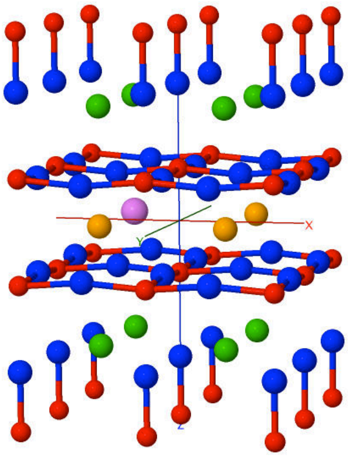

Figure 2.8: Crystal structure of $Y_{1-x}Ca_xBa_2Cu_3O_6$ for x=0.25: yttrium (orange), barium (green), calcium (violet), copper (red), oxygen (blue).

2.1.4.1 Results

The PSIC approach successfully describes [68] the undoped precursor $YBa_2Cu_3O_6$ as an AF Mott insulator. The main features of the AF Mott phase can be recognized in the closely similar orbital-resolved density of states (OR-DOS) at h=x/2=0.125 (top panels of Fig.2.9): valence and conduction bands are a mix of spin-polarized Cu $d_{x^2-y^2}$ and unpolarized O p_xp_y states, with the main optical transition (involving CuO_2-plane orbitals) starting at 1.2 eV, and higher transitions around 3.5 eV into apical O p_z and Cu d_{z^2} states. The Cu magnetic moments of 0.5 μ_B and in-plane AF coupling constant J≃0.15 eV in $YBa_2Cu_3O_6$ agree well with experiment.

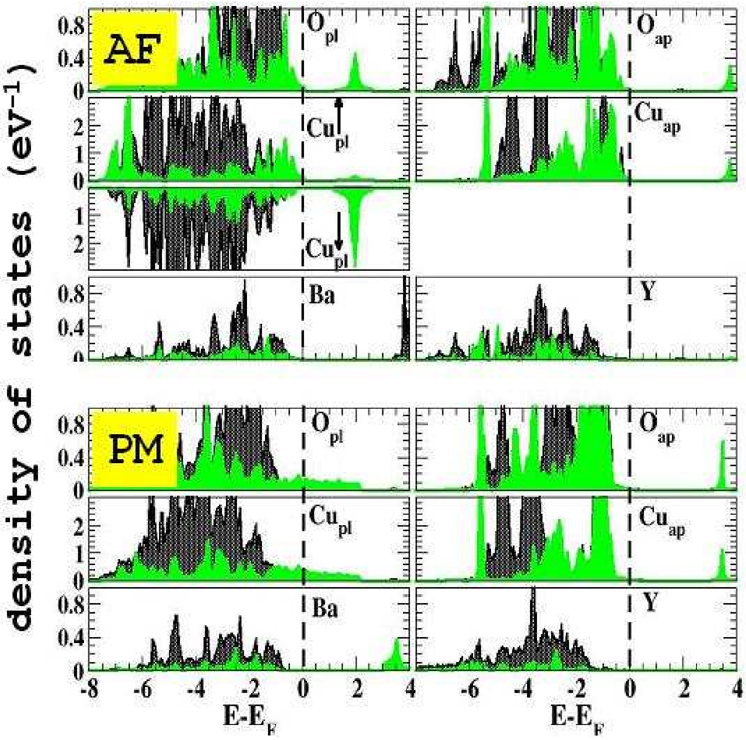

Figure 2.9: OR-DOS for AF and PM phase at h=0.125 doping - OR-DOS for AF (top) and PM (bottom) phase at h=0.125 doping. Labels "ap" and "pl" indicate apical and in-plane (CuO_2) atoms, respectively; arrows show spin directions. For each atom the light shadowed (green) curves shows the most important orbital contribution (p_x for O_{pl}, p_z for O_{ap}, $d_{x^2-y^2}$ for Cu_{pl}, Ba, and Y, d_{z^2} for Cu_{pl}), the dark shadowed (black) curves the contribution of the other p (for O) and d (for Cu, Y, and Ba) orbitals.

Fig.2.10 report calculated band energies, hole density isosurfaces, and FS for both AF and metallic non-magnetic (i.e. Pauli-paramagnetic (PM)) phases at h=0.125. The latter (right panels) shows doubly degenerate bands, and no Mott gap. The valence band is a 3.5 eV-wide spin-unpolarized $d_{x^2-y^2}$-(p_x,p_y) hybrid, with Fermi level E_F at ∼2 eV below the valence band top (VBT). The corresponding hole density is an array of connected bonds of self-evidently $d_{x^2-y^2}$-(p_x,p_y)–like shape; the FS is a large cylinder centered at the zone corner, as expected for the metallic Fermi-liquid-like state. Only in-plane atoms contribute to the FS, whereas apical-atom states start appearing ∼0.2 eV below E_F.

In the AF state (left panels) holes are homogeneously spread and evenly distributed through up- and down-polarized planar Cu. Despite the altered orbital filling and magnetic moments of Cu, the AF ordering is weakened but remains substantially in charge. The Mott gap still splits the planar CuO_2 band manifold into 2 eV-wide empty upper and nearly filled lower Hubbard bands. The latter is sliced by E_F at 0.1 eV below its top, along the BZ diagonal near the nodal point, with off-plane states again far below E_F. The reduced valence bandwidth with respect to the PM case follows from AF ordering, which hinders Cu-Cu nearest-neighbor hopping of spin polarized $d_{x^2-y^2}$-(p_x,p_y) holes. We see that the AF hole density is no longer an array of connected bonds, but is disentangled in two spin-polarized sublattices in which hole carriers of same polarization are enclosed in a single CuO_4 square. Because of this decoupling, the AF Fermi surface (plotted in the 1×1 reduced zone of edge $2\pi/a$) is squeezed from a large cylinder to circlets enclosing small areas around nodal points. A closer inspection reveals four (doubly degenerate) concentric circlets, one for each of the two up- and two down-polarized states per 2×2 CuO_2 plane. An estimate of our calculated FS area A_k for a single pocket (averaged over the four circlets of each pocket) gives 1.9% of the 1×1 BZ area $A=(2\pi/a)^2$, which converts to a frequency of 600 T, close to the value obtained via Onsager relation from SdH measurements[36, 37, 38]. The calculated hole-like effective mass per pocket, however, is –0.5 m_e, well below the experimental value reported in Ref.[36, 37, 38]. According to Luttinger's sum rule, an estimate of the carrier concentration can be derived from the pocket area in 2-D as $n=[2/(2\pi)^2](A_k/A)$, which for the four pockets gives a carriers/holes ratio of n/h∼1.2 in the AF state at h=0.125, thus suggesting a weak violation of Luttinger's sum rule (n=h), or more likely

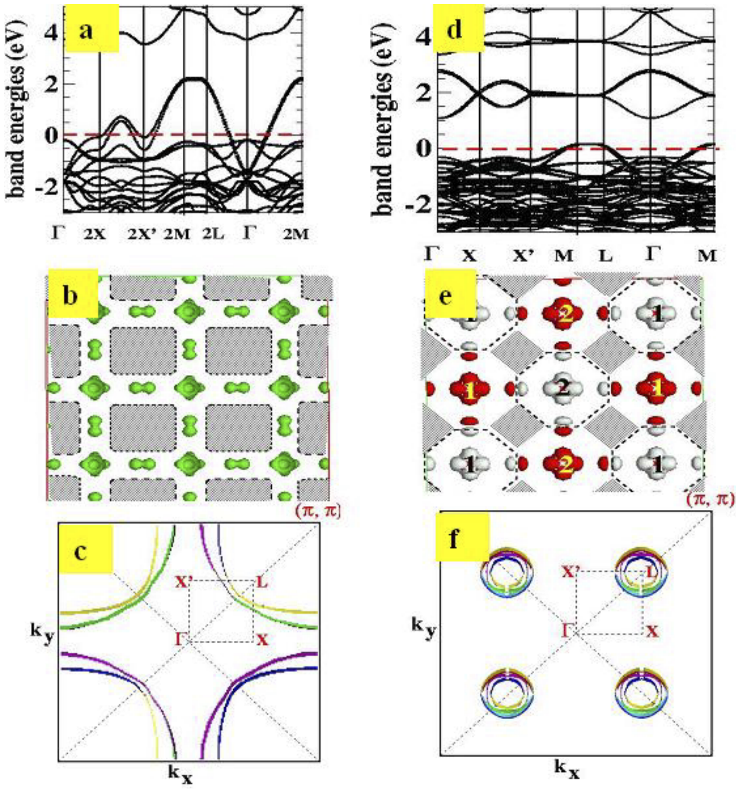

Figure 2.10: Band energies, hole density isosurface, Fermi surface - Top: Band energies at x=1/4 (h=0.125) for (2×2) AF phase (d) and (1×1) PM phase (a). K-points coordinates (units of 1/a=1/b, 1/c with a, b, c unit-cell parameters) are X=[π/2,0,0], X=[0,π/2,0], L=[π/2,π/2,0], M=[π/2,π/2,π/2]. Middle: hole density isosurface for AF (e) and PM (b) phases. For the AF white and red lobes are for up- and down-polarized holes. Bottom: calculated FS for AF (f) and PM (c) phase.

that the FS differs slightly from the Luttinger surface to which the sum rule applies [93]. Experimentally [36, 37, 38] a similar value (n/h∼1.5) was deduced.

We emphasize that a reason to compare the FS of magnetic phases with experiment is the evidence [94] that magnetic order develops in high magnetic fields at low doping in the superconducting state (this was modeled in Ref. [47]). The key difference between PM and AF Fermi surfaces is that in the former the electronic states are spin-degenerate, thus each FS point hosts two spin-compensating holes, while in the latter the injected holes are fully spin-polarized, i.e. each circlet visible in the AF FS plot can only be inhabited by fully spin-polarized carriers. Due to planar AF symmetry each up-polarized circlet is matched by an identical down-polarized, so that the total current can be still thought of as spin-compensated. However, this is not longer true when AF ordering is lost, which may occur due disorder and/or short-range localization phenomena. This motivates the exploration of more complex magnetic configurations than ordinary AF. Indeed, while the presence of closed features surrounding nodal points is a general characteristic of the AF background, shape and size of these FS features may be altered upon inclusion of polaronic states. Here we make a first attempt to model polarons and the attendant FS.

In Fig.2.11 (again at h=0.125 doping) we describe the electronic features of spinless polarons (reminiscent of the Zhang-Rice singlet (ZRS) polarons [95]) embedded in the CuO_2-plane AF background. According to the Zhang-Rice model, a doping hole localizes on the four oxygens of a given CuO_4 plaquette, and strongly couples to the native hole on Cu(2) forming a two-body singlet state. The coupling may be driven or accompanied by local lattice distortion. From our band-theory perspective, this picture corresponds to a self-consistent solution with the hole charge mainly "condensed" on the four oxygens of a single CuO_4 unit, with magnetization anti-paired to (i.e. compensating) that of the Cu(2) ion. In the following our polaronic solutions will be indicated as ZRS for brevity, although the singlet is strictly a 2-body state, whereas our equations deliver the one-body –i.e. integrated– density matrix of an interacting electron system.

We found stable ZRS solutions provided that an O breathing distortion was frozen-in (the four oxygens of one ZRS-to-be CuO_4 unit were equally displaced by 1% of the lattice parameter towards the Cu at the center of one ZRS-to-be CuO_4 unit). The condensation of one ZRS occurs within each breathing-distorted CuO_4. (We remark that the breathing displacement amplitude is tentative, i.e. not obtained by structural relaxation according to energy minimization, but the qualitative description of the ZRS state would not change by structural optimization in 2×2 symmetry.) The nature of this state is apparent from the hole spin densities: in Fig.2.11 (a2) we have one ZRS per cell (dashed circle), in Fig.2.11 (b2) two ZRS per cell aligned into [110]-oriented stripes. (those two are the only configurations which can be considered in 2×2 in-plane symmetry). We observe that the ZRS "condense" on the distorted CuO_4 plaquette: holes localize on oxygens, and the induced magnetization is indeed anti-aligned to that of Cu, producing a vanishing total magnetization on the distorted CuO_4 unit. Notice that the other non ZRS-populated CuO_4 units (i.e. belonging to the AF background)

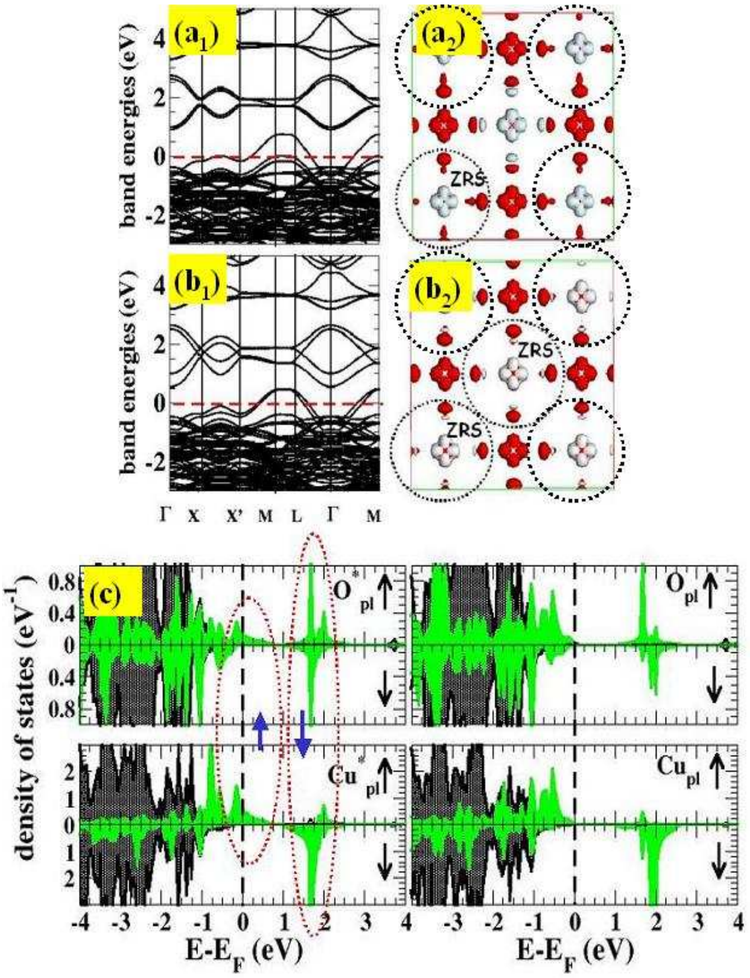

Figure 2.11: ZR - Top: Band energies and hole spin density isosurface (h/V=0.006 bohr^{-3}) at h=0.125 doping for two different magnetic phases with ZRS included, both within (2×2)symmetry. (a1) and (a2) refer to the one-ZRS per 2×2 plane configuration, (b1) and (b2) for two-ZRS per 2×2 plane configuration. (c) Orbital-resolved DOS for the one-ZRS configuration (only planar Cu $d_{x^2-y^2}$-O (p_x,p_y) state are shown for simplicity). Red (dotted) ellipses enclose the ZRS DOS contributions from injected and native antialigned holes (blue arrows) to give S=0 locally.

remain substantially unaffected by the presence of ZRS on the adjacent unit. This arrangement is different from that described by LDA+U in Ref.[63] where spin-bag (i.e. non spin-compensated) polarons were obtained on the CuO_2 planes of $La_{1-x}Sr_xCu_2O_4$.

The ZRS signature in Fig.2.11 (a1) is a single CuO_2 band being depleted (i.e. hole-filled) and lifted by about 0.7 eV over the valence bands related to the AF-ordered units. In the stripe configuration of Fig.2.11 (b1), two ZRS bands are now raised by roughly the same amount above the valence AF background. All other bands related to non-ZRS CuO_2 units are well below E_F and unaffected by hole injection. Thus, in both cases, only the ZRS bands contribute to the FS. The OR-DOS in Fig.2.11 (c), left panel, shows that each ZRS band involves all the four in-plane oxygens first-neighbors to the central Cu of the ZRS unit. This up-polarized hole couples to the native Cu down-polarized hole (the two are enclosed in dashed ellipses) to form the singlet. The DOS from non-ZRS CuO_2 units in (Fig.2.11 (c), right panel, is close to that of the AF phase in Fig.2.9, with hardly any magnetic moment reduction on Cu.

Fig.2.12 shows the FS of the three examined magnetic states (AF, one-ZRS, two-ZRS) at different values of h. The calculated FS at h=0.125 is in the central-column panels (the others are discussed below). Closed FS structures near nodal points appear to be a general feature of spin-polarized states. The one-ZRS FS shows a large nodal-point centered pocket due to the ZRS band (plus a minor AF-background pocket). In the two-ZRS configuration we find intersecting pockets from the two ZRS bands. The pocket shape is circular for the single ZRS, while for the stripe it is the intersection of two 90°-rotated ellipses. From the calculated FS areas of the ZRS bands, we obtain $n/h{\sim}1.2$ and $\sim$1 respectively, again mildly deviating from the Luttinger sum rule. (Notice that for PM and AF orderings, as previously discussed, holes were evenly distributed on all CuO_2 units. In the one- and two-ZRS configurations, they concentrate on one and two CuO_2 units respectively, so the effective doping is in fact h=0.5 and h=0.25.) The frequency and mass for the one and two ZRS cases is 2500 T and 1600 T respectively, with masses of –0.4 and –1. These do not match the SdH experimental values reported for $YBa_2Cu_3O_{6.5}$ at $h\simeq0.1$[36, 37, 38]. The numerical discrepancy may be attributed in part to the different doping mechanism and different effective doping h; however, the difference in mass sign (hole-like for our calculations, electron-like for the experiments) suggests that this polaron configuration is not what is actually observed in SdH and dHvA experiments.

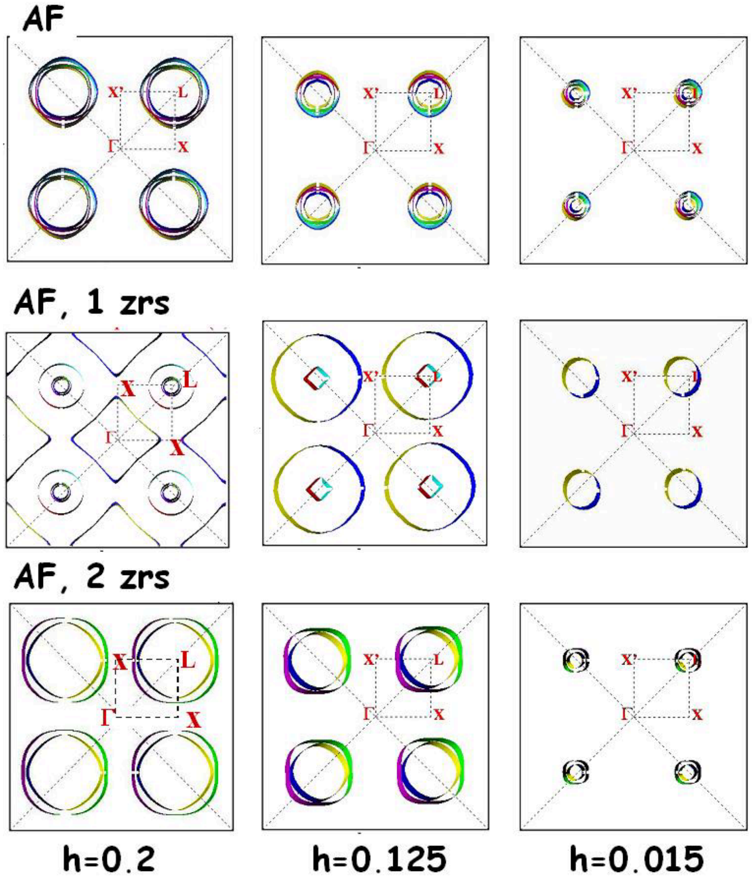

Figure 2.12: Evolution of the FS vs. rigid Fermi level shift - Evolution of the FS vs. rigid Fermi level shift ΔE_F for AF (top panels), AF plus one-ZRS (middle panels), AF plus two-ZRS (bottom panels) configurations. From left to right, $\Delta E_F = -0.2$ eV ($h \sim 0.2$), 0 ($h = 0.125$), and +0.1 eV (for AF), +0.5 eV for the two ZRS configurations ($h \sim 0.02$).

2.1.4.2 Discussion

A definite conclusion we can draw is that different magnetic configurations in zero field and 2×2 periodicity will produce FS differing in the details, but sharing the character of nodal hole-like pockets. This is broadly consistent with ARPES, but not with SdH/dHvA. To verify if electron-like branches may appear in the vicinity of E_F as calculated for h=0.125, in Fig.2.12 we also plot the FS obtained rigidly shifting E_F, which very roughly simulates doping fluctuations [34]. The FS remains hole-like and the pocket area falls sharply for an upwards shift ("decreasing doping", right panel column in Fig.4). Electron pockets at the anti-nodes do instead appear (while hole pockets open up) for E_F shifting down (left panel column in Fig.4). The shift, however, would correspond to optimal doping, i.e. to a unrealistic 50 % doping fluctuation. There is no obvious way to reconcile the Hall resistance sign with the present results. If one accepts the notion that the low T-high field Hall resistance (i.e. mass sign) change is a genuine electron current signature in the normal state, the present configurations should be ruled out. This does not imply that magnetism is not involved (we in fact think it is). A series of different polaronic patterns (e.g. as in Ref.[52, 53] and [63]) have been proposed as possible stable electronic configurations at low doping, but the present approach cannot yet tackle computationally the supercells needed.

We finally touch upon attempts to reconcile SdH pockets –whose shape, number, and location is undetermined– with ARPES arcs near nodes (see e.g. [48, 50, 96] for a summary). Recently, a photoemission pattern switching from large-doping Fermi cylinders to low-doping arcs was observed [44] upon tuning the self-doping of $YBa_2Cu_3O_{6+x}$ via surface treatment. Cylinders and arcs appear to coexist in different sample portions depending on the local self-doping, and arcs were hypothesized [44, 48] to be residual pockets (the estimated "virtual" areas would be, as our own are, in fair agreement with SdH data). From total energies, we find the PM phase slightly lower than, but still quite close to AF. A coexistence may be expected, as suggested by μSR experiments [54]. One may then speculate that the observed FS results from a configuration-averaged superposition of pockets and cylinder portions whose shape and spectral intensity depends on extension and shape of coexisting AF and PM regions. Indeed, short-range AF order [48, 50] has been shown to cause a similar "unfocusing" of the pocket shape into an apparent arc shape. Finally, of course, oscillations may turn out to be a token of the high-field conditions in SdH/dHvA, but this is outside our present scope.

2.1.4.3 Conclusions

We studied in detail the electronic structure of underdoped $Y_{1-x}Ca_xBa_2Cu_3O_6$ by the PSIC approach. Our results showed that AF phases (with or without embedded polarons) produce closed hole-like FS branches centered at nodal points, whose area depends on the doping concentration and for h=0.125 is comparable to the pocket area observed by SdH for $YBa_2Cu_3O_{6.5}$ at h=0.1. On the other hand, Fermi-liquid cylinders are always related to the spin-compensated (i.e. non-magnetic) states. These results support the viewpoint that pocket/arc dichotomy may be due as a superposition of pockets and cylinder portions related to competing AF and PM regions. We remark that some features of the pockets (specifically the effective mass and its sign) are not consistent with oscillation experiments on $YBa_2Cu_3O_{6.5}$, so that no unambiguous identification can be made. The indication is that the AF and high-density ZRS polaron configurations explored here are not the states observed by oscillation experiments. Candidate alternatives may be either an exotic field-induced state, which is beyond the scope of our method; or more complex polaronic structures [52, 53, 63] (plus coexisting orderings separated at nanoscopic range [54]) which are conceptually describable by our method, but for the moment computationally unapproachable.

The conclusions of this work compare reasonably with recent experiments. The existence of long-range (albeit incommensurate) spin order has been confirmed [97]; and additional quantum oscillations have been observed and interpreted as spin density wave induced [98]. This vindicates our choice of a spin density wave symmetry breaking, although very simplified because of the size of the system we can afford. The supposition that the pocket/arc dichotomy may be due as a superposition of pockets and cylinder portions related to competing AF and PM regions is compatible with the doping evolution of the Fermi surface topology recently observed in another cuprate [99].

2.2 CuO: rocksalt-structure

The main part of the following discussion is published in the APS Journal "Phys. Rev. B, 80(140408), 2009 [100]". In this section my operational contribution was the calculation of the total energy for several magnetic phases vs c/a and the estimation of the Néel temperature for the tetragonal-rocksalt CuO or about the 70% of the work. The writing and preparation of the paper was done collaboratively with coworkers and supervisors, as did the planning and assessment of the work.

2.2.1 Introduction

The monoxides of most $3d$ transition metals crystallize in rocksalt-like structures. They realize an insulating electronic spectrum removing spin-orbital degeneracies in the octahedral submanifolds t_g and e_g of the d shell by means of magnetic ordering and lattice distortions. Copper monoxide becomes a Mott-like charge-transfer insulating type-A antiferromagnet [101, 102] via a less direct, though conceptually equivalent strategy: it adopts a relatively low-density monoclinic structure comprising distorted tetrahedral units (see the discussion in Ref.[64]), called tenorite. Can CuO be stabilized in some close relative of the rocksalt structure? Cubic rocksalt CuO would be a Pauli-paramagnetic metal. Given the $t_g^6 e_g^3$ orbital configuration of Cu^{2+}, spin-orbital degeneracy removal requires both magnetic order and symmetry-lowering structural distortions. The minimal distortion needed is the paradigmatic Jahn-Teller elongation of the Cu-centered octahedra along the z axis (rocksalt can be seen as made up of side-sharing octahedra). The symmetry of stable rocksalt-like CuO will therefore be no higher than tetragonal, with two lattice constants a (in-plane) and c (vertically).

The routes to gap opening and structure stabilization in CuO have enjoyed a revived interest after Siemons *et al.* recently grew [6] on cubic $SrTiO_3$ an ultrathin ($\sim$15-20 Å) CuO film with apparently rocksalt-like structure.

In this section we report ab initio calculations on CuO done with the PSIC [3, 103] method [76, 104], which treats accurately the delicate chemistry of divalent Cu in cuprates, which are instead unapproachable by standard methods. Indeed, we have verified that LDA invariably produces a non-magnetic metallic rocksalt CuO, as in the case of tenorite CuO [64].

2.2.1.1 Electronic and magnetic properties

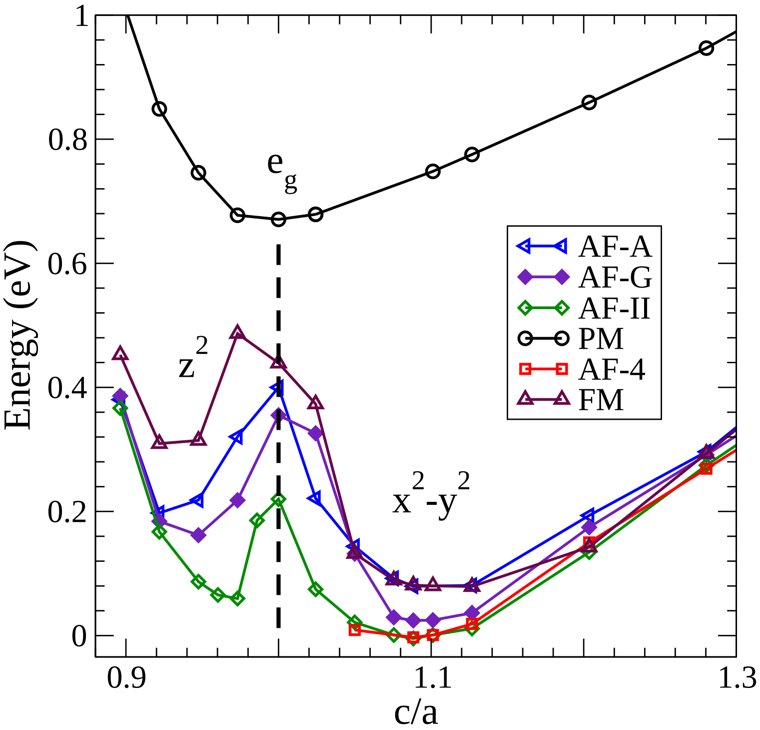

Figure 2.13: Energy per formula unit vs c/a for tetragonally-distorted CuO, in-plane lattice constant a=3.905 Å. The energy zero is the lowest structure, AF-II at c/a=1.09. In the regions labeled 'z^2' and 'x^2–y^2, the magnetic hole has d_{z^2} and $d_{x^2-y^2}$ character respectively. The barrier between the two minima corresponds to degenerate e_g states.

In Fig.2.13 we report the energy vs c/a of tetragonal-rocksalt CuO in the non-magnetic, ferromagnetic (FM), and four different antiferromagnetic (AF) ordering states, at the lattice constant a=3.905 Å of the SrTiO$_3$ substrate (see also below). In this structure, Cu atoms sit on an fcc lattice slightly elongated along the cartesian z axis, and their spin arrangement defines the magnetic ordering. The AF phases we consider are AF-A, AF-G, AF-4 and AF-II. While these are only some of the many possible spin arrangements on this lattice, they suffice to calculate the independent magnetic couplings; also, by analogy with other monoxides, they are likely to capture the essential physics. AF-A is made of ferromagnetic planes stacked antiferromagnetically in pairs (similarly to tenorite) along z; it is barely metallic at all c/a's, with a single band dipping below the Fermi level in a small region of the Brillouin zone. AF-G is fully antiferromagnetic (and equivalent to two interpenetrating ferromagnetic cubic lattices), and has a tiny indirect gap over most of the c/a range. The last two, AF-II and AF-4, compete closely for stability. The lowest-energy structure in Fig.2.13 is AF-II, typical of other transition-metal monoxides. It consists of z-, AF-stacked planes each built up of (110)-oriented ferromagnetic Cu rows arranged antiferromagnetically in the $(1\bar{1}0)$ direction (see further discussion below). This phase has a gap of 1.1 eV at the absolute structural energy minimum. The AF-4 structure is very similar (see below) and very close in energy to AF-II. The topmost curve in Fig.2.13 is the non-magnetic metallic state, with an equilibrium c/a of 1 and degenerate e_g states. The tenorite structure studied in Ref.[64] is as expected energetically favored over all the present structures.

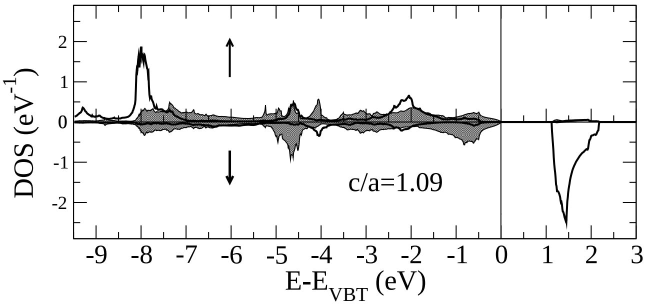

Figure 2.14: Density of states of CuO projected on Cu e_g orbitals at the axially-expanded minimum. Energy zero is the valence band top. Thick solid line: $d_{x^2-y^2}$; thin solid line, shaded curve: d_{z^2}. The antiferromagnetically-split Cu hole is almost pure $d_{x^2-y^2}$. The spin splitting of this state, 9.5 eV, is a measure of the effective on-site interaction U.

The energetics shows that the cubic non-magnet (or Pauli paramagnet) collapses spontaneously into tetragonally-distorted spin-polarized structures. The magnetic states have two distinct minima (Fig.2.13), one metastable at roughly c/a=0.97 (vertical compression ~3%), and one stable at c/a=1.09, corresponding to a vertical espansion of 9%. The c/a compression or elongation stems entirely from a Jahn-Teller distortion of the Cu-centered octahedron. The two minima are separated by a sharp maximum near c/a=1, related to the unresolved degeneracy of the partially occupied e_g doublet. In each of the two minima, the degeneracy is broken in favor of one of the e_g orbitals.

Examining the density of states (DOS) projected on Cu e_g orbitals for AF-II at c/a=1.09 in Fig.2.14, we see that the empty minority state on Cu has essentialy pure $d_{x^2-y^2}$ character, i.e. there is a $d_{x^2-y^2}$ magnetic orbital ordering at the absolute

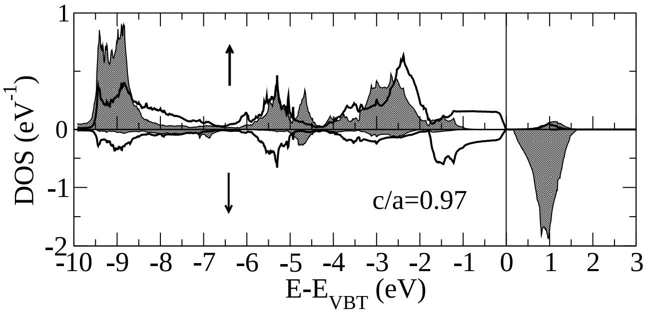

Figure 2.15: Density of states of CuO projected on Cu e_g orbitals at the axially-compressed minimum. Energy zero is the valence band top. Thick solid line: $d_{x^2-y^2}$; thin solid line, shaded curve: d_{z^2}. The antiferromagnetically-split Cu hole is almost pure d_{z^2}. The spin splitting is similar to that in Fig.2.14.

structural-energy minimum. Instead, the DOS in the metastable vertically-compressed minimum in Fig.2.15 shows that the polarized hole has d_{z^2} character, and hence a d_{z^2} magnetic orbital ordering. The gap increases monotonically from about 0.2 eV at c/a=0.96 to 2 eV at c/a=1.35. In the AF-II structure at the equilibrium c/a=1.09, the gap is 1.1 eV. It opens between mostly O p valence and purely Cu d empty states, which qualifies this variant of CuO as a charge transfer Mott insulator. The calculated Cu magnetic moment in the AF-II structure is about 0.6 μ_{B} at both structural minima, quite in line with the moments usually found computationally in cuprates [65, 66, 67, 68].

Our main structural prediction is that c/a elongates by nearly 10%, a sizable Jahn-Teller effect by any standard. However, a c/a of over 1.35, i.e. a 35% expansion, has been inferred from diffraction measurements [6]. We opine that this is a strikingly, perhaps unreasonably, large number. The argument [6] that the volume per formula unit of elongated rocksalt at c/a=1.35 would be the same as in tenorite is hardly compelling. The volumes of the cubic non-magnetic and polarized elongated structure (59 and 65 Å^3 per formula, respectively) are both far from the 80 Å^3 per formula of tenorite. The latter, however, is an open structure with locally tetrahedral coordination that naturally has a sizably larger specific volume than the close-packed octahedral rocksalt; this is similar, e.g., to Si in the diamond structure having a 20% larger volume per atom than in close-packed hcp or fcc [105]. A more robust proxy of bonding behavior in the various structures are Cu(2+)-O bond lengths. In cuprates, the latter cluster around 1.95-2 Å, and a Cu-O bond length of 2.65 Å as implied by experiment is quite out of the ordinary. To quote a fairly extreme example, in $YBa_2Cu_3O_7$ (YBCO), the only sizably anomalous bond length is apical O to in-plane Cu at 2.25 Å, an elongation originating from a dramatic apical distortion of the Cu-O pyramid with basal face on Cu-O planes, due to chain Cu's pulling apical oxigen as close as 1.80 Å. (We stress that our considerations apply to Cu(2+): trivalent Cu can indeed establish Cu-O bonds as long as 2.75 Å. However, mixed valence is not expected in bulk CuO.)

Since in Fig.2.13 the in-plane lattice constant is that of $SrTiO_3$ substrate as in experiment, the Jahn-Teller vertical elongation is coupled to a lateral constraint. We estimated that the minimum energy for *free-standing* AF-II CuO in the expanded basin is at (a,c)=(3.79,4.30) Å, vs. the epi-constrained (a,c)=(3.905,4.25) Å. (In passing, this suggests e.g. $LaAlO_3$, a=3.79 Å, as a substrate for CuO growth.) The vertical distortion is only slightly larger in the free-standing case, with comparable Cu-O bond lengths of 2.15 Å (free-standing) vs 2.125 Å (epitaxial), both very far from 2.65 Å. (We also have searched for off-plane distortions and buckling in the various structures, but found none.) Our present results, therefore, are circumstantial evidence that tetragonal-rocksalt CuO should have a bulk c/a closer to 1.1 than to the 1.35 reported so far experimentally for films [6]. The latter c/a value might be due to surface and interface effects, given that the films in question are ultrathin.

We now discuss magnetic couplings and ordering temperatures, motivated by the suggestion [6] that CuO in the rocksalt structure may have a Neél temperature T_N around 900 K, much larger than all other monoxides and than tenorite CuO. The lowest-energy AF-II structure can be seen as two interpenetrating AF simple-cubic sublattices, as shown in Fig.2.16. There are two independent magnetic couplings in the basal plane, and two more in the vertical planes. (This holds also for AF-4: the differences with AF-II are schematized in Fig.2.17.) The couplings within each sublattice ($J_{\|}$ in the basal plane and $J_{\perp}$ along the c axis) originate from O-mediated super-exchange between Cu's that are second neighbors on the full lattice. The two sublattices are coupled by the "diagonal" terms $J_{d\|}$ in the basal plane and $J_{d\perp}$ in the vertical planes. As easily seen by inspection, in the expression of the magnetic energy for AF-II the terms involving diagonal J's cancel out, which cures the apparent frustration in this structure. Therefore, the relevant ordering temperature can be estimated for each sublattice separately. As shown below, the intra-lattice couplings are AF and anisotropic (one J

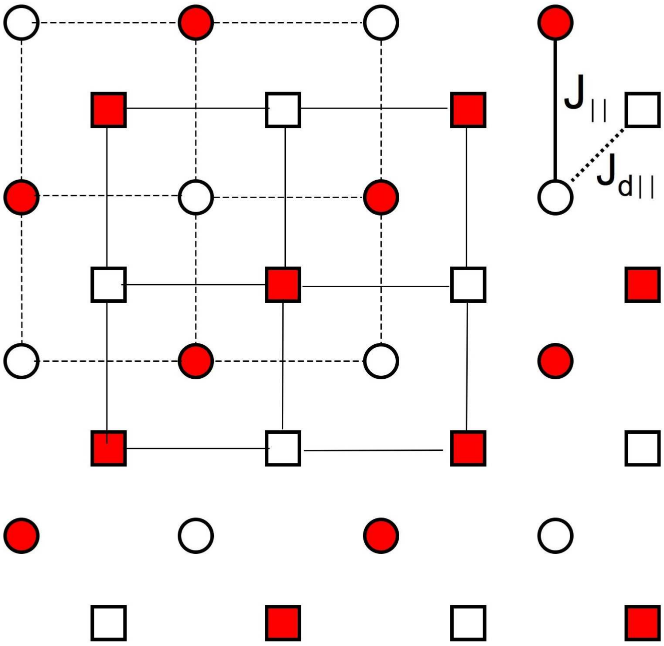

Figure 2.16: Schematic basal (xy)-plane view of the AF-II (or equivalently AF-4) structure. Filled and empty symbols indicate up or down spin. Square and circles are Cu atoms belonging to the two cubic AF sublattices discussed in the text. The intra sub-lattice AF coupling is named $\mathrm{J}_{||}$ and the inter-sublattice coupling is named $\mathrm{J}_{\mathrm{d}||}$. Note that the apparent frustration is avoided in this structure because the contributions involving $\mathrm{J}_{\mathrm{d}||}$ cancel. The vertical xz plane is obviously equivalent upon exchange of $||$ by $\perp$, and allowance for the different numerical value of the J's. Oxygens (not drawn) sit at the crossings of the two nets.

is one fifth of the other). Thus each sublattice can be mapped onto an anisotropic Ising model (three-dimensional, simple-cubic, antiferromagnetic).

The coupling parameters are calculated from the total energies of the various magnetic phases as

$$\begin{aligned}
\mathrm{J}_{||} &= (2E_{\mathrm{AF\ II}} - E_{\mathrm{AF\ G}} - E_{\mathrm{AF\ A}})/2 \\
\mathrm{J}_{\perp} &= E_{\mathrm{AF\ II}} - E_{\mathrm{AF\ 4}} \\
\mathrm{J}_{\mathrm{d}||} &= (E_{\mathrm{AF\ G}} - E_{\mathrm{AF\ A}})/2 \\
\mathrm{J}_{\mathrm{d}\perp} &= (E_{\mathrm{AF\ 4}} + E_{\mathrm{AF\ A}} - E_{\mathrm{FM}} - E_{\mathrm{AF\ II}})/2.
\end{aligned} \tag{2.1}$$

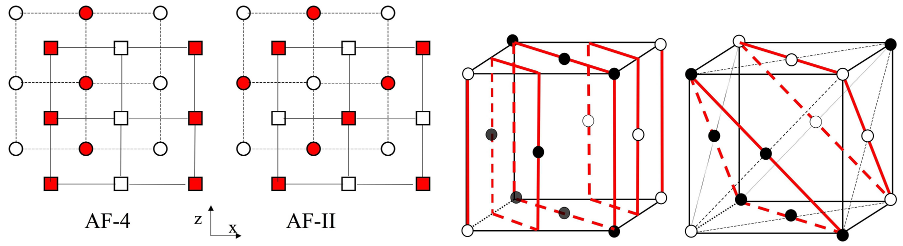

Figure 2.17: Top: stacking sequence of the AF-II (right) and AF-4 structures (left) viewed in the vertical (010) plane the c axis being (001)). Bottom: alternate view of AF-II (right) and AF-4 (left) as, respectively, (111)-oriented monolayer and (110)-oriented bilayer AF-A structures. Filled and empty symbols are up and down Cu's. Oxygens are not shown.

The calculated parameters are $J_{\parallel}$=–28.4 meV, $J_{d\parallel}$=–27.3 meV, $J_{\perp}$=–5.6 meV, and $J_{d\perp}$=2.5 meV. The anisotropy ratio is $J_{\perp}/J_{\parallel}$=0.197, i.e. as anticipated the system is strongly two-dimensional in terms of magnetic interaction.

$J_{\parallel}$	$J_{d\parallel}$	$J_{\perp}$	$J_{d\perp}$
–28.4	–27.3	–5.6	2.5
T_N(Ising)		T_N(Weiss)	
plain	rescaled	plain	rescaled
530	300	725	410

Table 2.1: In-plane (‖) and vertical (⊥) magnetic couplings (meV) and Neél temperatures (K) for Jahn-Teller-distorted CuO in the AF-II structure.

A simple estimate of the Néel temperature can be obtained [106] by a modified Weiss formula: we find T_N=725 K for AF-II. Applying Anderson's rescaling [106, 107] this estimate drops to 410 K. Since the present system is quite anisotropic, a formula born of isotropic classical models may not apply. We therefore employ results for the anisotropic Ising model. The critical temperature is a maximum in the isotropic case (1500 K for our calculated maximum J), and drops [108, 109] with increasing anisotropy, as one would intuitively expect. From renormalization-group data [110] on the anisotropy dependence of the critical temperature, we infer a Néel temperature of 530 K at the calculated ratio $J_{\perp}/J_{\parallel}\simeq$0.2. Upon Anderson scaling, T_N drops to 300 K. The data are collected in Tab.2.1. It appears that the present estimates (except to some extent for the unscaled Weiss formula) do not confirm the suggestion about a Neél temperature of rocksalt CuO much larger than in other transition-metal oxides.

This is clearly expected given the strong anisotropy of in-plane and vertical coupling, and the weakness of the latter.

In Fig.2.18 we compare our calculated valence DOS with the UPS peak positions [6]. The general shape and energy positions (see Ref.[6]) are in fair, though not especially striking agreement with experiment. On the other hand, if our conjecture about the possible interface and surface-induced expansion of the measured sample is correct, our DOS and the UPS spectrum should not necessarily agree, and this imperfect matching is not too disturbing.

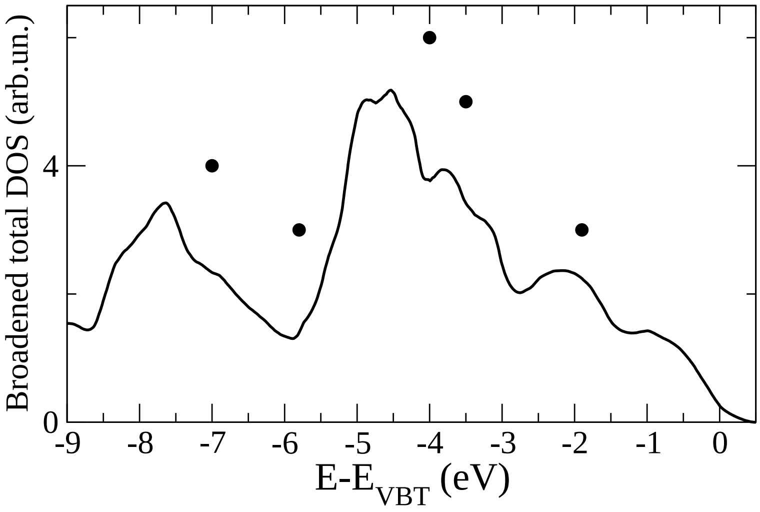

Figure 2.18: Valence density of states compared with UPS peak positions. The DOS is broadened by a running average procedure.

In a recent paper Grant [111] studied rocksalt CuO using LDA+U. He finds that both a substantial U (6 eV, which e.g. we also found to be the minimal value needed to open a gap in $YBa_2Cu_3O_6$) and a tetragonal distortion are needed to open a gap in the spectrum. He investigated only the expanded-c/a basin of the magnetic phase, finding a shallow structural minimum at about c/a=1.2, somewhat closer to our value than to experiment. The vertical Cu-O bonds of 2.35 Å are reasonable, though still somewhat large. The value of U suggested by our calculations (over 9 eV) is larger than that used by Grant: whether and how much U affects structure is an open question.

2.2.2 Conclusions

The results of another theory study [112] based on a hybrid functional are qualitatively comparable to ours, with important differences. Two d_{z^2} and $d_{x^2-y^2}$–orbitally ordered minima are obtained under compression and expansion, but at very different in-plane lattice constants. (We did not use the latter as a parameter, but took it as fixed by experiment: as mentioned, a hypothetical cubic CuO has the same lattice constant as the substrate.) The expanded c/a value of 1.36 is close to experiment, and the gap at that c/a is 2.7 eV (1.5 eV in the compressed configuration), both quite large compared to ours. The J's deduced from total-energy differences are also very different from ours, which is a token of the different energetic order of the various structures found by the hybrid functional.

In summary PSIC calculations show that metallic rocksalt CuO stabilizes by Jahn-Teller distortion at c/a=1.09 in an AF-II magnetic arrangement with $d_{x^2-y^2}$ orbital ordering and a charge-transfer gap of 1.1 eV. The Jahn-Teller distortion of the Cu-centered octahedra is a sizable 10%. Given our results, and other typical Cu-O bond lengths in cuprates, we suggest the 35% expansion reported in experiment may be due to interface and surface effects. We estimate relatively low Neél temperatures (between 300 by anderson59-rescaled anisotropic Ising model, and 750 K by unrescaled Weiss formula) due to the strong anisotropy of magnetic couplings, hence we do not support the suggestion of high Neél temperature in tetragonal-rocksalt CuO.

3

Magnetic titanates

This Chapter is devoted to the application of the VPSIC formalism for the analysis of magnetic perovskites $YTiO_3$ *and* $LaTiO_3$*. The main part of the following discussion is published in the APS Journal "Phys. Rev. B, 84 (195127), 2011 [5]". I only report the part of the long VPSIC paper to which I contributed, in particular my contribution is about the 50% of this part. The writing and preparation of the paper was done collaboratively with coworkers and supervisors, as did the planning and assessment of the work.*

3.1 Introduction

Titanates characterized by the nominal Ti d^1 configuration rank among the most peculiar and intriguing magnetic perovskites. At variance with the more investigated classes of manganites and cuprates whose fundamental chemistry is governed by 3d e_g states, in titanates the 3d valence states are 3d t_{2g}, thus orbitals not directly oriented towards the oxygens; this produces a much weaker p-d hybridization and crystal field splitting than in e_g systems. However, experiments show that the phenomenology of these systems may be crucially affected by small structural details.

A nice illustration of this over-sensitive magnetostructural coupling is the compared study of $YTiO_3$ (YTO) and $LaTiO_3$ (LTO): both systems are Pnma perovskites, with relatively small Jahn-Teller (JT) distortions and large GdFeO-type octahedral rotations; the difference in cation size (with La bigger than Y) causes larger distortions and rotations in YTO than in LTO (in agreement with the well known space-filling criterion), in turn leading to quite a different magnetic behaviour: YTO is ferromagnetic [113, 114, 115] with low Curie temperature T_c=30 K, sizable band gap (∼1eV) and magnetic moments M=0.8 μ_B, in line with a Ti d^1 ionic configuration; LTO, on the other hand, is antiferromagnetic G-type [116] with T_N=130K, very small energy gap (∼0.3 eV) and sensibly smaller magnetic moments (∼0.57 μ_B)[117]. A long-standing debate centers this much reduced magnetic moment and the nearly isotropic spin-wave dispersion in $LaTiO_3$ [118]. It was pointed out that a single electron in the triple-degenerate t_{2g} manifold can fluctuate giving rise to an exotic "orbital liquid" state[119, 120]. However this faschinating hypothesis is contrasted by a series of evidences[116, 117, 119, 121, 122, 123, 124] that crystal field splitting is actually not small enough to keep the t_{2g} degeneracy unlifted, and instead a Jahn-Teller distorted, orbital-ordered state is realized in LTO, as well as in YTO.

Needless to say, these issues stimulated a long series of attempts to describe the titanates by a variety of ab-initio approaches, including LSDA[125], LDA+U [126, 127], and several LSDA+DMFT implementations[128, 129, 130]. While our description reproduces, at least in part, some of the previous findings, our results are especially valuable as they account for properties on purely ab-initio grounds, in the framework of the same theory, and without system-dependent parameters (e.g. U, J).

After the description of the methodology (Sec.3.2), we illustrate the electronic properties of YTO (Sec.3.3), calculated at the experimental structure, as prototype of "basic" t_{2g} system. We then discuss the more peculiar LTO, highlighting the differences with respect to YTO (Sec.3.4). In Sec.3.5 we discuss the structural properties of both systems, rationalizing their different behavior, and sum up in Sec.3.6. Notice that LSDA does not reproduce the Mott-insulating behaviour for these systems, and in fact predict an unphysical non magnetic, metallic electronic ground-state.

3.2 Technicalities

Calculations are carried out with ultrasoft pseudopotentials [76] and a plane-wave basis set with cut off ranging from 30 to 35 Ryd, 6×6×6 special k-point grids for self-consistent calculations, 10×10×10 special k-points and linear tetrahedron interpolation method for density of states. The Ceperley-Alder-Perdew-Zunger local-density approximation is used for the exchange-correlation functional. Structural relaxations are carried out with a convergence threshold of 1 mRy/Bohr on the calculated forces.

3.3 Electronic properties of $YTiO_3$

In Fig.3.1 the orbital-resolved DOS of YTO is shown. The occupied DOS have two major contributions: at VBT there is a ~0.8 eV-wide fully spin-polarized DOS peak of Ti 3d states (residually hybridized with a small O 2p portion). Despite the nominal Ti^{3+} d^1 configuration, a certain amount of Ti d-O p hybridization is clearly visible (notice the different scale of Ti 3d and O 2p DOS: here the O 2p weight is way smaller than, e.g. in manganites). It follows that the calculated static charges and magnetic moment differ considerably from their nominal values (for Ti we obtain ~1.6 and ~0.7 electrons for up and down-polarized 3d state, respectively, and M=0.92 μ_B, a bit larger than the observed 0.8 μ_B). Below the Ti 3d peak there is a broader, unpolarized DOS of O 2p character spanning the energy interval between -4 eV to -8 eV (not shown in Figure). The CBB bands are also dominated by and large Ti 3d t_{2g} states, residually hybridized with O 2p and Y 4d orbitals. Thus we can unquestionably categorize the system as a true Mott-Hubbard insulator, at variance with most manganites or cuprates that are actually charge-transfer insulators or in the intermediate regime (more later on this important point).

In the band energy plot of FM YTO (Fig.3.2, left panel) we see four occupied bands (one for each Ti) separated from the 3d empty conduction bands by 1.8 eV. The fundamental gap only involves majority, and is direct at Γ. The CBB bands are ~1 eV wide. According to our calculations, the sharp DOS peak at the valence top is a complex admixture of the five Ti 3d orbitals. To assess quantitatively the identity of this state, we diagonalized the corresponding $P^{\sigma}_{mm'}$ (Eq.1.23) density matrix in the 3d orbital subspace. The results are reported in Tab.3.1 for two coordinate systems: the orthorhombic Pnma $\sqrt{2}\times\sqrt{2}\times 2$ (x′,y′,z′), and the conventional cubic(x,y,z), which differ by a 45° rotation[131] of the(x,y) plane. The Ti at (0,0,0) in the cubic reference system of YTO, shows prevailing contributions of $|yz\rangle$ and $|xy\rangle$ orbitals; however, not completely discardable e_g contributions are present as well. The charge density isosurface plot (Fig.3.4 left panel) confirms that this state can be expressed as $|\Psi_1\rangle \sim 0.75|yz\rangle + 0.56|xy\rangle$. Also evident is the resulting orbital ordering: co-planar

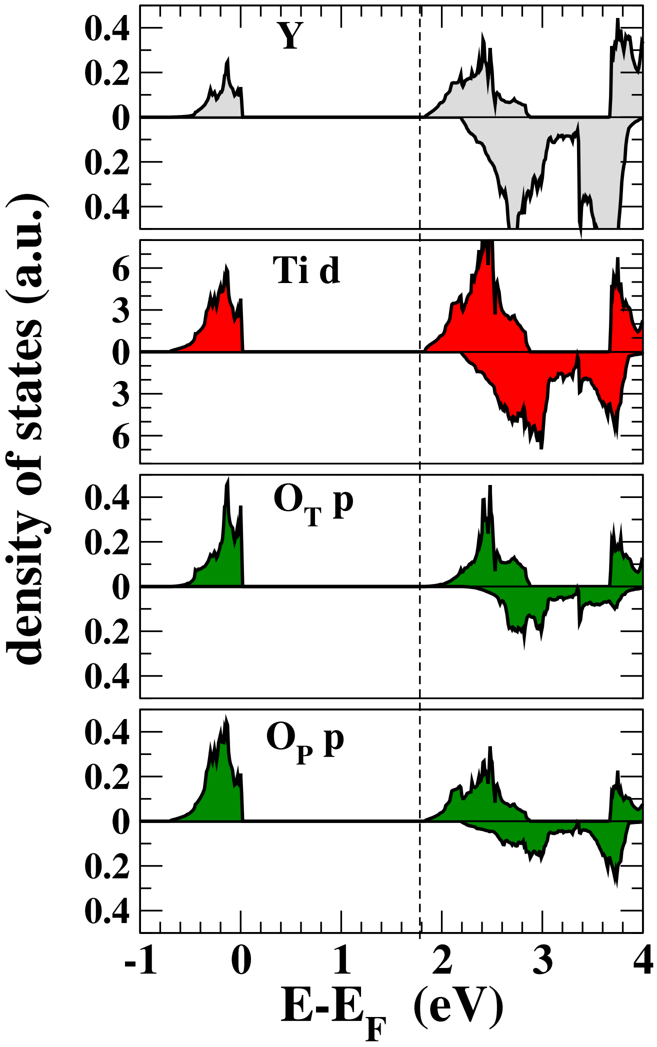

Figure 3.1: Orbital-resolved DOS for YTO - Orbital-resolved DOS for FM YTO. For clarity only Ti 3d, Y 5d, and O 2p are showed (oxygens on-top and in plane with Ti are labelled O_T and O_P, respectively). Notice that Y and O DOS are magnified by more than one order of magnitude with respect to the dominant Ti 3d DOS.

states shows an alternance of dominant $|yz\rangle$ and $|xz\rangle$ contributions, plus a change of sign for $|xy\rangle$ which causes the lobes of $|yz\rangle$ (or $|xz\rangle$) to lean back and forth towards the (x,y) plane (e.g. $|\Psi_2\rangle \sim 0.75|xz\rangle - 0.56|xy\rangle$). On the other hand, states aligned along z only differ by the alternance of $|xy\rangle$ sign, thus $|\Psi_3\rangle \sim 0.75|yz\rangle - 0.56|xy\rangle$, $|\Psi_4\rangle \sim 0.75|xz\rangle + 0.56|xy\rangle$. Our results are in excellent agreement with the finding of linear dichroism x-Ray absorption [132] which gives 0.8 and 0.6 for the coefficients of the two most occupied t_{2g} orbitals [133], and with LDA+DMFT [128] which obtains 0.78 and 0.62, respectively.

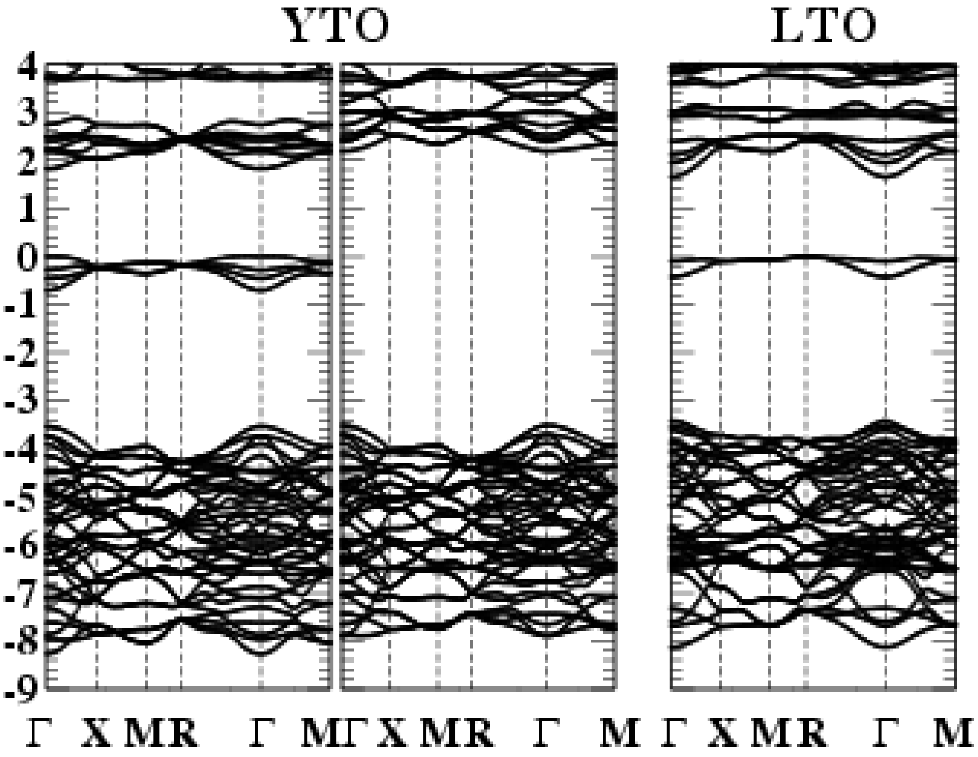

Figure 3.2: Band YTO and LTO - (Left panel) Band energy (spin up and spin down) of FM YTO and (right panel) AF-G LTO

3.4 Electronic properties of LaTiO$_3$

Remarkable differences from YTO emerge from the calculated DOS (Fig.3.3) and band structure (Fig.3.2): the fundamental band gap is a bit smaller for LTO but still quite sizeable (1.6 eV); furthermore, the latter is much flatter than in YTO: the occupied

3d states at VBT now span a much narrower energy range (0.4 eV instead of 0.8 eV), and the hybridization with the oxygens is smaller, although still well visible. Even the conductions bands in LTO appear flatter, and in fact they are separated in two groups by a gap of 0.2 eV. The magnetic moment is 0.89 μ_B, similar to YTO.

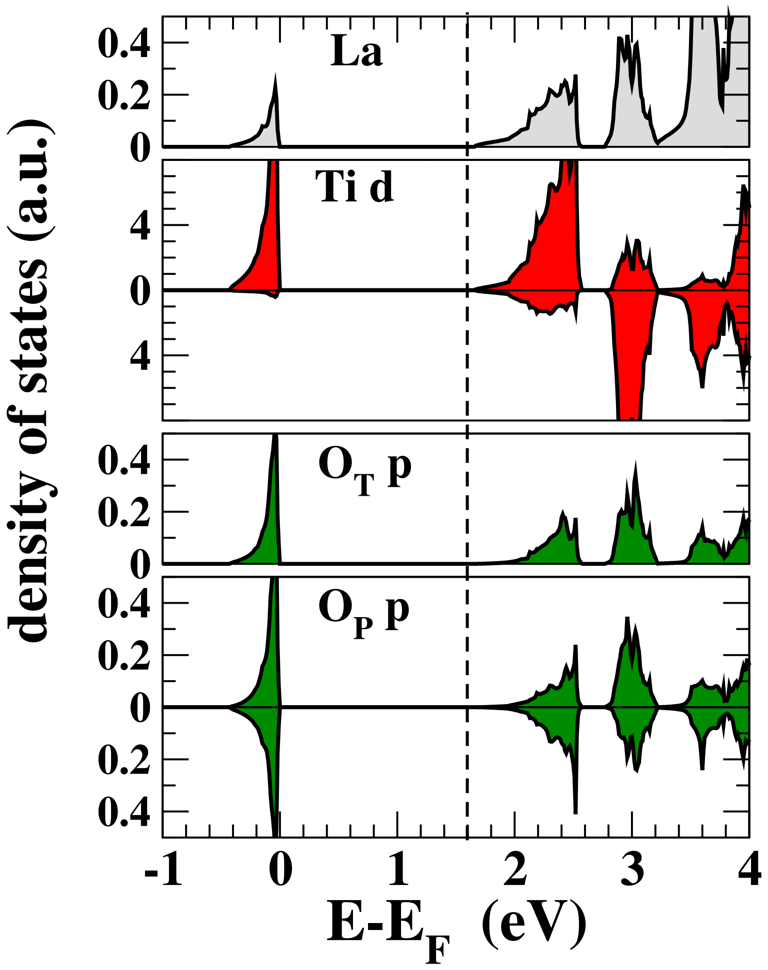

Figure 3.3: Orbital-resolved DOS for AF G-type LTO - Orbital labels are the same as in Fig.3.1. La and O_T states are spin-compensated, due to AFG symmetry. La and O DOS are magnified by more than one order of magnitude with respect to the dominant Ti 3d DOS.

The difference with YTO, is also borne out by the analysis of the diagonalized density matrix in Tab.3.1. In the cubic reference system, at variance with YTO we see that the e_g contribution is now almost vanishing, and the occupied states are almost purely t_{2g}. Moreover, the diversification of the t_{2g} occupancies is much reduced with respect to YTO as a results of the smaller rotations. Indeed this state approximately resembles cigar-shaped [111]-directed lobes, resulting from a nearly even t$_{2g}$ combination, as confirmed by the corresponding charge density isosurface plot in Fig.3.4, right panel. Notice that if t$_{2g}$ coefficients were exactly the same, Ψ_1 and Ψ_2, as well as Ψ_3 and Ψ_4, would be identical, and the resulting cigars in each plane parallel to each other, pointing all along [111].

	$\vert x'y'\rangle$	$\vert x'z'\rangle$	$\vert y'z'\rangle$	$\vert z'^2\rangle$	$\vert x'^2-y'^2\rangle$
YTO					
Ti 1	0.11	0.48	0.58	0.33	0.56
Ti 2	0.11	0.48	-0.58	-0.33	-0.56
Ti 3	-0.11	0.48	0.58	-0.33	-0.56
Ti 4	-0.11	0.48	-0.58	0.33	0.56
LTO					
Ti 1	0.02	0.15	0.78	0.08	0.60
Ti 2	0.02	0.15	-0.78	-0.08	-0.60
Ti 3	-0.02	0.15	0.78	-0.08	-0.60
Ti 4	-0.02	0.15	-0.78	0.08	0.60
	$\vert xy\rangle$	$\vert xz\rangle$	$\vert yz\rangle$	$\vert z^2\rangle$	$\vert x^2-y^2\rangle$
YTO					
Ti 1	0.56	-0.07	0.75	0.33	0.11
Ti 2	-0.56	0.75	-0.07	-0.33	0.11
Ti 3	-0.56	-0.07	0.75	-0.33	-0.11
Ti 4	0.56	0.75	-0.07	0.33	-0.11
LTO					
Ti 1	0.60	-0.45	0.66	0.08	0.02
Ti 2	-0.60	0.66	-0.45	-0.08	0.02
Ti 3	-0.60	-0.45	0.66	-0.08	-0.02
Ti 4	0.60	0.66	-0.45	0.08	-0.02

Table 3.1: 3d orbital decomposition of the four occupied states (one for each Ti) at VBT of YTO and LTO. Coordinates (x',y',z') and (x,y,z) refers to orthorhombic and conventional cubic cartesian axes, respectively, as indicated in Fig.3.4.

While the orbital charge distribution in YTO and LTO is so different, and causes much of their macroscopic differences, the relative ordering is the same: even for LTO, in the plane there is perfect alternance (i.e. chessboard-like order) of leading $|xz\rangle$ and $|yz\rangle$ contributions (this is less evident than in YTO since the t_{2g} coefficients are not as different as in YTO), plus a sign alternance for $|xy\rangle$. Along z only the sign alternance occurs. Our calculated t_{2g} coefficients are remarkably close to the values (0.56, 0.45, 0.69) measured by NMR spectra in Ref.[119], as well as those calculated by a model Hamiltonian (0.6, 0.39, 0.69) in Ref.[116].

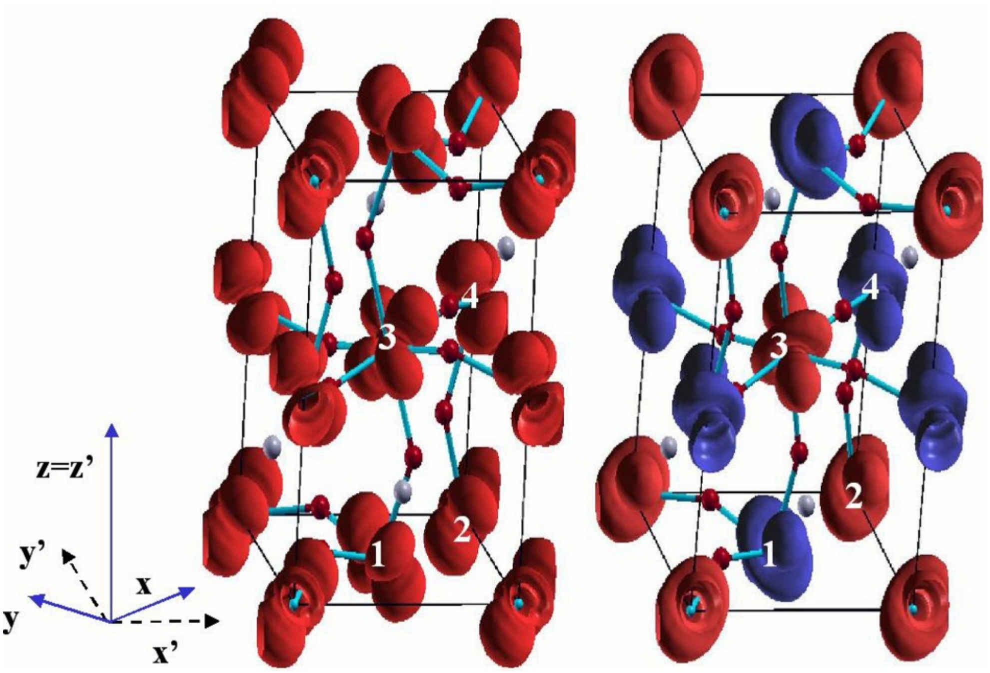

Figure 3.4: Charge density isosurface of YTO and LTO - Charge density isosurface $n_{\pm}=\pm$ 0.01 electrons/cm^3) of the upmost occupied state for FM YTO (left) and AF-G LTO (right). Red (light) and blue (dark) surfaces represent spin majority (+) and minority (-) contributions, respectively. On this scale only Ti d contributions are visible (oxygen contributes residually, see the DOS in Figs.3.1 and 3.3). Both YTO and LTO are orbital-ordered, i.e. the four Ti atoms in the cell have same integrated charge but different orbital distribution (numbers connect each Ti with the corresponding 3d orbital decomposition reported in Tab.3.1).

The observed magnetic ground-state is correctly predicted for both systems: for YTO the FM energy is lower than AF-G and AF-C phases by 10.1 meV/f.u. and 8.3 meV/f.u., respectively (in agreement with previous LDA+U results [126] with $U-J$ =3.2 eV). For LTO, on the other hand, we obtain the AF-G phase lower than FM and AF-A phases by 15.2 meV/f.u. and 10.05 meV/f.u., respectively. Fitting the energies on a 2-parameter nearest-neighbor Heisenberg Hamiltonian:

$$H = -\frac{1}{2}\sum_{i}\left[J_{pl}(\hat{S}_i \cdot \hat{S}_{i+x} + \hat{S}_i \cdot \hat{S}_{i+y}) + J_z \hat{S}_i \cdot \hat{S}_{i+z}\right] \tag{3.1}$$

where $i + x$, $i + y$, and $i + z$ indicate nearest neighbors of i in the x,y, and z directions, respectively, we obtain J_{pl} = 4.15 meV and J_z = 1.8 meV for planar and orthogonal exchange interaction parameters in YTO, respectively; J_{pl} = −5.02 meV and J_z = −5.03 meV for the same quantities in LTO. These results nicely confirm the analysis of the orbital ordering: while a remarkable anisotropy is present in YTO, LTO is substantially isotropic.

3.5 Structural properties

Tab.3.2 shows experimental and VPSIC-calculated atomic coordinates and the most important structural parameters, i.e. Ti-O-Ti angles (θ), and Ti-O distances, indicated in Fig.3.5.

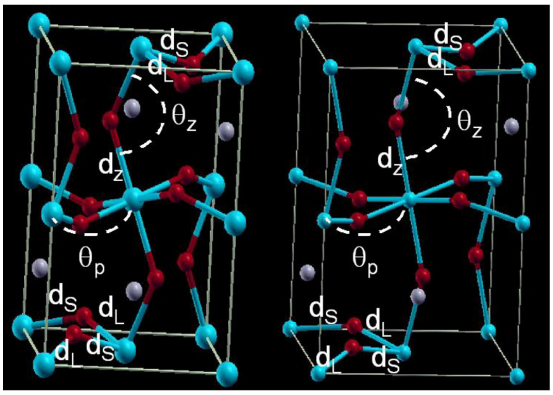

Figure 3.5: Pnma structure of YTO (left) and LTO (right). Cell parameters are fixed to experimental values, while atomic positions were relaxed according to VPSIC. Labels indicate Ti-O-Ti angles and Ti-O distances in plane (θ_p, d_p) and along z (θ_z, d_z). Results are reported in Tab.3.2.

In-plane there are two types of Ti-O bonds, long (d_L) and short (d_S), which alternate along both x and y directions (see Fig.3.5), while along z there is only one $d_z \sim d_S$. These values easily rationalize the chessboard-like Ti d ordering: on each Ti the occupied state

	x/a	y/b	z/c
Y	0.478 (0.479)	0.073 (0.073)	1/4
Ti	0	0	1/2
O_I	-0.139 (-0.121)	-0.063 (-0.042)	1/4
O_{II}	0.307 (0.309)	0.184 (0.190)	0.067 (0.058)
La	0.491(0.493)	0.053(0.043)	1/4
Ti	0	0	1/2
O_I	-0.080(-0.081)	-0.008(-0.007)	1/4
O_{II}	0.0288(0.291)	0.204(0.206)	0.042 (0.043)

	d_S	d_L	d_z
YTO	2.0(2.02)	2.13(2.08)	2.07(2.02)
LTO	2.02(2.03)	2.06(2.05)	2.02(2.03)

	θ_p	θ_z
YTO	140.41^o (143.62^o)	133.30^o (140.35^o)
LTO	153.82^o (152.93^o)	154.30^o (153.75^o)

Table 3.2: Atomic positions in crystal coordinates (x/a, x/b, x/c), and main structural parameters (Ti-O-Ti angles in plane (θ_p) and along z (θ_z), Ti-O distances along z (d_z) and in-plane (the shorter d_S and the longer d_L) bonds) for Pnma $YTiO_3$ and $LaTiO_3$ calculated by VPSIC, in comparison with the experimental data (in parenthesys). Cell structures are fixed to the experimental values a=5.316 Å, b=5.679 Å, c=7.611 Å for YTO, a=5.640 Å, b=5.584 Å, c=7.896 Å for LTO[117].

prefers to lie along the longer Ti-O bond (thus alternatively $|xz\rangle$ and $|xy\rangle$ for d_L parallel to x, or $|yz\rangle$ and $|xy\rangle$ for d_L parallel to y). For YTO the difference between d_L and d_S is quite sizeable, and give rise to a very pronounced ordering, as seen in the analysis of the charge density. For LTO the d_L and d_S difference is much reduced, and so is the planar chessboard ordering, indeed. Notice that for both materials the JT-type structural distortions are minor, i.e. properties along x, y, and z are, on average, almost the same (especially for LTO). The GdFeO-type tiltings and rotations, on the other hand, are quite sizable and represent the major factor determining the observed structures and the consequent splitting of the t_{2g} triplet state. Finally, the VPSIC-calculated structure is satisfactorily close to experiment for both LTO and YTO (although for the latter oxygen rotations are a bit overemphasized along z).

3.6 Conclusions

In summary, VPSIC results furnish a coherent guideline to understand (at least part of) the differences between YTO and LTO, and correctly describe the different magnetic ordering of the two systems: The bigger GdFeO-type distortions of YTO produce crucial differences in electronic and magnetic properties, as evidenced by the results:

a) larger Ti 3d-O 2p and t_{2g}-e_g mixing;

b) crucially different charge density distribution around Ti;

c) an increase by factor ∼2 of the occupied 3d state bandwidth. The wider rotations, in particular, destabilize the AF superexchange coupling which prevails in a purely d^1 t_{2g} unrotated Pnma environment.

Notice that the above considerations are completely reverted for doped manganites, whose chemistry is governed by e_g: in that case cubic symmetry and absence of octahedral rotations works in favor of e_g-p hybdridization. In titanates, on the other hand, absence of octahedral rotations means vanishing p-d hybridization, pure t_{2g} charge character, and minimal t_{2g} bandwidth.

It remains to explain the large difference between our calculated and the measured energy gap. This actually occurs by construction: our VBT and CBB band energies represent removal and additional energies, and their difference estimates the on-site Coulomb energy U, whereas the lowest excitation measured for these true Mott-Hubbard insulators is an intra-site excitation energy which of course does not include U. The attempt to argument a presumed smallness of U on the basis of the very tiny energy gap of $LaTiO_3$ [124] is a misinterpretation. In fact, according to our band structure U∼3 eV, as expected for a system of this kind. It is also not very proper the strategy carried out in several works of estimating the excitation energy as LDA-calculated t_{2g} (average) band splitting: this is justified by the fact that in the limit of vanishing U (i.e. delocalized electrons) excitation and additional/removal energies go back to be the same quantities; however we must keep in mind that here the vanishing of U is an artifact of the LDA, not a true feature of the titanate. A more rigorous strategy to evaluate the lowest excitation energy is suggested in [127] where a suited

Hamiltonian for the excited state is constructed in such a way to project out the electronic ground state. Here we do not pursue this route which overcomes the capability our actual methodological setting, and leave to future developments the investigation of the crystal-field splitting and orbital-liquid state in LTO by VPSIC. However, we emphasize that the rationalization of the FM vs. AF G-type competition is correctly described already at the level of our ground-state results.

4

Transition metal monoxides

The main part of the following discussion is published in the APS Journal "Phys. Rev. B, 84(115114), 2011 [134]". In this section my operational contribution was essentially the LDA and VPSIC calculation while the HSE and Montecarlo parts were the results of C. Franchini and R. Tiwari calculations. The writing and preparation of the paper was done collaboratively with coworkers and supervisors, as did the planning and assessment of the work.

4.1 Introduction

The relative simplicity of structural and magnetic ordering and the abundance of available experimental and theoretical data elect transition metal monoxides (TMO) as favorite prototype materials for the *ab initio* study of exchange interactions in Mott-like insulating oxides [107]. TMO are known to be robust antiferromagnetic (AF) Mott-like insulators with sizable exchange interactions and Néel ordering temperatures. The accurate determination of magnetic interactions purely by first-principles means is a remarkable and as yet unsolved challenge [135, 136, 137]. The difficulty stems, on the one hand, from fundamental issues in the description of Mott insulators by standard density functional theory (DFT) approaches, such as local-spin density approximation (LDA) or the generalized gradient approximation (GGA). On the other hand, the determination of low-energy spin excitations require a meV-scale accuracy; however, the error bar due to specific implementation and technical differences may easily be larger.

A large amount of theoretical work for TMO has amassed over the years. A number of studies were carried out in particular for MnO and NiO with a variety of advanced methods: the LDA+U [82, 135, 138, 139, 140, 141], GGA+U [142, 143], the optimized effective potential (OEP) [135], the quasiparticle Green function (GW) approach [137, 144, 145], several types of self-interaction corrected LDA (SIC-LDA) [21, 24, 146, 147, 148, 149], Hartree-Fock [150, 151, 152, 153] and several types of hybrid functionals such as B3LYP [153, 154, 155], PBE0 [152, 156, 157], Fock-35 [153], and B3PW91 [156]. From a methodological viewpoint, Refs. [135, 147, 158] are particularly relevant for our present purposes, because of the systematic comparison of diverse approaches to computing magnetic interactions. Other studies [159, 160, 161] focused in particular on pressure-induced high-to-low spin magnetic collapse observed at very high pressure (∼150 GPa for MnO) and relevant to Earth-core geophysics. Here we will not, however, be concerned with the phenomenology of this specific phase transition.

In this Chapter we present a detailed analysis of MnO and NiO magnetic properties on a wide range of lattice parameters (i.e. hydrostatic pressures) carried out by standard and advanced first-principles methods. In particular, our theoretical front-liners are two approaches proposed recently for the description of strongly-correlated systems: the Heyd, Scuseria and Ernzerhof (HSE) hybrid functional approach [162, 163, 164], and the VPSIC [5], implemented in plane-wave basis set plus ultrasoft [76] pseudopotentials. To provide a baseline for their evaluation, we complement these methods by their local counterparts implemented in the same methodological setting, namely LDA in plane-waves and ultrasoft pseudopotentials (reference for VPSIC) and GGA in the Perdew-Becke-Ernzerhof [165](PBE) version (reference for HSE). Performing the same set of calculations in parallel with different methods is instrumental to distinguish fundamental and methodological issues, and characterizes this work with respect to the many previous theoretical studies of TMO.

MnO and NiO in equilibrium conditions have a high-spin magnetic configuration and large (∼ 3.5-4 eV) band gap. Magnetic moments and exchange interactions depend crucially on the details of structural and electronic properties. The latter are characterized by a complex interplay of distinct energy scales: the crystal field splitting, which in rocksalt symmetry separates the on-site 3d e_g and t_{2g} energies; the charge transfer energy between O p and TM d states; the hopping energies between d-d and p-d states [166]. Ref.[135] convincingly shows that an empirical single-particle potential suitably adjusted to reproduce the experimental values of the above mentioned energies can deliver highly accurate magnetic interactions (moments and spin-wave dispersion). However, obtaining a correct balance of all these contributions is difficult even for advanced density functional methods, not to mention standard LDA or GGA, which fail altogether (to different extents depending on the specific compound). A general analysis of these failures and difficulties of *ab initio* approaches is beyond the scope of this work; we mention that the thorough analysis carried out in Refs. [135, 167] suggests that a single parameter, as adopted by the LDA+U, is not sufficient, while global multi-state energy corrections could serve this purpose. Both the advanced methods (HSE and VPSIC) adopted in this work, while quite different in spirit, act in terms of "global" corrections to local density functional energy spectrum, i.e. no a priori assumption is made about which particular state or band is in need of modification or correction.

MnO and NiO are both affected by SI, although to different extents [103]: severely for MnO, dramatically for NiO. Under positive (i.e. compressive) pressure the problem will be amplified, as any small band gap which may exist at equilibrium will be further reduced up to complete closure, and magnetic moments may be disrupted. Thus, a reliable description of TMO under pressure necessarily requires approaches overcoming the SI problem. Both VPSIC and HSE, although from different starting points, work towards the suppression of SI. The former explicitly subtracts the SI from the LDA functional; the latter, in a more fundamental manner, inserts of a portion of true Fock exchange in place of the local exchange functional, whose incomplete cancellation with the diagonal Hartree counterpart is the source of SI in LDA/GGA functionals [168]. The results will show that, despite the different conceptual origin, the two approaches deliver a consistent description of MnO and NiO, in fact with spectacular quantitative agreement in several instances.

The Chapter is organized as following: Sec.4.2 describes briefly the methodologies employed; in Sec.4.3, the model used to calculated the exchange-interaction parameters is discussed. Sec.4.4 illustrates our results at equilibrium (4.4.1) and under pressure (4.4.2). In Sec.4.4.2.2 and 4.4.2.3 we discuss the exchange interactions and critical temperatures, respectively. Section 4.5 offers some concluding remarks.

4.2 Methods

Our first-principles results are obtained by using two different codes: PWSIC [4] and VASP [71, 169]. With the PWSIC code, which uses plane-waves basis set and ultrasoft pseudopotentials we carry out calculations within LDA (hereafter LDA-PW) and VPSIC [5] (see Sec.1.4).

The VASP [71, 169] code, employing the projected augmented wave (PAW) approach, is used for PBE [165] and HSE [162, 163, 164] calculations. In the HSE method the short-range (sr) part of the exchange interaction (X) is constructed by mixing exact non-local Hartree-Fock exchange and approximated semi-local PBE exchange. The remaining contributions to the exchange-correlation energy, namely the long-range (lr) exchange interaction and the electronic correlation (C), is treated at PBE level only, resulting in the following expression:

$$E_{XC}^{HSE} = \frac{1}{4}E_X^{HF,sr,\mu} + \frac{3}{4}E_X^{PBE,sr,\mu} + E_X^{PBE,lr,\mu} + E_C^{PBE} \, . \tag{4.1}$$

The partitioning between *sr* and *lr* interactions is achieved by decomposing the Coulomb kernel ($1/r$, with $r = |\mathbf{r} - \mathbf{r}'|$) with a parameter μ, controling the range separation between the short (S) and long (L) range part

$$\frac{1}{r} = S_\mu(r) + L_\mu(r) = \frac{\mathrm{erfc}(\mu \mathrm{r})}{r} + \frac{\mathrm{erf}(\mu \mathrm{r})}{r} \, . \tag{4.2}$$

We have used here $\mu = 0.20$ Å^{-1}, in accordance to the HSE06 parameterization [170] and corresponding to the distance $2/\mu$ at which the short-range interactions become negligible. For $\mu = 0$, HSE06 reduces to the unscreened hybrid functional PBE0 [171, 172].

PWSIC calculations have been carried out in 16-atom face centered cubic (FCC) supercells [i.e. 8 formula units (f.u.)], cut-off energies of 40 Ry, reciprocal space integration over 6×6×6 and 10×10×10 special k-point grids for self-consistency and density of states calculations, respectively. VASP calculations have been performed using a 4 f.u. unit cell, an energy cut-off of 25 Ry, a 4×8×4 k-point mesh and a standard HSE mixing parameter a=0.25. Pressures have been evaluated using the Birch-Murnaghan equation of state [173].

Montecarlo simulations of the classical 2-parameter Heisenberg model have been carried out for a spin lattice system of size L=12 (i.e. N = L^3 total lattice sites).

We determined ground state magnetic ordering and critical temperature by simulated annealing for each pair of ab-initio-calculated J_1 and J_2 parameters characterizing the magnetic structure (see 4.3), at each lattice constant and for each method. In order to test finite-size effects on the results some annealing with L=20 was also performed. The annealing was done over 30 temperature points, starting from high temperature (roughly twice the critical temperature) down to T=0, with 10^6 sweeps at each temperature. The annealing protocol is the usual Metropolis algorithm based on single spin update.

4.3 Magnetic structures and the Heisenberg model

TMO have a rock-salt structure (see Fig.4.1), so each TM has 12 nearest-neighbor (NN) and 6 next-nearest neighbors (NNN). The NNN are connected through oxygen bridges, and their interaction J_2 is dominated by superexchange. On the other hand, NN interact via a typically smaller exchange coupling J_1 whose sign may depend on the specific TMO; J_1 involves direct TM-TM exchange (giving a robust AF contribution) and a 90°-oriented TM-O-TM superexchange (expected to be weakly FM). The observed ground state magnetic phase is antiferromagnetic (111) A-type, labeled AF_2 hereafter. It can be seen as a stacking of (111) planes of like spin alternating along the [111] direction, as illustrated in Fig.4.1. In AF_2 each TM has 6 spin-paired intra-(111)-plane NN and 6 spin-antipaired inter-(111)-plane NN; on the other hand, all 6 NNN bonds are inter-planar and antipaired. Thus, this configuration maximizes the energy gain associated to the NNN antiparallel spin alignment. As for beyond-NNN magnetic interactions, there is ample experimental [174] and theoretical [147] evidence that they can be safely discarded (e.g. according to inelastic neutron scattering [174] in NiO they are two order of magnitude smaller than the dominant J_2. We explicitly checked this with our code).

In order to evaluate J_1 and J_2 we need to consider at least two competing high-symmetry magnetic phases beside the observed AF_2. Natural choices are the ferromagnetic (FM) order and the AF (110) A-type order with (110) spin-paired planes compensated along [110] (labeled AF_1). AF_1 can also be seen as made of FM (001) planes alternating along [001] (see Fig.4.1). The AF_1 phase has all the 6 NNN spin-paired, 4 of the NN spin-paired, and 8 NN spin-antipaired. On the other hand, it is

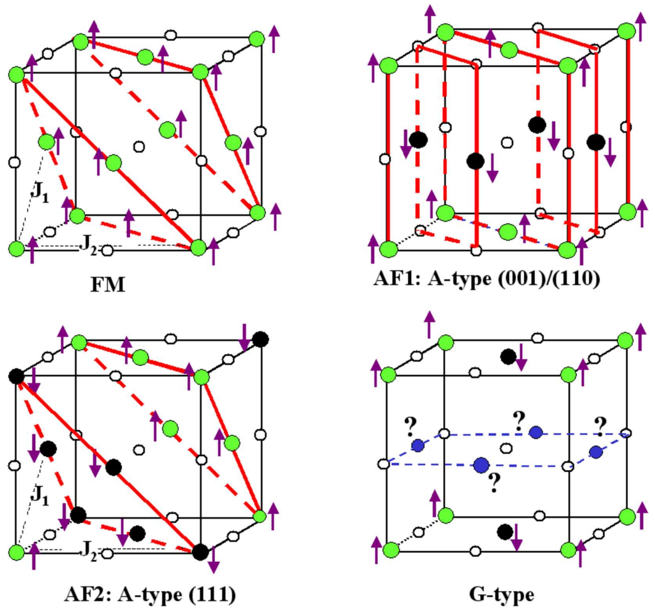

Figure 4.1: Magnetic phases used for the Heisenberg model fit: FM; AF$_2$ that is built of alternating (111) planes of like spins [highlighted by thick (red) lines]; AF$_1$, made of alternating (011) (or equivalently (001)) planes of like spins, delimited by (red) thick lines. The highly frustrated G-type AF phase is also shown for comparison. Filled light (green, up spin) and black (down spin) circles indicate TM atoms, small empty circles are for oxygens. For the G-type phase (blue) filled circles marked with a question mark indicate TM atoms with frustrated spin direction.

interesting to note that the G-type AF order (also depicted in Fig.4.1) is strongly disfavored by frustration, since in FCC symmetry there is no way to arrange the 12 NN interactions in antiparallel fashion without conflict.

To extract J$_1$ and J$_2$ we fit our calculated total energies to a standard 2-parameter classical Heisenberg Hamiltonian of the form:

$$H = -J_1 \sum_{\langle i,j \rangle} \vec{e_i} \cdot \vec{e_j} - J_2 \sum_{\langle\langle i,j \rangle\rangle} \vec{e_i} \cdot \vec{e_j} \tag{4.3}$$

where $\langle i,j \rangle$ and $\langle\langle i,j \rangle\rangle$ indicate summation over NN and NNN, respectively, and $\vec{e_i}$ is the spin direction unit vector. Energies (per f.u.) are then expressed as:

$$\begin{aligned} E_{FM} &= E_0 - 6J_1 - 3J_2 \\ E_{AF_1} &= E_0 + 2J_1 - 3J_2 \end{aligned}$$

$$E_{AF_2} \quad = \quad E_0 + 3J_2 \tag{4.4}$$

This is solved to give:

$$\begin{aligned} J_1 &= \frac{1}{8}(E_{AF_1} - E_{FM}) \\ J_2 &= \frac{1}{24}(4E_{AF_2} - 3E_{AF_1} - E_{FM}) \end{aligned} \tag{4.5}$$

With this choice of the Hamiltonian, negative and positive J values correspond to energy gain for spin-antiparallel and spin-parallel orientations, respectively.

Finally, we mention that several other anisotropic terms may in principle contribute to the Heisenberg Hamiltonian, related to short-range dipolar interactions favoring a preferential spin direction parallel to (111) planes, and to rhombohedral distortions of the AF_2 phase consisting on a (111) inter-planar contraction and slight change of the perfect 90° angle of the rock-salt cell, which causes a symmetry breaking of J_1 in two J_1^+ and J_1^- values [152]. However, all these effects are quantified to be order-of-magnitude smaller than the dominant exchange-interaction energies (e.g. for NiO J_1^+-$J_1^- \sim 0.03$ meV according to neutron data [174]), thus the Heisenberg Hamiltonian written in Eq.4.3 can be considered fully sufficient for our present purposes.

4.4 Results: MnO and NiO

4.4.1 Equilibrium structures

We have calculated total energies and pressures of MnO and NiO as a function of lattice parameter for the 3 magnetic phases FM, AF_2, and AF_1. Values of the equilibrium lattice parameter and bulk modulus for the stable AF_2 phase are reported in Tab.4.1, in comparison with the experimental values.

Results are quite satisfactory overall: each method predicts an equilibrium lattice constant in good agreement (within 1-2%) with experiment for the AF_2 phase. It is well known that structural properties calculated by LDA or GGA can be good, or even excellent, although the electronic properties are poor [180, 181]. The results for MnO and NiO are a case in point, as both LDA and PBE stay within 1% from experiment (the former in defect, the latter in excess). As for beyond-local functionals, HSE slightly underestimates PBE results and as a consequence is quite close to experiment, while

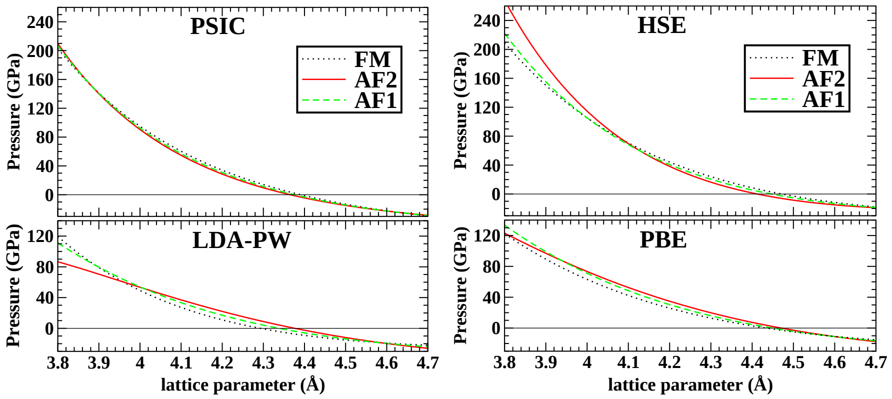

Figure 4.2: Calculated pressure for MnO in the three considered magnetic phases (see text). Each panel reports results obtained by a different energy functional.

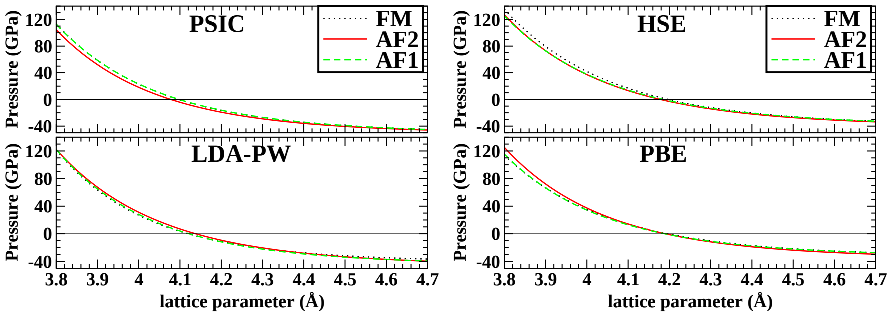

Figure 4.3: Calculated pressure for NiO in the three considered magnetic phases (see text). Each panel reports results obtained by a different energy functional.

VPSIC underestimate its respective local-functional (LDA-PW) references by ∼1% (a tendency also found [5] in other classes of oxides such as titanates and manganites).

In Figs.4.2 and 4.3 the calculated pressures for, respectively, MnO and NiO are reported as a function of lattice parameters for the three magnetic phases. The behavior in the region around the equilibrium lattice constant is expressed by the calculated bulk modulus (B_0) in Tab.4.1. The advanced functionals coherently give an increase of B_0 by ∼20-30 GPa (∼15%) with respect to their respective local functionals. This increase is a consequence of the enhanced 3d state localization and concomitant increase in Coulomb repulsion under compression which is expected from beyond-local approaches. Concerning the agreement with experiment, both PBE and HSE give values within the reported experimental uncertainty. In contrast, LDA-PW gives B_0 at the higher end of the experimental error bar, thus that the 15% further increase caused by VPSIC pushes the value of B_0 ∼40-50 GPa above the experiment. Hence the discrepancy should be seen as due to the LDA-PW performance (and to the characteristics of the used pseudopotentials), rather than as a failure of the VPSIC method in itself. The larger discrepancy, of course, is also related to the smaller volume.

A very interesting feature which emerges consistently from all the methods is the quite similar pressure dependence for different magnetic orderings, especially evident for NiO. This looks surprising at first glance, especially at strong compressive pressure, where changes in the magnetic ordering are related to metal-insulating transitions and to radical changes in the electronic properties. The explanation is that e_g electrons (strongly hybridized with O p states) govern the electronic and magnetic properties, but have only a minor effect on the response to applied hydrostatic pressure. In MnO, where t_{2g} states are also magnetically active, pressure is slightly more sensitive to the specific magnetic ordering (in Fig.4.2 AF_2 tends to differ from AF_1 and FM, which almost overlap each other). It should also be noted that in MnO for very contracted lattice constants the advanced functionals give pressures a factor of 1.5-2 larger than those of the corresponding local functionals, depending on the method and specific magnetic phase. At variance, for NiO advanced and local functionals give pressures in the same range. This reflects the larger effect of the advanced functionals on the half-filled t_{2g} shell of MnO, which is pushed down in energy and increase its spatial localization and its Coulomb repulsion under compression, than on the filled t_{2g} shell of NiO.

4.4.2 Magnetic properties upon applied pressure

4.4.2.1 Magnetic phase diagram under pressure

Figs.4.4 and 4.5 summarize our findings concerning phase stability and magnetic moments for MnO and NiO. Each panel reports results obtained by a given energy functional for relative magnetic energies (with respect to the most stable magnetic ordering) and their corresponding magnetic moments, as a function of lattice constant. Columnwise, panels are ordered according to the code used: LSDA and VPSIC (left, PWSIC); PBE and HSE (right, VASP).

We start our analysis from MnO results given by LDA and PBE (top panels of Fig.4.4). We can capture immediately the substantial similarity of the two approaches:

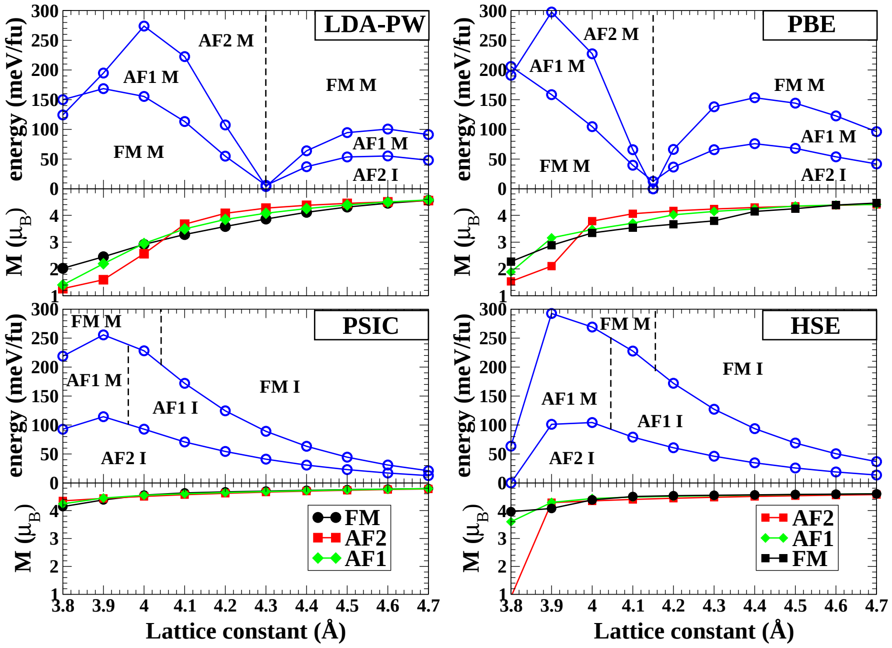

Figure 4.4: Total energies (relative to the ground state) and magnetic moments of FM, AF$_1$ and AF$_2$ phases of MnO as a function of lattice parameter, calculated by LDA and VPSIC (left panels), PBE and HSE (right panels). The insulating (I) or metallic (M) character of each magnetic phase is also indicated. Vertical dashed lines indicate phase transitions.

at large volumes AF$_2$ is the most stable phase and insulating, a metallic AF$_1$ region ~50-100 meV above AF$_2$, and a metallic FM region ~100-150 meV above AF$_2$. Under compression, all two methods reports a phase transition (indicated by the vertical dashed lines) through which the AF$_2$ phase yields to a metallic FM region as ground state, which wins over higher-energy AF$_1$ and (further above) AF$_2$ metallic phases. Looking at the corresponding magnetic moments, LDA and PBE both show a gradual moment decay when going from 4.7 Å up to a threshold of 4.0 Å (LDA) and 4.1 Å (PBE), corresponding, in the pressure scale, to ~40 GPa and 80 GPa, respectively. After this threshold, magnetic moments fall quite abruptly down to $\sim 2\ \mu_B$ at 3.8 Å for the stable FM metallic phase (notice that this unphysical collapse described by LDA-PW and PBE is not related to the true moment collapse [159] in MnO at much higher pressures).

Now we analyze the results obtained within beyond-local functionals. Overall, the picture is radically different: for the whole range of lattice parameters, the AF$_2$ insulating phase is robustly the ground state, and the spurious phase transition discussed above is absent. Furthermore, both approaches report a stability enhancement (i.e. a roughly linear energy gain) of AF$_2$ for decreasing lattice constant. This effect is indeed expected as a consequence of the increased Mn d-O p covalency and the related strengthening of AF superexchange coupling. The AF$_2$ maximum stability is reached at ~3.9 Å according to VPSIC (corresponding to an applied compression of ~130 GPa), and at ~4.0 Å according to HSE (P~90 GPa). The peak of AF$_2$ energy gain with respect to the equilibrium structure is nearly 100%, from ~50 meV/f.u. to more than 100 meV/f.u. according to HSE and VPSIC. Above AF$_2$ both advanced functionals favor the AF$_1$ phase, which, (at variance with the always insulating AF$_2$ phase) undergoes a metal-insulating transition at 3.97 Å (VPSIC) and 4.05 Å (HSE). Above AF$_1$ resides a FM region, again separated in a large-volume insulating and small-volume metallic sides, with an insulating-metal transition threshold of 4.07 Å for VPSIC, and 4.15 Å for HSE. This consistency is also reflected in similar values of magnetic moments through the whole lattice constant range: both methods describe a moderate decline from ~4.7 μ_B at 4.7 Å to ~4.0-4.2 μ_B (depending on the specific magnetic phase) at a=3.8 Å. Interestingly, the coherent picture delivered by the advanced functionals for MnO is not limited to the predict the same ground-state, but also involves ordering and energy differences among the three magnetic phases. This is instrumental to coherently describe finite-temperature properties as well, as shown in Section 4.4.2.3.

Now we move to the analysis of NiO results, summarized in Fig.4.5, starting again from the phase stability diagram drawn by the two local functionals (upper panels). At variance with MnO, now all the methods give the insulating AF$_2$ phase as stable at any lattice constant; however the competition with the other two orderings is described differently: according to LDA, moving from large to small lattice constants there is first a tiny region where the AF$_2$ stability increases, reaches maximum at 4.4 Å (thus much above the equilibrium value) and then falls linearly all the way down to 3.8 Å . Furthermore, above AF$_2$ the LDA predicts a coexistence of degenerate AF$_1$ and FM metallic phases. This scenario can be rationalized looking at the magnetic moments for AF$_1$ and FM calculated in LDA: starting from the large lattice constant value of ~1 μ_B, the magnetic moment falls rapidly and vanishes altogether just at 4.4 Å (i.e. still above

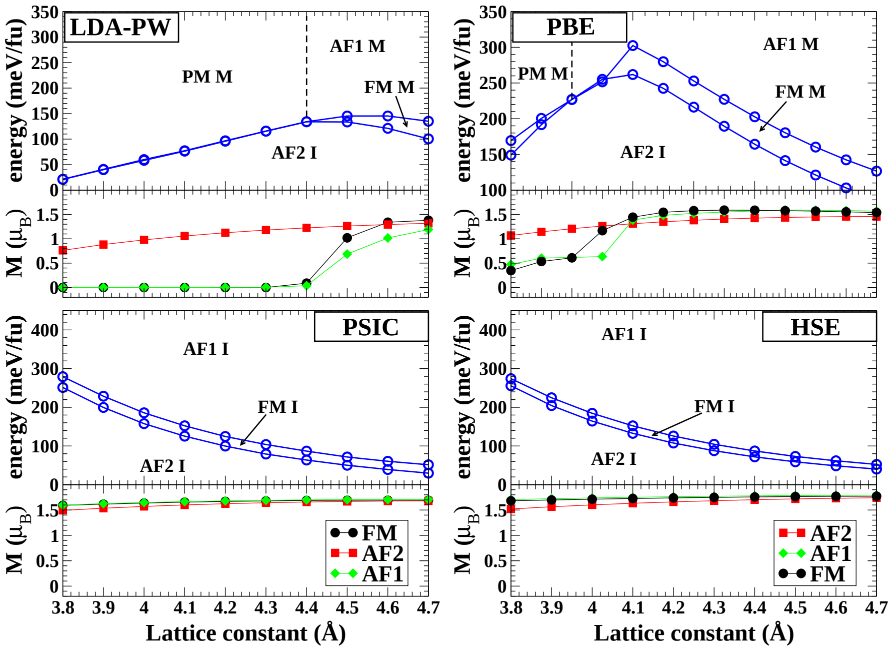

Figure 4.5: Total energies (relative to the ground state) and magnetic moments of FM, AF_1 and AF_2 phases of NiO as a function of lattice parameter, as calculated for the different methods used in this work: LDA and VPSIC calculations (left), PBE and HSE calculations (right). PM indicates Pauli Paramagnetic ordering, I and M insulating and metallic character, respectively. Vertical dashed lines indicate phase transitions.

the equilibrium value of 4.35 Å). Below this threshold the LDA describes a metallic Pauli paramagnetic region. On the other hand, the expected Mott-insulating behavior is only maintained in the AF_2 phase. This feature represents a major shortcoming which seriously hamper the NiO description by LDA.

PBE shows a similar, although slightly less dramatic failure, since the moment collapse starts to show up for smaller lattice constant values (4.0 Å for FM and 4.1 Å for AF_1, thus definitely below the equilibrium 4.19 Å), and the magnetic moment is severely reduced to about 0.5 μ_B, without vanishing completely.

Both the beyond-LDA functionals, predict a large enhancement of AF_2 stability upon lattice constant decrease in a wide range around the equilibrium value. The artificial moment collapse described by the local functionals is absent, and all the magnetic phases remain insulating through the whole lattice constant range. All methods find magnetic moments of about 1.7-1.8 μ_B at large lattice constants, and a very moderate decrease to ∼1.5 μ_B at the smallest lattice constant considered (3.8 Å). Particularly striking is the agreement between HSE and VPSIC, both describing a tiny FM region intermediate between AF$_2$ and AF$_1$, and a parabolic rise of the AF$_2$ energy gain from ∼50 meV at 4.7 Å up to ∼250 meV at 3.8 Å.

In order to clarify the difference in the magnetic moments under pressure obtained by the different methods, we examine the orbital-resolved density of states (DOS) for NiO at two representative lattice constants, a=4.5 Å and a=4.0 Å , corresponding to situations of tensile and compressive strain. The results are shown in Fig. 4.6.

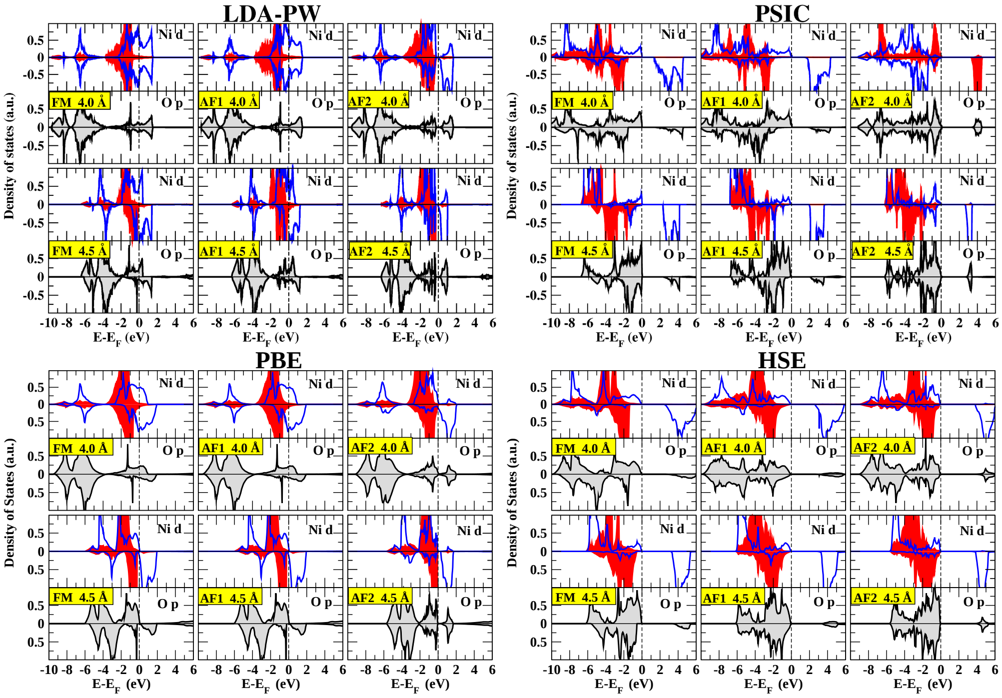

Figure 4.6: Orbital-resolved DOS for NiO calculated at two lattice constant values (4.0 Å, and 4.5 Å) with all our employed functionals: VPSIC (top right), PBE (bottom left) and HSE (bottom right). Only the DOS for the relevant orbitals are shown: O p (filled gray curves) and Ni d, separated in t$_{2g}$ (filled red curves) and e$_g$ (solid blue lines) contributions. Positive and negative curves represent majority and minority contributions.

LDA FM and AF$_1$ phases are actually Pauli-paramagnetic, with perfectly compensated spin-densities, while in the AF$_2$ phase a barely visible gap opens up within the e_g manifold. In PBE for FM and AF$_1$ phases some magnetization shows up in the upper e_g manifold, while for AF$_2$ the magnetic moment is formed, and a Mott gap is about to open. Even at a=4.5 Å some differences among the local functionals are detectable: according to LDA only the AF_2 is insulating, while PBE provides well formed magnetic moments in each phase but only AF_2 is clearly insulating.

Using beyond-local functionals, the expected picture of wide-gap intermediate charge-transfer/Mott insulator described by the experiments [182, 183, 184] is restored. Now the DOS is that of a robust insulator under both lattice expansion and compression, with a valence band top populated by a mixture of O p and Ni d states, and the conduction bottom with a majority of e_g and a minor fraction of O p states. The energy gap for the AF_2 phase (∼3.5 eV for both VPSIC and HSE) is in good agreement with the experimental value, and even FM and AF_1 phases show sizeable gaps of about 1-2 eV.

In summary, for MnO and NiO VPSIC and HSE deliver a very coherent description of relative phase stabilities in the whole examined range of lattice parameters, and predict a clear enhancement of the AF_2 phase relative stability (not described by local functionals) within a wide lattice parameter interval, which suggests the possibility of an enhancement of the magnetic ordering Néel temperature (T_N) upon applying compressive stress. Before exploring the validity of this expectation we will first discuss the evolution of the magnetic coupling constants upon compression.

4.4.2.2 Exchange interactions under pressure

A few qualitative considerations on magnetic interactions can help to correctly interpret our results. Our calculations find the T=0 magnetic ground state to be the observed AF_2 for both MnO and NiO; however, the detailed magnetic interactions suggest two different scenarios. Magnetic coupling between Mn^{2+} $3d^5$ ions is mediated by half-filled orbitals (thus J_1 mainly by t_{2g}-t_{2g} and J_2 by e_g-e_g couplings), which are both robustly AF oriented according to superexchange theory [107, 185, 186]. Thus we expect J_1 and J_2 to be both sizable and negative (i.e. AF in our present convention). For Ni^{2+} d^8 ions, on the other hand, only e_g-e_g coupling is magnetically active. Hence we expect a large and negative J_2 due to the dominance of covalent superexchange, very small and positive J_1 due to superexchange-mediated 90°-oriented e_g-(O p_x,p_y)-e_g orbital coupling, and therefore huge J_2/J_1 values.

These expectations are largely confirmed by our results: in MnO (Fig.4.7) J_1 and J_2 roughly track each other as function of the lattice parameter irrespective of the calculation method. However, it is of the utmost importance to observe the dramatic difference between the description of local and advanced functionals: looking at LDA results (Fig.4.7) J_1 and J_2 are moderately negative at expanded lattice, then upon lattice shrinking they both change sign and grow up to a maximum value at $\sim$ 4 Å, and finally fall back down as the lattice shrinks further. The VPSIC almost completely reverses this behavior: J_1 and J_2 nearly vanish at 4.7 Å (signaling a shorter interaction range with respect to LDA), and then grow steadily (in absolute value) on the negative side as the lattice squeezes up. Curiously, LDA and VPSIC curves intersect each other at $\sim$ 4.4 Å, but this agreement near the equilibrium lattice is just a fortuitous crossing of two otherwise radically different behaviours. Notice finally that while in VPSIC $J_2/J_1>1$ at any lattice parameter, in LDA-PW the exchange interaction ratio fluctuates as function of the lattice constant.

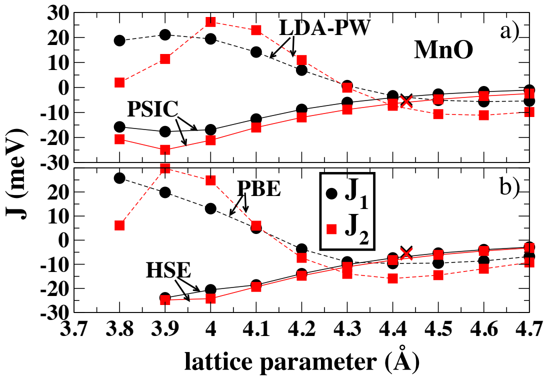

Figure 4.7: Exchange-interaction parameters J_1 (black filled circles) and J_2 (red filled squares) as a function of lattice parameter calculated for MnO with various approaches. a) with PWSIC code by LDA-PW and VPSIC functionals; b) with VASP code using PBE and HSE functionals. Dashed lines refer to local density functional (LDA-PW and PBE) calculations, solid lines represent beyond-local density functionals calculations (VPSIC and HSE). Black and red crosses show experimental values for J_1 and J_2, respectively, reported for MnO in Tab.4.2.

The considerations exposed for LDA and VPSIC can be identically repeated for PBE and HSE, respectively (the similarity of curves is apparent comparing panel a) and b) see Fig.4.7).

Now we move to examine NiO (Fig.4.8). As expected, the relative weight of J_1 and J_2 is very different: all functionals (both local and beyond-local) find J_1 very small and positive at any lattice value (black symbols). On the other hand, the large and negative

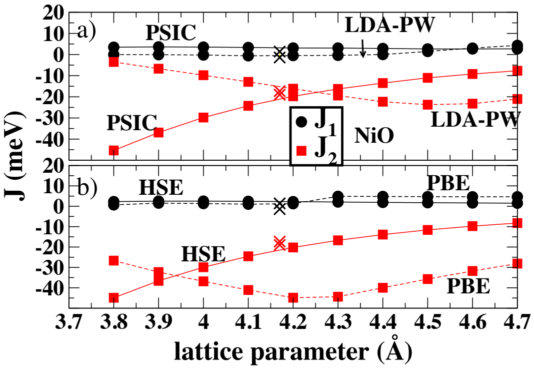

Figure 4.8: Exchange-interaction parameters J_1 (black filled circles) and J_2 (red filled squares) as a function of lattice parameter calculated for NiO with various approaches. From top to bottom: a) with PWSIC code by LDA-PW and VPSIC functionals; b) with VASP code using PBE and HSE functionals. Dashed lines refer to local density functionals calculations (LDA-PW and PBE), whereas solid lines represents beyond-local density functionals calculations (VPSIC and HSE). Black and red crosses show experimental values for J_1 and J_2, respectively, reported for NiO in Tab.4.2.

J_2 is again differently described by the two sets of functionals. We can repeat most of the considerations made for J_2 in MnO (Fig.4.8), the behavior with lattice parameter being roughly inverted.Phenomenologically, it is important to note the appreciable growth of the exchange interactions for large applied compression, coherently described by beyond-local functionals. In the next section we will illustrate the reverberations of this behavior on the magnetic ordering temperature. For now, we remark that this is the expected behavior of the so called covalent exchange, i.e. the shorter the TM-O distance, the stronger the energetic advantage for the O 2*p* ligand states to overlap with the adjacent TM 3*d* states with unlike spins. This advantage reaches a maximum at a certain compression, after which the J's start falling. This is the point when the pressure is so strong that minority DOS begins to be appreciably populated and in turn magnetic moments start falling.

Overall, the two beyond-local functionals furnish a qualitatively and quantitatively coherent description of exchange interactions under pressure for MnO and NiO. There is a large body of data in literature, both theoretical and experimental, with which to compare our data, at least at equilibrium. In Tab.4.2 we report our values for the theoretical equilibrium structure in comparison with the experimental values and other theoretical predictions obtained by several density functional based approaches (see

Sec.4.1), we neglect tight-binding or shell-model results, which rely on experimental fitting).

The J's reported in the Table are determined by finite energy differences, though in some cases, the magnetic force theorem (MFT) [191] based on the exchange-correlation density-functional gauge invariance under infinitesimal spin rotations [135, 192, 193, 194] was used. In Ref. [137], exchange interactions and the whole spin-wave spectrum was determined from the poles of spin susceptibility [195, 196]. As for experiments, results from both inelastic neutron scattering (INS) [174, 187, 188] and thermodynamic data (TD) [189, 190] are reported.

Comparison of J values given by different approaches and considerations on the level of agreement with the available experimental data must be taken very carefully. Differences of the order of a few meV may derive from technical implementation aspects rather than from the underlying theory. In MnO the comparison is further complicated by the closely similar J values. It is expected that local functionals should overestimate the J's, due to the underestimation of intra-atomic exchange splitting and the related overestimation of *p*-*d* hybridization. This is indeed verified with PBE; however LDA (the least accurate of the two local functionals) delivers J's in excellent agreement with the experiment: this fortuitous agreement was previously explained as consequence of the unphysical AF_2 to FM transition occurring in LDA-PW near the equilibrium structure. On the other hand, beyond-local functionals perform quite satisfactorily, apparently ranking among the closest to experiment both in absolute terms and concerning the J_2/J_1 ratio (1.16 for INS data, 1.1 for HSE, 1.5 for VPSIC). For NiO the analysis is simpler, as J_1 is very small and a qualitative comparison can be done on the base of J_2 only. As already commented, the LDA is grossly inadequate and can be left aside. On the other hand PBE delivers sizably overestimated J_2. As for beyond-local functionals, we have previously seen that that J's calculated by VPSIC and HSE almost overlap each other throughout the lattice parameter range. The agreement with values drawn from neutron experiments [174] is indeed quite satisfying. Nevertheless, the slight VPSIC underestimation of the equilibrium lattice parameter (4.09 Å against the near experimental-matched 4.18 Å of HSE) reverberates in a ∼15% overestimation of J_2. Looking at previous literature, we found a substantial agreement of VPSIC and HSE with GGA+U calculations of Ref. [142] (here the J's are also calculated as a function of lattice parameter) and with other types of hybrid functionals[153] as well. On the other hand, both unrestricted HF [153], full SIC in LMTO approach (SIC-LMTO) [146] and the local SIC (LSIC) (a KKR-based implementation of the self-interaction correction method [147, 148, 149]) tend to an excessive electronic localization, which thus turns into a slight underestimation of the exchange interactions.

	LDA-PW	VPSIC	PBE	HSE	Expt.
			MnO		
a_0	4.38	4.35	4.47	4.41	4.43^a
B_0	158	194	145	170	151^b,162^c
			NiO		
a_0	4.15	4.09	4.19	4.18	4.17^d
B_0	234	269	183	202	180-220^e

a): Ref.[175]; b): Ref.[176], c): Ref.[177]
d): Ref.[178]; e): Ref.[179]

Table 4.1: Equilibrium lattice constants a_0 (in Å) and bulk moduli B_0 (in GPa) calculated in this work with various methods, compared with experimental values. All values refer to the stable AF_2 magnetic ordering.

	MnO			NiO	
	J_1	J_2		J_1	J_2
Experiment					
INS[a]	-4.8	-5.6	INS[b]	1.4	-19.0
TD[c]	-5.4	-5.9	TD[d]	-1.4	-17.3
This work: local functionals					
LDA-PW	-2.7	-6.3	LDA-PW	-0.5	-14.7
PBE	-9.5	-14.9	PBE	1.2	-44.5
This work: advanced functionals					
VPSIC	-5.0	-7.6	VPSIC	3.3	-24.7
HSE	-7.0	-7.8	HSE	2.3	-21.0
Previous calculations					
LSDA[e] (MFT)	-13.2	-23.5			
LDA+U[e] (MFT)	-5.0	-13.2	GGA+U[l]	1.7	-19.1
OEP[e] (MFT)	-5.7	-11.0	SIC-LMTO[m]	1.8	-11.0
PBE+U[f]	-4.4	-2.3	Fock-35[n]	1.9	-18.7
PBE0[f]	-6.2	-7.4	B3LYP[n]	2.4	-26.7
HF[f]	-1.5	-2.32	UHF[n]	0.8	-4.6
QPGW[g]	-2.8	-4.7	QPGW[g]	-0.8	-14.7
LSIC[h]	1.4	-3.3	LSIC[h]	2.8	-13.9
LSIC[h] (MFT)	-1.8	-4.0	LSIC[h] (MFT)	0.3	-13.8
B3LYP[i]	-5.3	-11.0			

a): Ref.[187, 188], b): Ref.[174], c): Ref.[189] d): Ref.[190]
e): Ref.[135], f): Ref.[152], g): Ref.[137], h): Ref.[147]
i): Ref.[154, 155], l): Ref.[142], m): Ref.[146], h): Ref.[153]

Table 4.2: Exchange interaction parameters for MnO and NiO (in meV) calculated in this work, compared to experimental and theoretical values from previous works.

4.4.2.3 Critical transition temperatures under pressure

Fig.4.9 reports critical temperatures for MnO and NiO calculated with the Heisenberg Hamiltonian given in Eq.4.3 and solved through classical MonteCarlo (MC) simulated annealing technique [197]. Values calculated at equilibrium and at experimental volume are reported in Tab.4.3, in comparison with the experiment and other theoretical predictions.

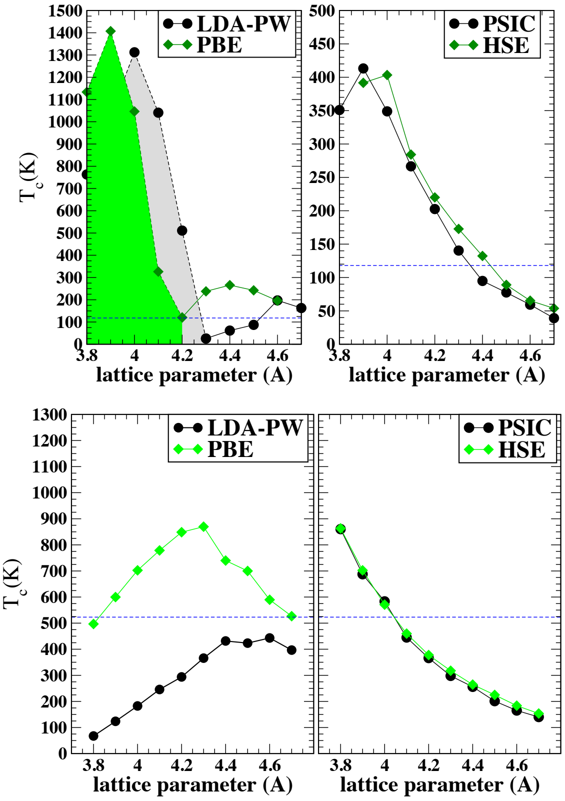

Figure 4.9: Critical temperatures as a function of lattice constant for MnO (top panel) and NiO (bottom) calculated by simulated-annealing MonteCarlo simulation of the Heisenberg Hamiltonian in Eq.4.3. Left and right panels separate local and advanced functionals used to determine each set of (J_1, J_2). The shaded areas in the top-left panel indicate FM metallic regions; apart from that, each curve separates low-T insulating AF_2 from high-T insulating PM regions (PM stands for Pauli Paramagnetic ordering). The dashed horizontal lines indicate experimental T_N values.

We start discussing the case of MnO as described by our local density functionals. As expected, MC calculations describe fictitious phase transitions (consequence of the spurious magnetic moment collapse previously discussed) from AF_2 to FM metallic magnetic phase (highlighted by the dashed areas) while moving from large to small lattice parameters. The onset of this transition depends on the method: it is especially harmful in LDA as it occurs near (just below) the theoretical lattice value (4.35 Å). In all cases this phase transition dramatically alters the critical temperature behavior, which is expected to grow (at least in some interval around equilibrium) as the lattice parameter contracts.

Furthermore in all cases the predicted T_N (see Tab.4.3) remains quite distant from the experimental T_N=118 K (horizontal dashed line in the Figure). Notice again that while PBE overestimates T_N at the equilibrium structure, the spurious phase transition in LDA-PW cause T_N to be smaller than the experimental values, and paradoxically not too far (at experimental lattice constant) from the experiment. This is another manifestation of the fortuitous agreement already pointed out in the illustration of the exchange interactions.

Conversely, the advanced functionals deliver for MnO a nicely consistent picture, with T_N growing steadily from very large lattice constants ($T_N \rightarrow 0$) up to 3.9-4.0 Å, and peaking at ∼410 K. The corresponding pressure is around 120±20 GPa depending on the approach (see Fig.4.2). There is a minor offset between the two methods, due to the slight increase in J's moving from VPSIC to HSE. However, if calculated at their respective equilibrium values, both VPSIC and HSE predict a T_N which is almost spot-on to the experimental value. In addition, HSE and VPSIC-derived dT_N/dP∼6k/GPa also agree well with experiment.

Moving to the analysis of NiO, the two local functionals behave quite differently from each other. So, it is all the more remarkable that their beyond-local counterparts are capable to rebuild a very consistent picture, with T_N linearly growing along with the decrease of lattice parameter. The near-overlap of HSE and VPSIC is especially striking, and already noticed for the J's. Notice that for NiO there is no lattice parameter turning point in the considered range, thus T_N keeps growing up to 3.8 Å, corresponding to a pressure of about 100-120 GPa (see Fig.4.3). The agreement with the experiment for NiO is much less outstanding than for MnO, as both HSE and VPSIC remains below the experimental T_N=523 K by ∼20% (at the equilibrium structure the VPSIC value is actually not too far from the experiment thanks to its underestimated lattice parameter).

	MnO	NiO
	Experiment	
ND^{a,b}	118	523
Expt. J's	85^{c}	340^{d}
Expt. J's	90^{e}	300^{f}
	This work: local functionals	
LDA-PW	55 (71)	272 (280)
PBE	249 (257)	824 (829)
	This work: advanced functionals	
VPSIC	116 (89)	458 (387)
HSE	125 (116)	393 (400)
	Previous works	
LSIC^{g} (DLM)	126	336
LSIC^{g} (RPA)	87	448
LSIC^{g} (MC)	90	458
LDA^{h} (MC)	423	965
LDA+U^{h}(MC)	240	603
CED^{h} (MC)	172	519

a): Ref.[198], b): Ref.[199], c) Ref.[187, 188], d) Ref.[174], e) Ref.[189]. f) Ref.[190], g) Ref.[147], h) Ref.[136].

Table 4.3: Critical temperatures (K) for MnO and NiO calculated in this work at equilibrium and experimental (in brackets) lattice constant, compared with experimental (neutron diffraction, ND) and theoretical values from previous works. As a reference we also report MC-calculated values obtained by using the experimental J's (see text for discussion).

The disagreement between *ab initio* theoretical estimates and the experimental value of T_N for NiO is typical and well documented in the literature (see e.g. Ref. [147] and references therein) and a full discussion on the subject is beyond our present scope. We only remark that the mismatch with HSE and VPSIC is somewhat puzzling, in consideration of the excellent agreement of the calculated J_2 with the experimental value. In fact, even using experimental sets of J's, the MC-calculated T_N would change only marginally our theoretical value: as a useful reference we also report in the Table the T_N of MnO and NiO calculated by MC using sets of experimental J's reported in Tab.4.2. It turns out that these T_N underestimate by ∼30% the directly measured T_N (they are even lower than those obtained with our calculated J's, since the slight overestimation of our calculated J's helps in shifting up the predicted T_N). The discrepancy between experimental J's and T_N somewhat points out to possible inadequacies of the employed Heisenberg model, possibly due to further terms (not included in Eq.4.3) which might be important at the relatively high ordering temperature of NiO. In Tab.4.3 we compare our results with some previous theoretical predictions (we omit the many mean-field approximations which are known [107] to grossly overestimate the critical temperature). Ref.[147] proposes T_N obtained by disordered local moments (DLM), random-phase approximations (RPA) and MC, based on the MFT-calculated J's given in Tab.4.2. The DLM values are closest to our HSE and VPSIC estimate, while RPA and MC values for NiO are larger than our values despite smaller J's, due to the debatable inclusion in Ref.[147] of the quantum rescaling factor (S+1)/S [136]. Ref. [136] also proposes MFT-calculated J's, derived from LDA, LDA+U, and LDA plus dynamical mean field approach solved through cluster exact diagonalization (CED). The latter seems to restore an outstanding agreement with the experimental T_N for NiO [200].

4.5 Summary and Conclusions

It is fair to affirm that the overall account of the structural, electronic, and magnetic properties of MnO and NiO provided by the advanced functionals is overall quite satisfying, internally consistent, and in good agreement with experiments. In particular, HSE shows a remarkable quantitative agreement with experiments on most examined properties; the VPSIC, perhaps surprisingly when considering the substantially different conception at the basis of their theoretical constructions, is quite comparable with HSE results, and in some cases in spectacular quantitative agreement (e.g. the NiO exchange interactions vs. lattice constant). An important persistent shortcoming of VPSIC, however, is the prediction of structure: the predicted lattice constant is below experiment by ∼1-2%. This tendency to deliver smaller-than-optimal structural parameters was also encountered in other situations [5], and it is probably not an isolated occurrence, but rather a characteristics of the VPSIC method. In perspective, we expect that this drawback could be overcome by adopting the GGA (e.g. PBE) instead of the LDA as reference functional upon which to build the VPSIC projector. This would probably lead, as in the case of HSE, to a moderate volume reduction compared to the slightly overestimated GGA volume, hence probably to an end product much nearer to experiments.

Finally, our evaluation of the exchange-interaction parameters and of the Néel temperatures requires a mention. While the calculated J's of both MnO and NiO are found in satisfying agreement with the experiments, only for the first an equally satisfying T_N is predicted by the MC-solved Heisenberg Hamiltonian. This discrepancy can stimulate debate and more work devoted to investigate the possible inadequacies of the Heisenberg Hamiltonian at high temperature, an aspect that has not been sufficiently stressed in previous literature.

In conclusion, we have presented a systematic analysis of the structural and magnetic properties of MnO and NiO under applied pressure, including ground-state and finite temperature properties, by using a range of standard and advanced first-principle approaches. The advanced techniques (HSE, VPSIC) describe very consistently the behavior of the exchange interactions in a wide range of lattice constant values around the equilibrium structure, showing an overall agreement with experiments. This places such methods among the most accurate now available to the first-principles community.

Our results establish a benchmark of accuracy for innovative techniques aimed at the determination of the magnetic properties of magnetic oxides.

5

Nickelates

5.1 Charge disproportionation from first principle: La_2NiMnO_6

We have a forthcoming paper: "Charge disproportionation from first principle: the case of the double perovskite La_2NiMnO_6". This is essentially my own work. The planning and assessment of the work was done in collaboration with the supervisors.

5.1.1 Introduction

Charge disproportionation, also known as charge ordering, is expected in materials containing a mix of cations of nominally different valence. These may be a single species on inequivalent sites/environments, or two or more different species. Examples are magnetite and doped manganites. It is a source of puzzlement that disproportionation as calculated *ab initio* is generally quite modest compared to the nominal value - but then of course quantifying charge transfer is tricky. As a case study we will consider the double perovskite La_2NiMnO_6 (LNMO).

LNMO is a ferromagnetic (FM) semiconductor and a most promising material for spintronics. LNMO is a double ordered perovskite ($A_2BB'O_6$) with NiO_6 and MnO_6 octahedra. It is monoclinic ($P2_1/n$) at low temperature and transforms to rhombohedral ($R\bar{3}$) at high temperature (in this context we will focus only on this), with these two structure coexisting over a wide temperature range [201, 202]. Its paramagnetic-FM transition temperature (T_c) is about 280 K.

The magnetic properties of LNMO can be well explained by Goodenough-Kanamory rules [203, 204, 205]. However disagreements exist about the cation oxidation state (i.e. Ni^{2+}/Mn^{4+} or Ni^{3+}/Mn^{3+}). Nuclear magnetic resonance spectroscopy (NMR) and x-ray absorption spectroscopy have provided evidence for ordered Mn^{4+}-O-Ni^{2+} superexchange interactions in LNMO [206, 207]. On the other hand some neutron diffraction measures conclude that Ni^{3+} and Mn^{3+} are present [201, 202]. It is known that disproportionation calculated from first-principles is quite modest compared to the nominal valence. The idea here is to analyze the charge imbalance between Ni and Mn via partial DOS integration (integrals of atom-centered-sphere-projected densities of states), Bader analysis [208, 209, 210, 211] and by the occupancy of localized Wannier functions [212].

The Section is organized as follow: in Sec.5.1.2 we show the structure and electronic properties of LNMO, in Sec.5.1.3, Sec.5.1.4, and Sec.5.1.5 we discuss and show the results of our analysis.

5.1.2 Structure and electronic properties

Using GGA [213] we have performed structural optimization of the internal degrees of freedom of the rhombohedral (RH) structure, keeping the lattice parameters fixed at experimental values [201]. Our structural parameters (Table 5.1) for the RH FM state are in good agreement whit another theoretical study [214] as well as with experimental data [201]. In our final structure (Fig.5.1) we observe that NiO_6 is tilted with respect to MnO_6 giving rise to a Ni–O–Mn bond angle of 157°.

a(Å)	b(Å)	c(Å)		x	y	z
5.474	5.474	5.474	La	0.24994	0. 24993	0.24994
α	β	γ	Ni	0.0	0.0	0.0
60.671	60.671	60.671	Mn	0.5	0.5	0.5
			O	0.80678	0.68043	0.25839

Table 5.1: GGA structural parameters of La_2NiMnO_6 in RH phase

In Fig.5.2 we show the band structure and the spin, site, and orbital-resolved density of states (DOS) of FM RH LNMO. We obtain an insulating solution with a band gap of ∼0.5 eV. In the DOS (Fig.5.2(b)) we see that below -2 eV the main contribution is from O-p states. The crystal field splits the Mn- and Ni-d manifolds into t_{2g} and e_g levels. In the up-spin channel the Mn-t_{2g} bands are located between Ni-e_g and Ni-t_{2g}

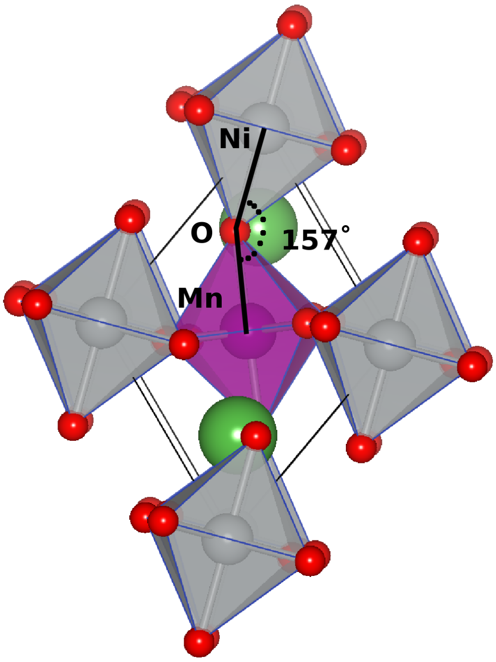

Figure 5.1: Structure of RH FM La$_2$NiMnO$_6$. In the picture we can observe that the Ni(grey)–O(red)–Mn(violet) bond angle is 157°.

bands and are filled, while the Mn-e_g bands are separated by a gap of ∼2.5 eV from the Mn-t_{2g} bands and are empty. In the down-spin channel, both Mn-e_g and Mn-t_{2g} bands are empty and located ∼1.5 to 5 eV above the top of valence band (TVB). In other words the nominal valence of Mn is 4+ ($d^3 : t_{2g}^3\, e_g^0$) in agreement with the Mn NMR and x-ray absorption spectroscopy measurements [206, 207]. In the up-spin channel, the Ni-t_{2g} and Ni-e_g levels are placed in an energy range of ∼2 eV from the TVB and show a significant hybridization with Mn-d states and O-p states. In the down-spin channel the Ni-t_{2g} bands are found between O-p states and the TVB, while Ni-e_g states lie ∼1.0 eV above the TVB. This leads to conclusion that the oxidation state of Ni is nominally 2+ ($d^8 : t_{2g}^6\, e_g^2$).

In our calculations the magnetic moment of Mn is 2.94μ_B which agrees with the experimental value of 3.0μ_B [215]. However, the magnetic moment of Ni is 1.28μ_B) which is less than the experimental value of 1.9μ_B [215]. The residual moment reside on the O sites giving rise to the total magnetization of ∼5.0μ_B in agreement with experiment [215].

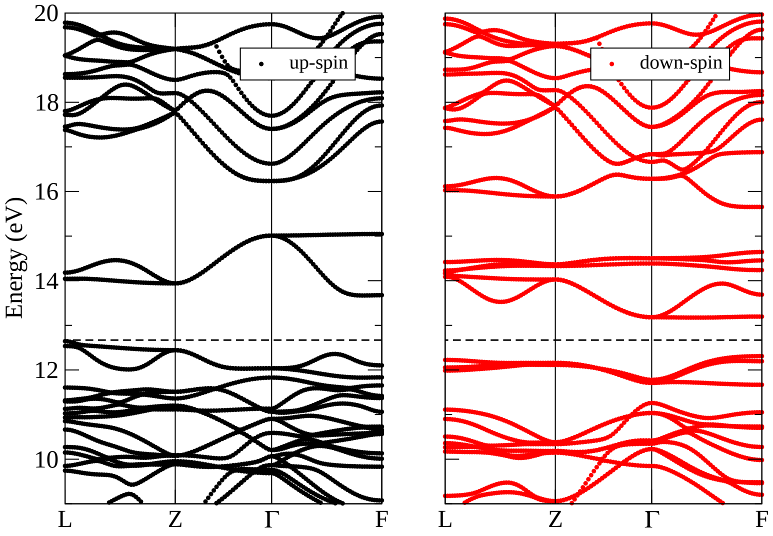

(a) Electronic band structure of FM RH La$_2$NiMnO$_6$ along selected symmetry directions: L (0, $\pi/2$, 0), Z ($\pi/2$, $\pi/2$, $\pi/2$), Γ (0, 0, 0), F ($\pi/2$, $\pi/2$, 0).

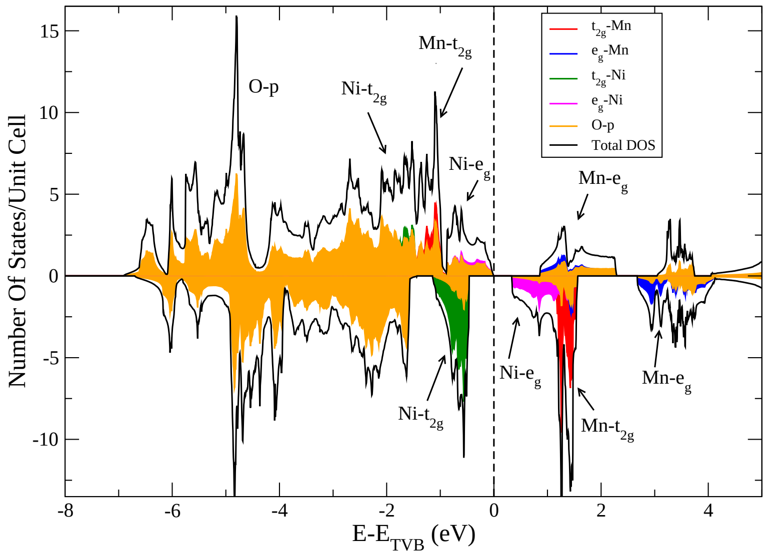

(b) Density of states of FM RH La$_2$NiMnO$_6$.

Figure 5.2: Electronic properties of FM RH La$_2$NiMnO$_6$

5.1.3 Integrating atom-projected DOS

To interpret the electronic structure of a material, it is often useful to understand which state with what occupation can be associated with a specific atom. One standard way to do this is to use the projected density of states (PDOS), defined as the number of electronic states at a specified energy weighted by the fraction of the total electron density for those states that appears in a specified volume around the nuclei. Typically, this volume is simply taken to be spherical; so to calculate the PDOS we must specify the effective radii of each atom of interest. The results of this approach for LNMO are shown in Fig.5.3. We plot the oxidation state of the atoms versus the ratio R_{sph}/R_{ion} where R_{sph} is the radius of the sphere centered on the atom and R_{ion} is the ionic radius of this one. Unfortunately the definition of the radius is not unambiguous. If too small a radius is used, information on electronic states that are genuinely associated with the atom will be missed. If the radius is too large, on the other hand, the LDOS will include contributions from other atoms. Of course this affects the calculated charge. A

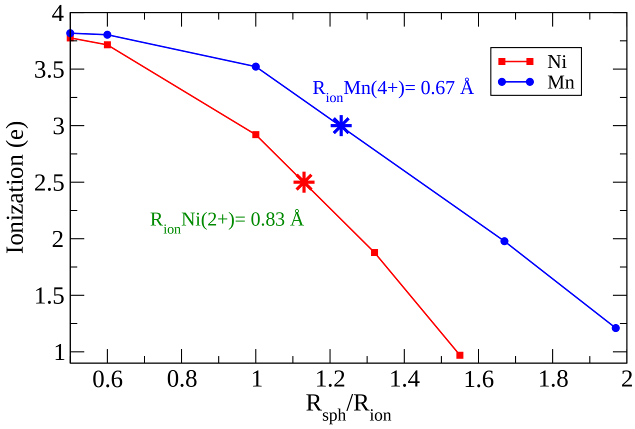

Figure 5.3: Integrated atom-projected DOS for La_2NiMnO_6 in the RH phase. The stars indicate one-half of the bond length Mn-O and Ni-O

good criterion to choose the radii of the spheres could be to take one-half of the bond length Mn-O for the sphere centered on Mn and the half of the bond length Ni-O for the one centered on Ni (see stars in Fig.5.3). In this case our results suggest that the oxidation state for Ni and Mn is +2.5 and +3.0 respectively, with a disproportion of 0.5 electrons. Only at unreasonably small radii the Mn attains its nominal 4+ state.

5.1.4 Bader analysis

The Bader approach [208, 209, 210, 211] eliminates the space-partitioning ambiguity of the method just described (Sec.5.1.3): space is divided into regions by surfaces where the gradient of the electron density has no surface-normal component $\overline{S} \cdot \overline{\nabla} \rho = 0$, whith $\overline{S}$ a surface normal vector. We will refer to regions bounded by such dividing surfaces as Bader regions (Fig.5.4).

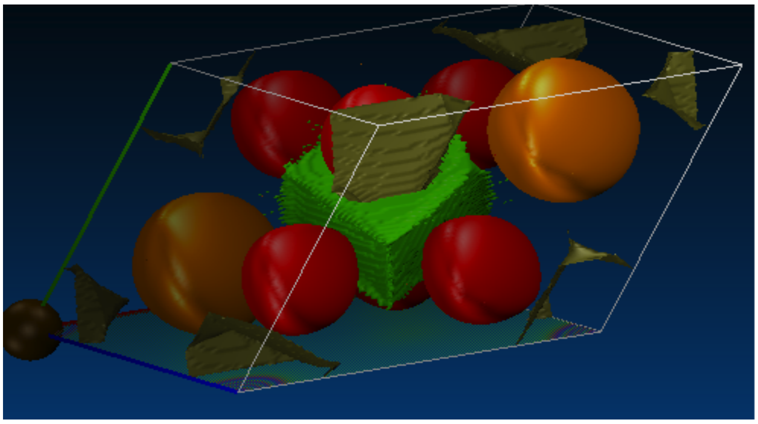

Figure 5.4: The Bader partition generates volumes that are not spherical. An example is the green cube in the picture, which belongs to Mn (the others are not Bader volumes).

Because this analysis is based solely on the charge density, it is rather insensitive to the basis set used in the calculation and can be used to analyze plane wave based calculations as well as atomic-basis ones. Each Bader region generally contains one nucleus, but not necessarily. Sometimes no nucleus is found within a Bader region. By integrating the electronic density within the Bader region where an atom is located, and possibly adding the electronic charge in nearby regions that do not include a nucleus, the total charge on an atom can be estimated.

ion	oxidation state
Ni	+1.19
Mn	+1.66

Table 5.2: Bader analysis for La_2NiMnO_6 in RH phase

In tab.5.2 we show the results of Bader analysis. The oxidation state for Ni and Mn is +1.19 and +1.66 respectively with a weak disproportion of ~ 0.5 electrons.

5.1.5 Wannier approach

Wannier functions (WFs) $|W_n^{\mathbf{T}}\rangle$ are defined as Fourier transforms of Bloch functions $|\Psi_{n\mathbf{k}}\rangle$ [216]:

$$|W_n^{\mathbf{T}}\rangle = \frac{1}{\sqrt{\Omega}} \sum_{\mathbf{k}} e^{-i\mathbf{k}\mathbf{T}} |\Psi_{n\mathbf{k}}\rangle, \tag{5.1}$$

where $\mathbf{T}$ is the lattice translation vector, n the band number and $\mathbf{k}$ the reciprocal lattice vector. WFs are not uniquely defined because, in the single band case, there is a freedom of choice of the phases of the Bloch functions, $|\Psi_{n\mathbf{k}}\rangle$, as a function of $\mathbf{k}$, and in the multiband case, any set of orthogonal linear combination of Bloch functions $|\Psi_{n\mathbf{k}}\rangle$ could be used in (5.1). The uncertainty in the WF's definition corresponds to a freedom of choice for a unitary transformation matrix $U_{jn}^{(\mathbf{k})}$

$$|\Psi_{n\mathbf{k}}\rangle \rightarrow \sum_j U_{jn}^{(\mathbf{k})} |\Psi_{j\mathbf{k}}\rangle. \tag{5.2}$$

A commonly used approach to generate WFs was proposed by N. Marzari and D. Vanderbilt [217]. They use a condition of maximum localization of the WFs (MLWFs), that consists in a variational procedure for the matrix $U_{jn}^{(\mathbf{k})}$. As an initial step before the variational process, a set of trial localized orbitals (in fact atomic orbitals) was chosen and projected onto the subspace of Bloch functions. Later [218] it was shown that this initial guess for the WFs of transition-metal oxides is usually so good that the variational procedure can be dropped and the projection of the trial orbitals onto the subspace of Bloch functions can be used to define the unitary transformation matrix $U_{jn}^{(\mathbf{k})}$.

5.1.5.1 Maximum localization of the WFs

We use this approach for a qualitative analysis because an analysis of the full charge distribution in term of the maximally-lpcalized Wannier functions would be rather complex. A simple picture of the charge ordering can be obtained by constructing occupation-resolved WFs (ORWFs) [219] from the two e_g fully occupied bands. For this purpose we choose an energy window of [10.0, E_f] eV for up-spin. The resulting WFs are centered at the Ni-site as illustrated in Fig.5.5.

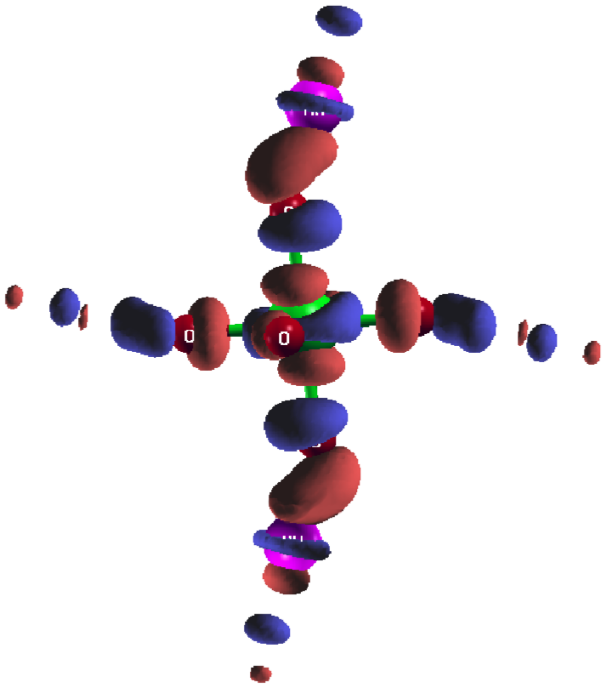

Figure 5.5: An occupied e_g WF centered on Ni (green) showing remarkable delocalization to the neighboring Mn (violet).

To devise ways of attributing electron charges to a given atom, we observe that the majority t_{2g} WF's centered on Mn are fully occupied and all others are empty; all Ni-centered WFs except minority e_g are fully occupied. Each WF is normalized, hence contains one electron. Now the individual electrons occupying a WF centered on an atom are attributed to that atom. This yields a formal valency of 4+ for Mn and 2+

for Ni. Having recovered the nominal ionic state of the two cations, we also obtain the nominal charge disproportionation.

Of course, as exemplified by Fig.5.5, a major fraction of the unit charge lodged in a WF centered on a given atom spills out of the sphere centered on that atom into neighboring ones, and will therefore be attributed to other atoms when the charge is integrated in the spheres. This charge spill-out will cause the *actual* charge disproportionation to be much smaller than nominal. We may argue that the small directly-calculated disproportionation does not conflict with the ionic picture, in the precise and limited sense just outlined.

Notice that as already mentioned LNMO is a FM insulator where the double-exchange interaction is dominant. This results from the interaction of the filled *d* orbital of one metal ion with the vacant *d* orbital of another metal ion through anion *p* orbital. Fig.5.6 shows the overlap between MLWFs, placed at neighboring NiO_6 and MnO_6 octahedra of LNMO calculated in the FM RH phase: the superexchange path is mediated by the corner-shared O. The Mn and Ni-centered WFs should be thought as empty and filled, respectively, in the double-exchange picture.

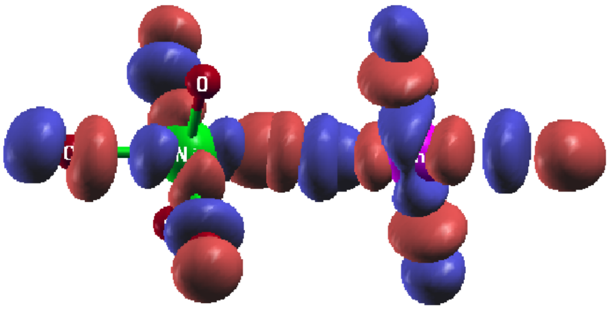

Figure 5.6: Overlap between MLWFs, placed at neighboring NiO_6 and MnO_6 octahedra of LNMO calculated in the RH phase, showing the double-exchange path mediated by the corner-shared O. The MLWFs are centered on Ni (green) and Mn (violet).

5.1.5.2 Projected Wannier functions

An alternative use of WFs in the context of the evaluation of atomic charges is to calculate the Wannier occupancy matrix for WFs generated in a wide energy window including empty states. Here we employ the pseudopotential method and a plane wave basis set. Hence, site centered pseudoatomic orbitals ϕ_n were chosen as a set of trial orbitals [212].

Nonorthogonalized approximations to the WFs in the direct $|\widetilde{W}_n^{\mathbf{T}}\rangle$ and reciprocal space $|\widetilde{W}_{n\mathbf{k}}\rangle$ are calculated as projection of the pseudoatomic orbitals onto a subspace of Bloch functions that is defined by setting an energy interval $E_1 \leq \varepsilon_i(\mathbf{k}) \leq E_2$ or some band numbers $N_1 \leq i \leq N_2$:

$$|\widetilde{W}_n^{\mathbf{T}}\rangle = \sum_{\mathbf{k}} |\widetilde{W}_{n\mathbf{k}}\rangle e^{-i\mathbf{kT}}, \tag{5.3}$$

$$|\widetilde{W}_{n\mathbf{k}}\rangle \equiv \sum_{i=N_1}^{N_2} |\Psi_{i\mathbf{k}}\rangle\langle\Psi_{i\mathbf{k}}|\phi_{n\mathbf{k}}\rangle = \sum_{E_1\leq\varepsilon_i(\mathbf{k})\leq E_2} |\Psi_{i\mathbf{k}}\rangle\langle\Psi_{i\mathbf{k}}|\phi_{n\mathbf{k}}\rangle. \tag{5.4}$$

To generate orthogonalized WFs, one should define the overlap matrix:

$$O_{nn'}(\mathbf{k}) \equiv \langle\widetilde{W}_{n\mathbf{k}}|\widetilde{W}_{n'\mathbf{k}}\rangle \tag{5.5}$$

Orthogonalized Wannier functions are then obtained as:

$$|W_n^{\mathbf{T}}\rangle = \sum_{\mathbf{k}} |W_{n\mathbf{k}}\rangle e^{i\mathbf{kT}}, \tag{5.6}$$

where

$$|W_{n\mathbf{k}}\rangle = \sum_{n'} (O_{nn'}(\mathbf{k}))^{-\frac{1}{2}} |\widetilde{W}_{n'\mathbf{k}}\rangle \tag{5.7}$$

with the Wannier functions occupancy matrix Q_{nm}^{WF} [212] given by:

$$Q_{nm}^{WF} \quad = \langle W_n^0| \left(\sum_{\mathbf{k}} \sum_{i=N_1}^{N_2} |\Psi_{i\mathbf{k}}\rangle \theta(\varepsilon_i(\mathbf{k}) - E_f)(\mathbf{k})\langle\Psi_{i\mathbf{k}}| \right) |W_m^0\rangle \tag{5.8}$$

where θ is the step function and E_f is the Fermi energy. For our purpose we choose an energy window of [10.0, 17.0] eV for both spin channels. The choice is based on the projected DOS and calculated band structure (Fig.5.2) where we note that the d-states are located in the energy window from ∼10.0 eV to ∼17.0 eV. In Fig.5.7 we compare

Wannier occupation d-orbital	Ni	Mn
Up	4.715	3.040
Down	3.040	0.145
total	7.755	3.185

Table 5.3: *d*-Wannier occupation calculated with Eq.5.8

the DFT and the *d*-WFs bands: we can see that they match almost exactly, except around some band crossings. In Tab.5.3 we show the occupation of *d*-WFs calculated with Eq.5.8. Our result suggest that the oxidation state for Ni and Mn is +2.25 and +3.82 respectively with a disproportion of 1.57 electrons. We note that the projected Wannier functions will in general depend on the specific choice of the radial part of the atomic orbital, as well as on the energy window chosen for the construction. In the latter sense, the WF-based evaluation of charge disproportionation still contains major element of arbitrariness.

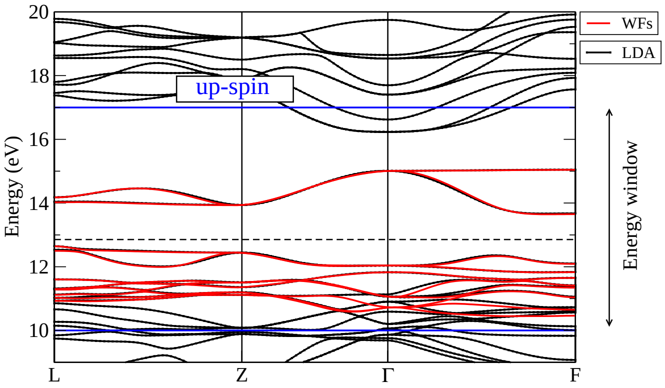

(a) up-spin

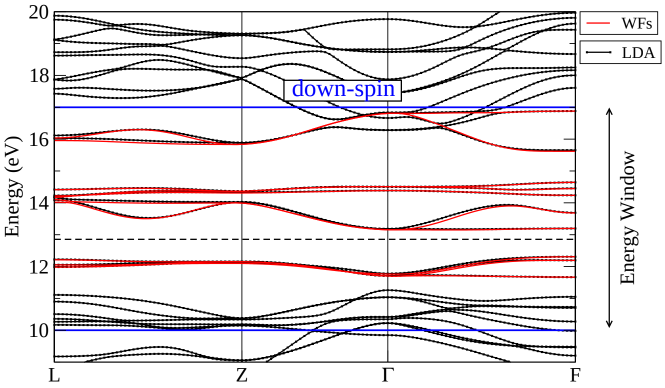

(b) down-spin

Figure 5.7: DFT band structure (black lines) for FM RH LNMO: (a) up-spin, (b) down-spin FM. The blue lines demarcate the energy window. *d*-WF bands are depicted as red lines.

5.1.6 Conclusions

Ion	Nominal	$DOS_{1/2bond}$	Bader	Wannier
Mn	+4	+3.0	+1.66	+3.82
Ni	+2	+2.5	+1.19	+2.25
δQ	2	0.5	0.47	1.57

Table 5.4: Summary of charge analysis. In the last row (δQ) we compare the nominal charge disproportion with that calculated in this work.

From our analysis we can draw the following conclusions:

- The ambiguity in defining the volumes used for atom-projected DOS calculation is the fundamental problem of the method and generally any choice could be questionable: the choice of the volume is not a simple task.
- An elegant method is the Bader decomposition, which uses stationary points in the three-dimensional electron density to partition charge among different atoms. One limitation of this approach is that it will tend to produce geometrically sensible (Voronoi-polyhedra-like) regions, which however do not necessarily match the bonding situation in the solid. Indeed, it tends to produce ionicities much smaller than nominal.
- With maximally-localized Wannier functions, we reconcile the Ni^{2+}/Mn^{4+} picture with weak charge disproportion.
- The projected Wannier functions provides useful, non-trivial occupations, which however will in general depend on the specific choice of the radial part of the atomic orbital and on the energy window.
- Not surprisingly, as seen in Tab.5.4 the various methods give scattered results, qualitatively confirming a charge disproportionation between Ni and Mn.

5.2 Order, phase transitions, and transport in ultra-thin nickelate superlattices

We have a forthcoming paper: "Ordered ground state and phase transitions in ultra-thin nickelate superlattices". This is essentially my own work. The planning and assessment of the work was done in collaboration with the supervisors.

5.2.1 Introduction

Correlated materials are often characterized by incipient or actual instabilities towards collective ordered states. Two recent sets of experiments [220, 221, 222] have investigated phase transitions playing out in $LaNiO_3$ (LNO, in bulk the only metallic Pauli-paramagnetic rare-earth nickelate) in an intentionally perturbed environment, namely epitaxially-strained ultra-short superlattices (SL) of LNO layers alternated with the band insulator $LaAlO_3$ (LAO). These elegant nanostructuring manipulations of materials properties revealed nearly concurrent transitions from a non-magnetic normal metal to a long-range-ordered magnetic, insulating, charge-ordered state for sufficiently thin LNO (2-3 layers at most), observing a crossover to an insulator-like conductivity temperature (T) dependence, spectral weight transfer in optical conductivity [220], and XAS (x-ray absorption spectroscopy) line splitting [221, 222]. Magnetometry (measuring zero total magnetization) and μSR (muon spin rotation, detecting magnetic moments with a lower-bound value 0.5 μ_B and line shape compatible with long-range order) lend support to long-range antiferromagnetic (AF) order [220].

The precise nature of the low-T state of the LNO/LAO SL and the transitions it undergoes is unclear. In this section we address the problem studying ultrathin (1+1 and 1+2-layer) LNO/LAO SLs under tensile strain using variational self-interaction-corrected local density functional theory (VPSIC) [3, 4, 5], which notoriously provides a markedly improved description of correlated and magnetic materials [5, 134] compared to conventional semi-local approaches. Our ground state is structurally dimerized, charge-ordered, insulating, and antiferromagnetic with modulation vector $(0,\pi/2)$, in analogy with bulk rare-earth nickelates (this state is labeled AFD henceforth). From the calculated energetics, we infer antiferromagnetic (AF) to paramagnetic (PM) and insulating-metal (IMT) transitions at two distinct critical temperatures (50 and 150 K respectively). The AF-PM transition is driven by superexchange, the IMT by **Mott**

localization, valency disproportionation and structural dimerization of Ni atoms at low T. All the above results are consistent with experiments of Ref.[220]; in addition, to elucidate the experiments of Ref.[221, 222] we calculate the SLs conductivity by Bloch-Boltzmann approach [223, 224], showing a transition of the electron-doped AF insulating ground state undergoes a transition from hopping to band conductivity at 150 K, wich may reconcile Ref.[221, 222] with Ref.[220].

Finally, we find that the high-T metallic PM phase has a Fermi surface (FS) akin to optimally-doped cuprates, as foreshadowed in earlier theoretical work [225, 226].

5.2.2 Method

Total energy, force, and band structure calculations are performed by VPSIC [5] using the plane-wave ultrasoft pseudopotential method in the supercell approach. The epitaxially-strained LNO/LAO (1+1) SL is simulated at an in-plane lattice constant fixed to that of $PrScO_3$, corresponding to a tensile planar strain of about 3%. The LNO layers contain up to four Ni atoms to simulate antiferromagnetism. We optimize the cell length, and atomic positions according to quantum forces [5]. Band energies calculated on a dense 2050-**k** point grid are used in Bloch-Boltzmann transport theory within a relaxation time approximation to obtain dc conductivity [227].

5.2.3 Structure and charge ordering

In the AFD ground state the nominally trivalent Ni(III) atoms of LNO are inequivalent due to strong cooperative dimerization of the Ni-centered octahedra. All Ni-O bonds around each Ni either expand or contract from 2 Å to 2.19 Å or respectively 1.83 Å in a predominantly breathing mode. The calculated octahedra rotations are rather small (∼1-2°). The short and long bonds match those, respectively, in peroxonickel complexes with nominal tetravalent Ni(IV) and NiO with nominal divalent Ni(II). (We use these labels below). The distortion is accompanied by charge transfer from Ni(IV) to Ni(II), which we quantify by VPSIC occupations [3]. The total transfer is 0.07 $|e|$, in fair agreement with the 0.03 $|e|$ estimated [220] from the difference of integrated optical conductivity above and below the transition. This charge-ordered bond-dimerized phase clearly is in line with a $[2\,\mathrm{Ni(III)} \rightarrow \mathrm{Ni(II)} + \mathrm{Ni(IV)}]$ disproportionation suggested by the splitting in the SL XAS spectra, analogous to insulating nickelates [221, 222].

The magnetic order and insulating character of this state confirm this conclusion, as discussed below.

5.2.4 Magnetism

In the AFD state the structural and valency dimerization are associated with the AF pattern sketched in Fig.5.8. Ni(II)'s [squares, circles in the Figure] carry a moment $\mu_{\mathrm{Ni(II)}}=\pm 1.44\ \mu_B$, while Ni(IV)'s [crosses in the Figure] have zero moment, confirming a picture of Ni(III) disproportionation into unpolarized Ni(IV) $t_{2g}^6 e_g^0$ and polarized Ni(IV) $t_{2g}^6 e_g^2$. The planar modulation wavevector is $(0,\pi/2)$ on the $(\mathbf{a},\mathbf{b})$ basis, similarly to bulk nickelates and monoxides [5, 100]; in our single-LNO-layer cell, there is no vertical modulation by construction. Our result agrees with μSR [220] lower-bound moment 0.5 μ_B (below 40 K for tensile strain), with magnetometry ruling out ferromagnetism, and μSR asymmetry lineshapes [220] favoring long-range order.

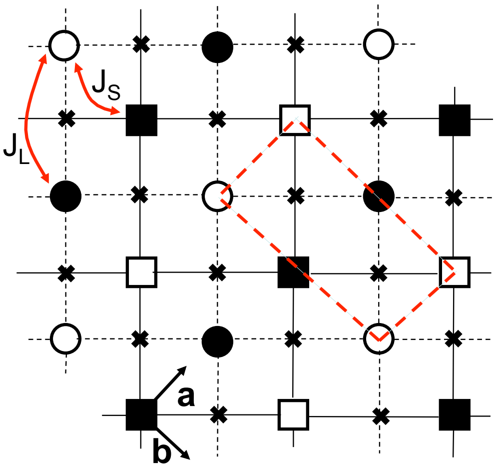

Figure 5.8: Magnetic order of the LNO/LAO (1+1) SL. Squares, circles: up (filled) and down (empty) polarized Ni(II); crosses: unpolarized Ni(IV). Circles and squares indicate distinct interpenetrating cubic AF lattices (see text). Oxygens (not shown) sit on connecting lines roughly halfway between Ni's. The $2\sqrt{2}\times\sqrt{2}$ simulation cell is indicated (long-dash).

To estimate the critical temperature of the magnetic transition, we map our pattern on a Ising model. The AFD structure, with in-plane couplings J_L and J_S (Fig.5.8), consists of two interpenetrating simple-cubic antiferromagnetic-G lattices (circles, dashed lines, and, respectively, squares and solid lines in Fig.5.8). The AFD magnetic energy does not depend on J_S, so the two sub-lattices are decoupled, and the critical temperature can be estimated for each of them separately. Since only the Ni-O bond parallel e_g orbitals are spin-polarized and contribute to the magnetic coupling, the diagonal J_S exchange interaction is arguably negligibly weak.

From the energies of AFD and ferromagnetic (FM) phases, since

$$E_{\mathrm{AFD}} - E_{\mathrm{FM}} = (8J_L + 4J_S)\mu^2_{\mathrm{Ni(II)}} \simeq 8J_L\mu^2_{\mathrm{Ni(II)}} \tag{5.9}$$

(see Fig.5.8), we extract an antiferromagnetic J_L=–11.2 meV. The FM is also insulating and has the same moments, structure, and charge-ordering pattern, showing that the AFD ordering is simply driven by AF superexchange. As the vertical coupling $J_\perp$ across the LAO layer should be very weak compared to the in-plane J_L (i.e. the anisotropy $J_L/J_\perp$ is large), we use results for the 3D anisotropic AF Ising model [228] in the asymptotic large anisotropy limit obtaining $\mathrm{T_N}$≃0.40 J_L/k_B∼33 K, rather close to the experimental 40 K.

5.2.5 Electronic structure and metal-insulator transition

The concurrent action of dimerization and magnetic superstructure open an electronic gap in the AFD phase. Fig.5.2.5 reports the bands (left), and the density of states (DOS) projected on Ni(II), center, and Ni(IV), right. The gap is 1.3 eV, indirect. The projected DOS shows that the top valence states are predominantly Ni(II) and of mixed e_g-O_p character, while the low conduction states are mostly Ni(IV), in agreement with the dimerization being the driving mechanism. The conduction band bottom (CBB) is very flat throughout the BZ, an essential trait to interpret transport results for the electron-doped AFD phase. The Ni(IV)-Ni(II) charge transfer is associated in optical experiments to a spectral weight depletion below 0.4 eV, which is identified as the "charge gap" [220]. Our best shot at this gap is the (admittedly somewhat larger) electronic gap, originating from the combined structure, charge, and magnetic ordering. Indeed, we point out that the octahedra distortion is essential to obtain a gap. Forbidding distortion, all simulated phases are metallic and show no charge transfer. Only the Pauli-PM metal is stable among these; e.g., the G-type AF dimerizes spontaneously to a ferrimagnetic marginal metal with Ni-Ni charge transfer.

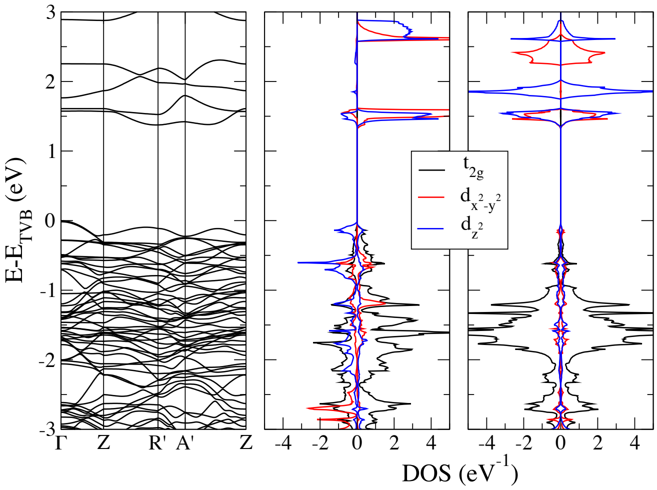

Figure 5.9: Bands (left; zero at valence band top) and DOS of the AFD states, projected on Ni(II), center,and Ni(IV), right.

Since the IMT is associated to dimerization, the transition T is that at which the structure undimerizes thermally, with attendant gap closure. The full distorted-octahedra population N_0 is thermally activated out of the low-T ground state into the high-T state as $N_0 \exp(-Rt)$ whenever the Arrhenius rate $R=\nu_0 \exp(-\Delta E/k_B T)$ become appreciable–say, unity. Since the Pauli-PM is the only stable undimerized state, we envisage an AFD-PM transition and use the AFD-PM energy difference ΔE=0.20 eV/Ni atom. With a plausible prefactor ν_0=5 THz [229], R=1 Hz corresponds to $T_c \simeq$80 K, in fair agreement with 100 K experimentally.

The PM phase has a large hole-like Fermi surface (Fig.5.10) centered at the 1×1 Brillouin zone corner, analogous to optimally-doped cuprates, confirming earlier theoretical suggestion [225, 226]. Unlike cuprates, however, the states character is mixed e_g.

To compare our results with alternative methods, we note that LSDA finds no stable AF phase and obtains undimerized structures even starting from dimerized and polarized initial conditions. LDA+U does not stabilize the AF phase and predicts [230] a gapped FM phase (not seen in experiment; it is unclear if a different U may obtain the observed phase). Our method does not use tuning parameters. Its agreement with experiment suggests an improved account for on-site correlation compared to

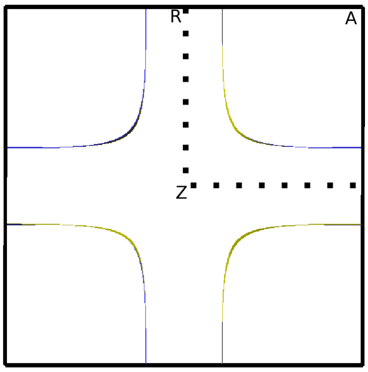

Figure 5.10: Fermi surface of the PM phase.

other methods. Further supporting this contention, we find agreement with dynamical mean field theory (DMFT) for the simplified-geometry PM state where it was applied; our Fermi surface in the PM phase is analogous to that of DMFT [226], and in the undimerized AF G-type phase (results not shown) we obtain a pseudo-gapped DOS similar to DMFT [231] at large U.

5.2.6 Transport

The dc σ(T) of Ref.[221, 222] does not signal a proper IMT in the ultrathin SLs (3 LNO layers or less), but rather an anomalous hopping-like T-dependence; thicker-LNO SLs behave as normal metals with large residual resistivity. To resolve this discrepancy we calculate σ within BBT with energy-dependent relaxation time, known to be accurate for doped insulators [223]. We suggest that the thick normal-metal SL corresponds to the Pauli-PM phase, and the ultrathin SL to the electron-doped AFD phase (typical defects, e.g. oxygen vacancies, in transition metal oxides are donors).

We tune the parameters of the relaxation time model to reproduce the $\sigma \sim T^{3/2}$ normal-metal behaviour reported in Ref.[221, 222] (Fig.5.11, top) for the Pauli-PM. Then we combine the same relaxation-time model with the bands of the AFD phase, to obtain σ(T) for the n-doped Mott phase (Fig.5.11). Our results fit nicely the data [221, 222]: at low T σ grows exponentially, then saturates to a metallic linear behavior above T$\sim$150K. To understand this result, we analyze σ as a function of μ and T.

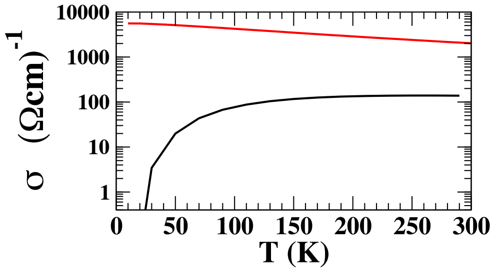

Figure 5.11: Calculated conductivity vs. T for metallic PM phase (red line) and n-doped AFD phase (black)

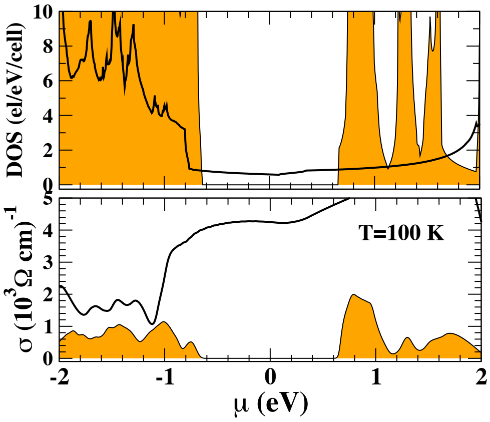

Figure 5.12: Density of states (upper panel) and conductivity (lower panel) for metallic PM phase (black line) and AFD phase (orange-filled line) as function of chemical potential.

Fig.5.12 compares the total DOS and $\sigma(\mu)$ (at 100K) for PM and AFD. The flat PM DOS near E$_F$ gives σ_{PM}~4 kS/cm, while σ_{AFD}<2 kS/cm near the CBB. The inset of Fig.5.13 shows a marked slope discontinuity near the AFD CBB DOS, separating a steep 10-meV-wide lower region from a higher-energy flatter side, signaling the crossover in the e_g CBB from hopping-like flat-band to dispersed metallic regime. This hopping-to-band conductivity transition is in the upper panel of Fig.5.13 where $\sigma(\mu)$ is reported for a range of temperatures from 10K (blue thickest line) up to 290K (red thickest line) (the change in color highlight the transition at T=150-170K). The solid vertical line indicate the threshold value μ_t = 0.662 eV whch separate two distinct conductivity regimes: in the low-μ region σ grows exponentially with μ and T, and

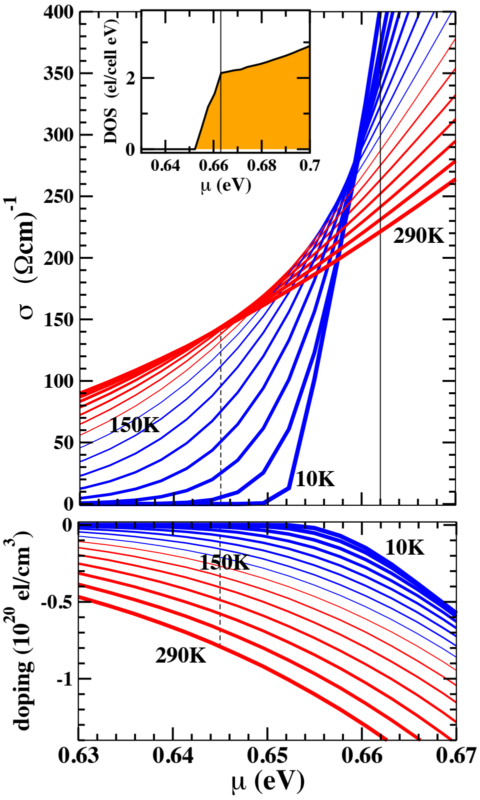

Figure 5.13: Conductivity (upper panel) and doping (lower panel) vs. chemical potential and temperature. Temperature is varied from 10 K (thickest blue line) up to 290 (thickest red line), progressively increasing by 20 K at each curve. Inset: detail of the DOS near the conduction bottom; dashed (solid) vertical lines mark μ^* (μ_t), see text.

for fixed μ it saturates to nearly constant values around T=150K; above μ_t σ recovers normal-metal behaviour: it decreases with T, and grows linearly with μ. The dashed vertical line marks the reference value μ^*, falling well in the middle of the hopping conduction region, assumed for the calculation of σ(T) in Fig.5.11. Finally, in lower panel of Fig.5.13 we report doping concentration curves n(μ) for the same temperature range. At μ=μ^* (dashed vertical line) n grows with T from zero up to 8×10^{19} cm^{-3} (0.52 electrons/cell) at 290K, crossing the boundary of the transition (T=150K) for n ~2×10^{19} cm^{-3} (0.13 electrons/cell), which closely match the integrated DOS in the 10-meV steepest region (the vertical line in the inset). The interpretation of our results is simple: the low-μ regime (low dopant concentration) characterized by hopping-like conductivity, corresponds to carriers progressively filling the steepest DOS edge; at higher μ (i.e. highest dopant concentration) carriers start to fills the higher-energy flatter DOS region and the normal metal behavior takes place.

5.2.7 Summary

Ab initio calculations suggest that LNO/LAO ultra-short-period SLs have a structurally- and valency-dimerized charge-ordered insulator ground state, making phase transitions to a metallic Pauli paramagnet. The magnetic and metal-insulator critical temperatures are estimated around 35 K and 80 K respectively. This interpretation is in good agreement with available experimental data. We have also calculated the electron conductivity as function of chemical potential and temperature, showing that the electron-doped AFD phase undergoes a hopping-conductivity to metal-conductivity phase transition at T$\sim$150 K, thus providing a sound interpretation to the results of transport experiments.

Summary & Outlook

The main aim of this work was to improve our understanding of strongly correlated materials. For this reason we have used the Pseudo–Self-Interaction approach and developed the Variational-Pseudo–Self-Interaction formulation. These aspects are reflected in the five chapters of this thesis:

- In chapter 1 we introduced the Pseudo–Self-Interaction and presented the new variational approach.

- Chapter 2 was devoted to cuprate superconductors. In particular we approached the problem of Shubnikov-de Haas (SdH) and de Haas-van Alphen (dHvA) quantum oscillation observed in the underdoped cuprate $YBa_2Cu_3O_{6.5}$, and we have suggested that the experimentally observed pockets are a property of a state characterized by some form of magnetic ordering. Moreover we clarified theoretically the properties of the possible stable structures of bulk rocksalt-like CuO.

- In chapter 3 we tested the new Variational Pseudo-Self-Interaction formalism on $YTiO_3$ and $LaTiO_3$. We discussed electronic and structural properties and showed that this new approach is very helpful to understand the differences between $YTiO_3$ and $LaTiO_3$.

- In chapter 4 we analyzed the MnO and NiO magnetic properties under pressure by both standard (LDA and PBE) and advanced first–principles methods (VPSIC and the Heyd, Scuseria and Ernzerhof hybrid functional). We showed that the results provided by VPSIC and HSE are quite consistent, and satisfactory in comparison to experiment.

– The final chapter (Chap.5) was devoted to nickelates. We first faced the problem of charge disproportionation in the double perovskite La_2NiMnO_6 confirming qualitatively the charge disproportionation between Ni and Mn. Then we analyzed the magnetic and electronic properties of the 1/1 layered system $LaAlO_3/LaNiO_3$.

The unifying aspect of most of the topics tackled in this work is the need for major corrections to semi-local (LDA or GGA) exchange-correlation to obtain even qualitatively correct results. The basic issue is that the effective promotion cost of an electron from a site to the next (U, in Hubbard parlance) is grossly underestimated by LDA due to the self-interaction, and as a consequence metallicity often spuriously prevails: e.g., CuO is metallic and non-magnetic in LDA, and MnO and NiO are marginal small-gap insulators only due to combinations of crystal fields and small Hund exchange.

PSIC removes the spurious on-site self-interaction repulsion present in e.g. LDA and, judging from the empirical evidence, it appears to restore the on-site interaction to values that capture well the energy scale typically associated to U in the Hubbard model. The outcome is that the correct (qualitatively and most of the time quantitatively) ground states and electronic structures are regained. CuO, MnO and NiO, e.g., are large-gap charge-transfer insulators, with the correct character of near-gap states. As a byproduct, pSIC can estimate the effective U from the density of states, and that U usually agrees with those estimated or guessed in LDA+U. In some cases (not discussed in this work), the electronic structure is characterized by two distinct U scales, which the PSIC captures correctly [232] and automatically. In insulators and wide gap semiconductors the (V)PSIC reduces the excessive delocalization of the valence states (typically p states of oxygen or nitrogen) correcting the gap error of LDA or GGA. On the other hand (V)PSIC works less well on Si or Ge, and generally in small gap systems, where other sources of error are comparable.

One aspect to improve in this version of SIC is the fact that the SI potential is assumed linearly dependent on the occupation number (Eq.1.13). This is correct for the Hartree term, which is the dominant contribution for large occupation numbers, whereas it introduces a nonlinearity error of $\mathcal{O}(p_i^{1/3} - p_i)$ in the exchange-correlation part. Another potential pitfall is the possible tendency (common to hybrid and SIC approaches) to over-correct the delocalization and the hybridization of the LDA, as indeed LDA + U does with large U. At least, the (V)PSIC overcorrection is self-contained and not dependent from parameters.

Another issue is how well the LDA-SIC mimics the "real" self-energy of the interacting system (ie, the effective interaction potential, energy-dependent and non-local, among electrons beyond Hartree). It is plausible that this version of SIC is implicitly non-local and energy-dependent as the self-energy must be. In fact, since PSIC corrects every state in dependence on the projection of the Bloch states, typically the band energies ("quasiparticles") are corrected differently for different energies, that is, in an energy dependent manner. The "quasiparticle corrections", i.e. the energy-dependent difference of LDA and pSIC eigenvalues, mirror quite closely those obtained by GW and by hybrids, for instance, in ZnO. This suggests that the common dominant ingredient of all these approaches on the electronic structure is self-interaction removal. Further, since the SIC corrections depend on angular momentum and atomic site, each Bloch state, having different projections on each channel and on each site, sees different potentials for the same angular momentum. In this sense the correction is (although it is not obvious to prove it) implicitly non-local.

Finally we remark that three variants of PSIC were mentioned in Chap.1: original (PSIC), variational (VPSIC), and simplified variational (VPSIC0). PSIC was used in Chap.2, VPSIC in Chap.3, 4, and 5. No results obtained with VPSIC0 are presented here, but the method was analyzed in Ref.[5] (material not reported in this work). As Ref.[5] discusses in detail, PSIC and VPSIC are largely equivalent in terms of electronic structure. VPSIC, however, uses a more robustly defined total energy which should give more reliable structures; importantly, unlike PSIC, it allows for the calculation of forces. VPSIC0 is a simplified version of VPSIC that will allow less costly force calculations and structural relaxations. Its performance is comparable to the other versions in non-magnetic systems, but unfortunately is less than impressive for magnetic systems.

Bibliography

[1] Francis Galton. *Hereditary Genius.* MacMillan and Co., 1869. 1

[2] J. Hubbard. Electron Correlations in Narrow Energy Bands. *Proceedings of the Royal Society of London. Series A - Mathematical and Physical Sciences*, 276(238), 1963. 2

[3] A. Filippetti and N. A. Spaldin. Self-interaction-corrected pseudopotential scheme for magnetic and strongly-correlated systems. *Phys. Rev. B*, 67(125109), 2003. 2, 6, 10, 11, 17, 22, 46, 107, 108

[4] A. Filippetti and V. Fiorentini. A pratical first-principles band-theory approach to the study of correlated materials. *The European Physical Journal B*, 71(139), 2009. 2, 6, 17, 22, 70, 107

[5] A. Filippetti, C. D. Pemmaraju, S. Sanvito, P. Delugas, D. Puggioni, and Vincenzo Fiorentini. Variational pseudo-self-interaction-corrected density functional approach to the *ab initio* description of correlated solids and molecules. *Phys. Rev. B*, 84(195127), 2011. 2, 13, 55, 68, 70, 74, 91, 107, 108, 109, 119

[6] Wolter Siemons, Gertjan Koster, Dave H. A. Blank, Robert H. Hammond, Theodore H. Geballe, and Malcolm R. Beasley. Tetragonal CuO: End member of the 3d transition metal monoxides. *Phys. Rev. B*, 79(195122), 2009. 3, 46, 49, 50, 53

[7] P. Fulde. *Electron Correlations in Molecules and Solids, 2nd ed.* (Springer-Verlag, Berlin, 1995). 5

[8] K. Terakura, T. Oguchi, A.R. Williams, and J. Kübler. Band theory of insulating transition-metal monoxides: Band-structure calculations. *Phys. Rev. B*, 30(4734), 1984. 5

[9] G.A. Sawatzky and J.W. Allen. Magnitude and origin of the band gap in NiO. *Phys. Rev. Lett.*, 53(2339), 1984. 5

[10] R. Zimmermann, P. Steiner, R. Claessen, F. Reinert, S. Hüfner, P. Blaha, and P. Dufek. Electronic structure of 3d-transition-metal oxides: on-site coulomb repulsion versus covalency. *J. Phys.: Condens. Matter*, 11(1657), 1999. 5

[11] W.E. Pickett. Electronic structure of the high-temperature oxide superconductors. *Rev. Mod. Phys.*, 61(433), 1989. 5

[12] H. Sawada, Y. Morikawa, K. Terakura, and N. Hamada. Jahn-teller distortion and magnetic structures in $LaMnO_3$. *Phys. Rev. B*, 56(12154), 1997. 5

[13] A. Filippetti and N.A. Hill. Coexistence of magnetism and ferroelectricity in perovskites. *Phys. Rev. B*, 65(195120), 2002. 5

[14] V.I. Anisimov andJ. Zaanen and O.K. Andersen. Band theory and Mott insulators: Hubbard U instead of Stoner I. *Phys. Rev. B*, 44(943), 1991. 6

[15] A. D. Becke. Density-functional thermochemistry. iii. the role of exact exchange. *J. Chem. Phys.*, 98(5648), 1993. 6

[16] J. F. Janak. Proof that $\partial E/\partial n_i = \epsilon$ in density-functional theory. *Phys. Rev. B*, 18(7165), 1978. 6, 11, 13

[17] J.P. Perdew and A. Zunger. Self-interaction correction to density-functional approximations for many-electron systems. *Phys. Rev. B*, 23(5048), 1981. 7, 11, 12, 14

[18] A. Filippetti. Electron affinity in density-functional theory in the local-spin-density approximation. *Phys. Rev. A*, 57(914), 1998. 7

[19] B. Y. Tong and L. J. Sham. Application of a self-consistent scheme including exchange and correlation effects to atoms. *Phys. Rev.*, 144(1), 1966. 7

[20] A. Zunger, J.P. Perdew, and G.L. Oliver. A self-interaction corrected approach to many-electron systems: Beyond the Local Spin Density Approximation. *Solid State Communications*, 34(933), 1980. 7

[21] A. Svane and O. Gunnarsson. Transition-metal oxides in the self-interaction-corrected density-functional formalism. *Phys. Rev. Lett.*, 65(1148), 1990. 8, 11, 68

[22] A. Svane. Electronic structure of La_2CuO_4 in the self-interaction-corrected density-functional formalism. *Phys. Rev. Lett.*, 68(1900), 1992. 8

[23] A. Svane. Electronic structure of cerium in the self-interaction corrected local spin density approximation. *Phys. Rev. Lett.*, 72(1248), 1994. 8

[24] Z. Szotek, W.M. Temmermann, and H. Winter. Self-interaction corrected, local spin density description of the $\gamma \rightarrow \alpha$ transition in Ce. *Phys. Rev. B*, 47(4029), 1993. 8, 68

[25] M. Arai and T. Fujiwara. Electronic structures of transition-metal mono-oxides in the self-interaction-corrected local-spin-density approximation. *Phys. Rev. B*, 51(1477), 1995. 8

[26] R.A. Heaton, J.G. Harrison, and C.C. Lin. Self-interaction correction for density-functional theory of electronic energy bands of solids. *Phys. Rev. B*, 28(5992), 1983. 8

[27] M.R. Pederson, R.A. Heaton, and C.C. Lin. Local-density Hartree-Fock theory of electronic states of molecules with self-interaction correction. *J. Chem. Phys.*, 80(1972), 1984. 8

[28] M. Stengel and N.A. Spaldin. Self-interaction correction with Wannier functions. *Phys. Rev. B*, 77(155106), 2008. 8

[29] D. Vogel, P. Krüger, and J. Pollmann. Self-interaction and relaxation-corrected pseudopotentials for II-VI semiconductors. *Phys. Rev. B*, 54(5495), 1996. 9

[30] L. Kleynmann and D. M. Bylander. Efficacious form for model pseudopotentials. *Phys. Rev. Lett.*, 48(1425), 1982. 9, 15

[31] C. Stampfl, C.G. Van de Walle, D. Vogel, P., Krüger, and J. Pollmann. Native defects and impurities in InN: First-principles studies using the local-density approximation and self-interaction and relaxation-corrected pseudopotentials. *Phys. Rev. B*, 61(R7846), 2000. 9

[32] D. Vogel, P. Krüger, and J. Pollmann. Ab initio electronic structure of silver halides calculated with self-interaction and relaxation-corrected pseudopotentials. *Phys. Rev. B*, 58(3865), 1998. 9

[33] C. D. Pemmaraju, T. Archer, D. Sanchez-Portal, and S. Sanvito. Atomic-orbital-based approximate self-interaction correction scheme for molecules and solids. *Phys. Rev. B*, 75(045101), 2007. 16

[34] Danilo Puggioni, Alessio Filippetti, and Vincenzo Fiorentini. Fermi-surface pockets in $YBa_2Cu_3O_{6.5}$: Comparison of *ab initio* techniques. *Phys. Rev. B*, 79(064519), 2009. 19, 44

[35] A. Filippetti, D. Puggioni, and V. Fiorentini. Fermi-surface pockets in magnetic underdoped cuprates from first principles. *EPL*, 88(67009), 2009. 19

[36] N. Doiron-Leyraud, C. Proust, D. LeBoeuf, J. Levallois, J-B. Bonnemaison, X. Liang, D. A. Bonn, W. N. Hardy, and L. Taillefer. Quantum oscillations and the Fermi surface in an underdoped high-T_c superconductor. *Nature*, 447(565), 2007. 19, 20, 28, 32, 33, 38, 39, 42

[37] D. LeBoeuf, N. Doiron-Leyraud, J. Levallois, R. Daou, J. B. Bonnemaison, N. E. Hussey, L. Balicas, B. J. Ramshaw, R. Liang, D. A. Bonn, W. N. Hardy, S. Adachi, C. Proust, and L. Taillefer. Electron pockets in the Fermi surface of hole-doped high-T_c superconductors. *Nature*, 450(533), 2007. 19, 20, 28, 32, 33, 38, 39, 42

[38] Cyril Jaudet, David Vignolles, Alain Audouard, Julien Levallois, D. LeBoeuf, Nicolas Doiron-Leyraud, B. Vignolle, M. Nardone, A. Zitouni, Ruixing Liang, D. A. Bonn, W. N. Hardy, Louis Taillefer, and Cyril Proust. de haas˘van alphen oscillations in the Underdoped High-Temperature Superconductor $YBa_2Cu_3O_{6.5}$. *Phys. Rev. Lett.*, 100(187005), 2008. 19, 20, 28, 32, 38, 39, 42

[39] E. A. Yelland, J. Singleton, C. H. Mielke, N. Harrison, F. F. Balakirev, B. Dabrowski, and J. R. Cooper. Quantum Oscillations in the Underdoped Cuprate $YBa_2Cu_4O_8$. *Phys. Rev. Lett.*, 100(047003), 2008. 19, 33

[40] Chakravarty S. and Kee H.-Y. Fermi pockets and quantum oscillations of the Hall coefficient in high-temperature superconductors. *Proc. Natl. Acad. Sci. U.S.A.*, 105(8835), 2008. 19, 20

[41] M. R. Norman, H. Ding, M. Randeria, J. C. Campuzano, T. Yokoya, T. Takeuchi, T. Takahashi, T. Mochiku, K. Kadowaki, P. Guptasarma, and D. G. Hinks. Destruction of the fermi surface in underdoped high-T_c superconductors. *Nature*, 157(392), 1998. 19, 20

[42] Hussain Z. Damascelli A. and Shen Z.-X. Angle-resolved photoemission studies of the cuprate superconductors. *Rev. Mod. Phys.*, 75(473), 2003. 19, 20

[43] Norman M. R. Campuzano J. C. and Randeria M. *The Physics of superconductors*, volume II. Springer, 2004. 19, 20

[44] M. A. Hossain, J. D. F. Mottershead, A. Bostwick, J. L. McChesney, E. Rotenberg, R. Liang, W. N. Hardy, G. A. Sawatzky, I. S. Elfimov, D. A. Bonn, and A. Damascelli. *In situ* doping control of the surface of high-temperature superconductors. *Nature Phys.*, 4(527), 2008. 19, 20, 44

[45] S. E. Sebastian, N. Harrison, E. Palm, T. P. Murphy, C. H. Mielke, R. Liang, D. A. Bonn, W. N. Hardy, and G. G. Lonzarich. A multi-component Fermi surface in the vortex state of an underdoped high-T_c superconductor. *Nature*, 454(200), 2008. 20, 28, 32

[46] Andrew J. Millis and M. R. Norman. Antiphase stripe order as the origin of electron pockets observed in 1/8-hole-doped cuprates. *Phys. Rev. B*, 76(220503), 2007. 20

[47] Chen W.-Q., Yang K.-Y., Rice T. M., and Zhang F. C. Quantum Oscillations in Magnetic Field Induced Antiferromagnetic Phase of Underdoped Cuprates : Application to Ortho-II $YBa_2Cu_3O_{6.5}$. *EPL*, 82(17004), 2008. 20, 22, 39

[48] N. Harrison, R. D. McDonald, and J. Singleton. Cuprate Fermi Orbits and Fermi Arcs: The Effect of Short-Range Antiferromagnetic Order. *Phys. Rev. Lett.*, 99(206406), 2007. 20, 44

[49] B. Kyung, S. S. Kancharla, D. Sénéchal, A.-M. S. Tremblay, M. Civelli, and G. Kotliar. Pseudogap induced by short-range spin correlations in a doped Mott insulator. *Phys. Rev. B*, 73(165114), 2006. 20

[50] E. Kuchinskii and M. Sadovskii. Reconstruction of the Fermi surface in the pseudogap state of cuprates. *JETP Letters*, 88(192), 2008. 20, 44

[51] L. Hozoi and M. S. Laad. Quasiparticle Bands in Cuprates by Quantum-Chemical Methods: Towards an *Ab Initio* Description of Strong Electron Correlations. *Phys. Rev. Lett.*, 99(256404), 2007. 20

[52] Hugo Keller, Annette Bussmann-Holder, and K. Alex Müller. Jahn-Teller physics and high-Tc superconductivity. *Materials Today*, 11(38), 2008. 20, 22, 44, 45

[53] Bussmann-Holder A. and Keller H. *Polarons in Advanced Materials*, volume 103. Springer Series in Materials Science, 2007. 20, 22, 44, 45

[54] Niedermayer Ch., Bernhard C., Blasius T., Golnik A., Moodenbaugh A., and Budnick J. I. Common phase diagram for antiferromagnetism in $La_{2-x}Sr_xCuO_4$ and $Y_{1-x}Ca_xBa_2Cu_3O_6$ as seen by muon spin rotation. *Phys. Rev. Lett.*, 80(3843), 1998. 20, 44, 45

[55] Sanna S., Allodi G., Concas G., Hillier A. D., and Renzi R. De. Nanoscopic coexistence of magnetism and superconductivity in $YBa_2Cu_3O_{6+x}$ detected by muon spin rotation. *Phys. Rev. Lett.*, 93(207001), 2004. 20

[56] V. Hinkov, S. Pailhes, P. Bourges, Y. Sidis, A. Ivanov, A. Kulakov, C. T. Lin, D. P. Chen, C. Bernhard, and B. Keimer. Two-dimensional geometry of spin excitations in the high-transition-temperature superconductor $YBa_2Cu_3O_{6+x}$. *Nature*, 430(650), 2004. 20

[57] Y. Sidis, C. Ulrich, P. Bourges, C. Bernhard, C. Niedermayer, L. P. Regnault, N. H. Andersen, and B. Keimer. Antiferromagnetic Ordering in Superconducting $YBa_2Cu_3O_{6+x}$. *Phys. Rev. Lett.*, 86(4100), 2001. 20

[58] B. Fauqué, Y. Sidis, V. Hinkov, S. Pailhès, C. T. Lin, X. Chaud, and P. Bourges. Magnetic Order in the Pseudogap Phase of High-T_c Superconductors. *Phys. Rev. Lett.*, 96(197001), 2006. 20

[59] Nicolas Doiron-Leyraud, Mike Sutherland, S. Y. Li, Louis Taillefer, Ruixing Liang, D. A. Bonn, and W. N. Hardy. Onset of a Boson Mode at the Superconducting Critical Point of Underdoped $YBa_2Cu_3O_y$. *Phys. Rev. Lett.*, 97(207001), 2006. 20

[60] B. G. Levi. Quantum oscillations finally seen in high-temperature superconductors. *Physics Today*, 60(26), 2007. 21

[61] B. Lake, H. M. Ronnow, N. B. Christensen, G. Aeppli, K. Lefmann, D. F. McMorrow, P. Vorderwisch, P. Smeibidl, N. Mangkorntong, T. Sasagawa, M. Nohara, H. Takagi, and T. E. Mason. Antiferromagnetic order induced by an applied magnetic field in a high-temperature superconductor. *Nature*, 415(299), 2002. 21

[62] A. Carrington and E. A. Yelland. Band-structure calculations of Fermi-surface pockets in *ortho*-ii $YBa_2Cu_3O_{6.5}$. *Phys. Rev. B*, 76(140508), 2007. 21, 24, 26, 33

[63] V. I. Anisimov, M. A. Korotin, J. Zaanen, and O. K. Andersen. Spin bags, polarons, and impurity potentials in $La_{2-x}Sr_xCuO_4$ from first principles. *Phys. Rev. Lett.*, 68(345), 1992. 22, 23, 42, 44, 45

[64] Alessio Filippetti and Vincenzo Fiorentini. Magnetic Ordering in CuO from First Principles: A Cuprate Antiferromagnet with Fully Three-Dimensional Exchange Interactions. *Phys. Rev. Lett.*, 95(086405), 2005. 22, 33, 46, 48

[65] Alessio Filippetti and Vincenzo Fiorentini. Double-exchange driven ferromagnetic metal-paramagnetic insulator transition in Mn-doped CuO. *Phys. Rev. B*, 74(220401), 2006. 22, 33, 49

[66] Alessio Filippetti and Vincenzo Fiorentini. Magnetic Ordering under Strain and Spin-Peierls Dimerization $GeCuO_3$. *Phys. Rev. Lett.*, 98(196403), 2007. 22, 33, 49

[67] A. Filippetti and V. Fiorentini. Metal-insulator transitions and singlet polarons in one-dimensional $Ca_{2+x}Y_{2-x}Cu_5O_{10}$. *Phys. Rev. B*, 77(235124), 2008. 22, 33, 49

[68] Alessio Filippetti, Giorgia M. Lopez, Mauro Mantega, and Vincenzo Fiorentini. Chain metallicity and competition between paramagnetism and antiferromagnetism in underdoped $YBa_2Cu_3O_{6+x}$: A first principles description. *Phys. Rev. B*, 78(233103), 2008. 22, 23, 33, 36, 49

[69] Alessio Filippetti and Vincenzo Fiorentini. Self-interaction-free density-functional band theory for magnetic cuprates. *Journal of Magnetism and Magnetic Materials*, 310(1648 - 1650), 2007. 22, 23, 33

[70] G. Kresse and J. Hafner. *Ab initio* molecular dynamics for liquid metals. *Phys. Rev. B*, 47(558–561), 1993. 22

[71] G. Kresse and J. Furthmüller. Efficiency of *ab-initio* total energy calculations for metals and semiconductors using a plane-wave basis set. *Computational Materials Science*, 6(15 - 50), 1996. 22, 70

[72] John P. Perdew, J. A. Chevary, S. H. Vosko, Koblar A. Jackson, Mark R. Pederson, D. J. Singh, and Carlos Fiolhais. Atoms, molecules, solids, and surfaces: Applications of the generalized gradient approximation for exchange and correlation. *Phys. Rev. B*, 46(6671–6687), 1992. 22

[73] J. M. Shi, F. M. Peeters, G. Q. Hai, and J. T. Devreese. Erratum: Donor transition energy in GaAs superlattices in a magnetic field along the growth axis. *Phys. Rev. B*, 48(4978–4978), 1993. 22

[74] P. E. Blöchl. Projector augmented-wave method. *Phys. Rev. B*, 50(17953–17979), 1994. 22

[75] G. Kresse and D. Joubert. From ultrasoft pseudopotentials to the projector augmented-wave method. *Phys. Rev. B*, 59(1758–1775), 1999. 22

[76] D. Vanderbilt. Soft self-consistent pseudopotentials in a generalized eigenvalue formalism. *Phys. Rev. B*, 41(R7892), 1990. 22, 23, 46, 56, 68, 131

[77] Hendrik J. Monkhorst and James D. Pack. Special points for brillouin-zone integrations. *Phys. Rev. B*, 13(5188–5192), 1976. 22

[78] J. Grybos, D. Hohlwein, T. Zeiske, R. Sonntag, F. Kubanek, K. Eichhorn, and T. Wolf. Atomic displacements in the *ortho*-II phase of $YBa_2Cu_3O_{6.5}$ by synchrotron X-ray diffraction. *Physica C*, 220(138), 1994. 23

[79] J. Grybos, M. Wabia, N. Guskos, and J. Typek. Atomic displacements in the *ortho*-II phase of $YBa_2Cu_3O_{6.5}$ by synchrotron X-ray diffraction. *Physica C*, 34(121), 2001. 23

[80] Anton and Kokalj. Xcrysden a new program for displaying crystalline structures and electron densities. *Journal of Molecular Graphics and Modelling*, 17(176 - 179), 1999. 23

[81] Anton and Kokalj. Computer graphics and graphical user interfaces as tools in simulations of matter at the atomic scale. *Computational Materials Science*, 28(155 - 168), 2003. 23

[82] S.L. Dudarev, G.A. Botton, S.Y. Savrasov, C.J. Humphreys, and A.P. Sutton. Electron-energy-loss spectra and the structural stability of nickel oxide: an LSDA+U study. *Phys. Rev. B*, 57(1505), 1998. 23, 25, 68

[83] V. I. Anisimov, M. A. Korotin, A. S. Mylnikova, A. V. Kozhevnikov, Dm. M. Korotin, and J. Lorenzana. Computation of stripes in cuprates within the LDA+U method. *Phys. Rev. B*, 70(172501), 2004. 23

[84] K. Yonemitsu, A. R. Bishop, and J. Lorenzana. Sensitivity of doping states in the copper oxides to electron-lattice coupling. *Phys. Rev. Lett.*, 69(965–968), 1992. 23

[85] E. Bascones, T. M. Rice, A. O. Shorikov, A. V. Lukoyanov, and V. I. Anisimov. Optical conductivity of ortho-ii $YBa_2Cu_3O_{6.5}$. *Phys. Rev. B*, 71(012505), 2005. 24

[86] A. P. Mackenzie, S. R. Julian, A. J. Diver, G. J. McMullan, M. P. Ray, G. G. Lonzarich, Y. Maeno, S. Nishizaki, and T. Fujita. Quantum oscillations in the

layered perovskite superconductor Sr_2RuO_4. *Phys. Rev. Lett.*, 76(3786–3789), 1996. 26

[87] A. Carrington, P. J. Meeson, J. R. Cooper, L. Balicas, N. E. Hussey, E. A. Yelland, S. Lee, A. Yamamoto, S. Tajima, S. M. Kazakov, and J. Karpinski. Determination of the Fermi Surface of MgB_2 by the de Haas˘van Alphen effect. *Phys. Rev. Lett.*, 91(037003), 2003. 26

[88] A. Carrington, E.A. Yelland, J.D. Fletcher, and J.R. Cooper. de Haas van Alphen effect investigations of the electronic structure of pure and aluminum-doped MgB_2. *Physica C: Superconductivity*, 456(92 - 101), 2007. 26

[89] I. S. Elfimov, G. A. Sawatzky, and A. Damascelli. Theory of Fermi-surface pockets and correlation effects in underdoped $YBa_2Cu_3O_{6.5}$. *Phys. Rev. B*, 77(060504), 2008. 26

[90] A. F. Bangura, J. D. Fletcher, A. Carrington, J. Levallois, M. Nardone, B. Vignolle, P. J. Heard, N. Doiron-Leyraud, D. LeBoeuf, L. Taillefer, S. Adachi, C. Proust, and N. E. Hussey. Small Fermi Surface Pockets in Underdoped High Temperature Superconductors: Observation of Shubnikov˘de Haas Oscillations in $YBa_2Cu_4O_8$. *Phys. Rev. Lett.*, 100(047004), 2008. 33

[91] Claudia Ambrosch-Draxl, Peter Blaha, and Karlheinz Schwarz. Electronic structure and electric-field gradients for $YBa_2Cu_4O_8$ from density-functional calculations. *Phys. Rev. B*, 44(5141–5147), 1991. 33

[92] Andrea Damascelli, Zahid Hussain, and Zhi-Xun Shen. Angle-resolved photoemission studies of the cuprate superconductors. *Rev. Mod. Phys.*, 473–541(75), 2003. 33

[93] Igor Dzyaloshinskii. Some consequences of the Luttinger theorem: The Luttinger surfaces in non-Fermi liquids and Mott insulators. *Phys. Rev. B*, 68(085113), 2003. 39

[94] B. Lake, G. Aeppli, K. Clausen, D. McMorrow, K. Lefmann, N. Hussey, N. Mangkorntong, M. Nohara, H. Takagi, and T. Masonand andA. Schroder. Spins in the Vortices of a High-Temperature Superconductor. *Science*, 291(1759), 2001. 39

[95] F. C. Zhang and T. M. Rice. Effective Hamiltonian for the superconducting Cu oxides. *Phys. Rev. B*, 37(3759), 1988. 40

[96] M. R. Norman, A. Kanigel, M. Randeria, U. Chatterjee, and J. C. Campuzano. Modeling the Fermi arc in underdoped cuprates. *Phys. Rev. B*, 76(174501), 2007. 44

[97] D. Haug, V. Hinkov, A. Suchaneck, D. S. Inosov, N. B. Christensen, Ch. Niedermayer, P. Bourges, Y. Sidis, J. T. Park, A. Ivanov, C. T. Lin, J. Mesot, and B. Keimer. Magnetic-field-enhanced incommensurate magnetic order in the underdoped high-temperature superconductor $YBa_2Cu_3O_{6.45}$. *Phys. Rev. Lett.*, 103(017001), 2009. 45

[98] Suchitra E. Sebastian, N. Harrison, P. A. Goddard, M. M. Altarawneh, C. H. Mielke, Ruixing Liang, D. A. Bonn, W. N. Hardy, O. K. Andersen, and G. G. Lonzarich. Compensated electron and hole pockets in an underdoped high-T_c superconductor. *Phys. Rev. B*, 81(214524), 2010. 45

[99] J. Meng, G. Liu, W. Zhang, L. Zhao, H. Liu, X. Jia, D. Mu, S. Liu, X. Dong, J. Zhang, W. Lu, G. Wang, Y. Zhou, Y. Zhu, X. Wang, Z. Xu, C. Chen, and X. J. Zhou. Coexistence of Fermi arcs and Fermi pockets in a high-T_c copper oxide superconductor. *Phys. Rev. B*, 462(335), 2009. 45

[100] Giovanni Peralta, Danilo Puggioni, Alessio Filippetti, and Vincenzo Fiorentini. Jahn-Teller stabilization of magnetic and orbital ordering in rocksalt CuO. *Phys. Rev. B*, 80(140408), 2009. 46, 109

[101] B. X. Yang, J. M. Tranquada, and G. Shirane. Neutron scattering studies of the magnetic structure of cupric oxide. *Phys. Rev. B*, 38(174), 1988. 46

[102] B. X. Yang, T. R. Thurston, J. M. Tranquada, and G. Shirane. Magnetic neutron scattering study of single-crystal cupric oxide. *Phys. Rev. B*, 39:4343, 1989. 46

[103] See the review of the method and of recent results in A. Filippetti and V. Fiorentini, Eur. Phys. J. B **71**, 139 (2009). 46, 69

[104] We use a plane wave basis with cutoff 40 Ryd, ultrasoft pseudopotentials,[76] and fine k-points meshes up to (8,8,8). 46

[105] M. T. Yin and Marvin L. Cohen. Theory of static structural properties, crystal stability, and phase transformations: Application to Si and Ge. *Phys. Rev. B*, 26(5668), 1982. 49

[106] Nathascia Lampis, Cesare Franchini, Guido Satta, Alessandra Geddo-Lehmann, and Sandro Massidda. Electronic structure of $PbFe_{1/2}Ta_{1/2}O_3$: crystallographic ordering and magnetic properties. *Phys. Rev. B*, 69(064412), 2004. 52

[107] P.W. Anderson. New approach to the theory of superexchange interactions. *Phys. Rev.*, 115(2), 1959. 52, 67, 80, 90

[108] Chi-Yuan Weng, Robert B. Griffiths, and Michael E. Fisher. Critical Temperatures of Anisotropic Ising Lattices. I. Lower Bounds. *Phys. Rev.*, 162(475), 1967. 52

[109] Michael E. Fisher. Critical Temperatures of Anisotropic Ising Lattices. II. General Upper Bounds. *Phys. Rev.*, 162(480), 1967. 52

[110] M. A. Yurishchev. Anisotropic simple-cubic Ising lattice: extended phenomenological renormalization-group treatment. *arXiv:cond-mat/0312555v1*, 2003. 52

[111] P. M. Grant. Electronic properties of rocksalt copper monoxide: a proxy structure for high temperature superconductivity. *J. Phys.: Conf. Ser.*, 129(012042), 2008. 53

[112] Xing-Qiu Chen, C. L. Fu, C. Franchini, and R. Podloucky. Hybrid density-functional calculation of the electronic and magnetic structures of tetragonal CuO. *Phys. Rev. B*, 80(094527), 2009. 54

[113] G. Khaliullin and S. Okamoto. Quantum behavior of orbitals in ferromagnetic titanates: Novel orderings and excitations. *Phys. Rev. Lett.*, 89(167201), 2002. 56

[114] M. Tsubota, F. Iga, T. Takabatake, N. Kikugawa, T. Suzuki, I. Oguro, H. Kawanaka, and H. Bando. Low-field magnetic anisotropy in Mott-insulating ferromagnet $Y_{1-x}Ca_xTiO_3$ ($x \leq 0.1$). *Physica B*, 281-282(622), 2000. 56

[115] H. Nakao, Y. Wakabayashi, T. Kiyama, Y. Murakami, M. V. Zimmermann, J. P. Hill, D. Gibbs, S. Ishihara, Y. Taguchi, and Y. Tokura. Quantitative determination of the atomic scattering tensor in orbitally ordered $YTiO_3$ by using a resonant x-ray scattering technique. *Phys. Rev. B*, 66(184419), 2002. 56

[116] M. Mochizuki and M. Imada. Orbital-spin structure and lattice coupling in $RTiO_3$ where R=La, Pr, Nd, and Sm. *Phys. Rev. Lett.*, 91(167203), 2003. 56, 62

[117] M. Cwikand T. Lorenz, J. Baier, R. Müller, G. André, F. Bourée, F. Lichtenberg, A. Freimuth, R. Schmitz, E. Müller-Hartmann, and M. Braden. Crystal and magnetic structure of $LaTiO_3$: Evidence for nondegenerate t_{2g} orbitals. *Phys. Rev. B*, 68(060401(R)), 2003. 56, 64

[118] B. Keimer, D. Casa, A. Ivanov, J. W. Lynn, M. v. Zimmermann, J. P. Hill, D. Gibbs, Y. Taguchi, and Y. Tokura. Spin dynamics and orbital state in $LaTiO_3$. *Phys. Rev. Lett.*, 85(3946), 2000. 56

[119] T. Kiyama and M. Itoh. Presence of 3d quadrupole moment in $LaTiO_3$ studied by ^{47,49}Ti NMR. *Phys. Rev. Lett.*, 91(167202), 2003. 56, 62

[120] G. Khaliullin and S. Maekawa. Orbital liquid in three-dimensional Mott insulator: $LaTiO_3$. *Phys. Rev. Lett.*, 85(3950), 2000. 56

[121] L. Craco, M. S. Laad, S. Leoni, and E. Müller-Hartmann. Hidden orbital fluctuations in the solid solution $Y_{1-x}La_xTiO_3$ (x<0.2). *Phys. Rev. B*, 74(155128), 2006. 56

[122] M. W. Haverkort *et al.* Determination of the orbital moment and crystal-field splitting in $LaTiO_3$. *Phys. Rev. Lett.*, 94(056401), 2005. 56

[123] J. Hemberger *et al.* Evidence for Jahn-Teller distortions at the antiferromagnetic transition in $LaTiO_3$. *Phys. Rev. Lett.*, 91(066403), 2003. 56

[124] P. Lunkenheimer, T. Rudolf, J. Hemberger, A. Pimenov, S. Tachos, F. Lichtenberg, and A. Loidl. Dielectric properties and dynamical conductivity of $LaTiO_3$: From dc to optical frequencies. *Phys. Rev. B*, 68(245108), 2003. 56, 65

[125] H. Fujitani and S. Asano. Full-potential band calculations on $YTiO_3$ with a distorted perovskite structure. *Phys. Rev. B*, 51(2098), 1995. 56

[126] H. Sawada and K. Terakura. Orbital and magnetic orderings in localized t_{2g} systems, $YTiO_3$ and YVO_3: Comparison with a more itinerant e_g system $LaMnO_3$. *Phys. Rev. B*, 58(6831), 1998. 56, 62

[127] S. V. Streltsov, A. S. Mylnikova, A. O. Shorikov, Z. V. Pchelkina, D. I. Khomskii, and V. I. Anisimov. Crystal-field splitting for low symmetry systems in *ab initio* calculations. *Phys. Rev. B*, 71(257114), 2005. 56, 65

[128] E. Pavarini, S. Biermann, A. Poteryaev, A. I. Lichtenstein, A. Georges, and O. K. Andersen. Mott transition and suppression of orbital fluctuations in orthorhombic $3d^1$ perovskites. *Phys. Rev. Lett.*, 92(176403), 2004. 56, 59

[129] I. V. Solovyev. Lattice distortion and magnetism of $3d - t_{2g}$ perovskite oxides. *Phys. Rev. B*, 74(054412), 2006. 56

[130] I. A. Nekrasov, N. Blümer K. Held, A. I. Poteryaev, V. I. Anisimov, and D. Vollhardt. Calculation of photoemission spectra of the doped Mott insulator $La_{1-x}Sr_xTiO_3$ using LDA+DMFT(QMC). *Eur. Phys. J. B*, 18(55), 2000. 56

[131] For a 45^o rotation in the (x,y) plane $|xy\rangle \rightarrow |x^2 - y^2\rangle$, $|xz\rangle \rightarrow (|xz\rangle + |yz\rangle)/\sqrt{2}$, $|yz\rangle \rightarrow (|yz\rangle$ - $|xz\rangle)/\sqrt{2}$. 57

[132] F. Iga, M. Tsubota, M. Sawada, H. B. Huang, S. Kura, M. Takemura, K. Yaji, M. Nagira, A. Kimura, T. Jo, T. Takabatake, H. Namatame, and M. Taniguchi. Determination of the orbital polarization in $YTiO_3$ by using soft x-ray linear dichroism. *Phys. Rev. Lett.*, 93(257207), 2004. 59, 134

[133] Notice that we use a different reference configuration: in ref.[132] they assume a local cubic reference system where z change according to Ti, so to be always parallel to the longer Ti-O bond. see our structural analysis later on. 59

[134] T. Archer, C. D. Pemmaraju, S. Sanvito, C. Franchini, J. He, A. Filippetti, P. Delugas, D. Puggioni, V. Fiorentini, R. Tiwari, and P. Majumdar. Exchange

interactions and magnetic phases of transition metal oxides: Benchmarking advanced *ab initio* methods. *Phys. Rev. B*, 84(115114), 2011. 67, 107

[135] I. V. Solovyev and K. Terakura. Effective single-particle potentials for MnO in light of interatomic magnetic interactions: Existing theories and perspectives. *Phys. Rev. B*, 58(15496), 1998. 67, 68, 69, 83, 86

[136] X. Wan, Q. Yin, and S. Y. Savrasov. Calculation of magnetic exchange interactions in Mott-Hubbard systems. *Phys. Rev. Lett.*, 97(266403), 2006. 67, 89, 90

[137] T. Kotani and M. van Shilfgaarde. Spin wave dispersion based on the quasiparticle self-consistent GW method: NiO, MnO and α-MnAs. *J. Phys. Condensed Matter*, 20(295214), 2008. 67, 68, 83, 86

[138] Z. Fang, K. Terakura, H. Sawada, T. Miyazaki, and I. Solovyev. Inverse versus normal NiAs structures as high-pressure phases of FeO and MnO. *Phys. Rev. Lett.*, 81(1027–1030), 1998. 68

[139] Zhong Fang, Igor V. Solovyev, Hideaki Sawada, and Kiyoyuki Terakura. First-principles study on electronic structures and phase stability of MnO and FeO under high pressure. *Phys. Rev. B*, 59(762–774), 1999. 68

[140] A. Rohrbach, J. Hafner, and G. Kresse. Molecular adsorption on the surface of strongly correlated transition-metal oxides: A case study for CO/NiO(100). *Phys. Rev. B*, 69(075413), 2004. 68

[141] Pask, J. E., Singh, D. J., Mazin, I. I., Hellberg C. S., and J. Kortus. Structural, electronic, and magnetic properties of MnO. *Phys. Rev. B*, 64(024403), 2001. 68

[142] Zhang Wei-Bing, Hu Yu-Lin, Han Ke-Li, and Tang Bi-Yu. Pressure dependence of exchange interactions in NiO. *Phys. Rev. B*, 74(054421), 2006. 68, 83, 86

[143] V. Bayer, C. Franchini, and R. Podloucky. *Ab initio* study of the structural, electronic, and magnetic properties of MnO(100) and MnO(110). *Phys. Rev. B*, 75(035404), 2007. 68

[144] F. Aryasetiawan and O. Gunnarsson. Electronic structure of NiO in the GW approximation. *Phys. Rev. Lett.*, 74(3221–3224), 1995. 68

[145] S. Massidda, A. Continenza, M. Posternak, and A. Baldereschi. Quasiparticle energy bands of transition-metal oxides within a model GW scheme. *Phys. Rev. B*, 55(13494–13502), 1997. 68

[146] D. Ködderitzsch, W. Hergert, W. M. Temmerman, Z. Szotek, A. Ernst, and H. Winter. Exchange interactions in NiO and at the NiO(100) surface. *Phys. Rev. B*, 66(064434), 2002. 68, 84, 86

[147] Guntram Fischer, Markus Däne, Arthur Ernst, Patrick Bruno, Martin Lüders, Zdzislawa Szotek, Walter Temmerman, and Wolfram Hergert. Exchange coupling in transition metal monoxides: Electronic structure calculations. *Phys. Rev. B*, 80(014408), 2009. 68, 71, 84, 86, 89, 90

[148] M. Däne, M. Lüders, A. Ernst, D. Ködderitzsch, W.M. Temmerman, Z. Szotek, and W. Hergert. Self-interaction correction in multiple scattering theory: application to transition metal oxides. *J. Phys.: Condens. Matter*, 21(045604), 2009. 68, 84

[149] I.D. Huges, M. Däne, A. Ernst, W. Hergert, M. Lüders, J. B. Stounton, Z. Szotek, and W. Temmermann. Onset of magnetic order in strongly-correlated systems from *ab initio* electronic structure calculations: application to transition metal oxides. *New Journal of Physics*, 10(063010), 2008. 68, 84

[150] M. D. Towler, N. L. Allan, N. M. Harrison, V. R. Saunders, W. C. Mackrodt, and E. Aprà. *Ab initio* study of MnO and NiO. *Phys. Rev. B*, 50(5041–5054), 1994. 68

[151] Thomas Bredow and Andrea R. Gerson. Effect of exchange and correlation on bulk properties of MgO, NiO, and CoO. *Phys. Rev. B*, 61(5194–5201), 2000. 68

[152] C. Franchini, V. Bayer, R. Podloucky, J. Paier, and G. Kresse. Density functional theory study of MnO by a hybrid functional approach. *Phys. Rev. B*, 72(045132), 2005. 68, 73, 86

[153] Ibério de P. R. Moreira, Francesc Illas, and Richard L. Martin. Effect of Fock exchange on the electronic structure and magnetic coupling in NiO. *Phys. Rev. B*, 65(155102), 2002. 68, 83, 84, 86

[154] Xiaobing Feng. Electronic structure of MnO and CoO from the B3LYP hybrid density functional method. *Phys. Rev. B*, 69(155107), 2004. 68, 86

[155] Xiao-Bing Feng and N. M. Harrison. Metal-insulator and magnetic transition of NiO at high pressures. *Phys. Rev. B*, 69(035114), 2004. 68, 86

[156] Fabien Tran, Peter Blaha, Karlheinz Schwarz, and Pavel Novák. Hybrid exchange-correlation energy functionals for strongly correlated electrons: Applications to transition-metal monoxides. *Phys. Rev. B*, 74(155108), 2006. 68

[157] Xing-Qiu Chen, C. L. Fu, C. Franchini, and R. Podloucky. Hybrid density-functional calculation of the electronic and magnetic structures of tetragonal CuO. *Phys. Rev. B*, 80(094527), 2009. 68

[158] Deepa Kasinathan, J. Kuneš, K. Koepernik, Cristian V. Diaconu, Richard L. Martin, Ionuţ D. Prodan, Gustavo E. Scuseria, Nicola Spaldin, L. Petit, T. C. Schulthess, and W. E. Pickett. Mott transition of MnO under pressure: A comparison of correlated band theories. *Phys. Rev. B*, 74(195110), 2006. 68

[159] R. Cohen, I. Mazin, and I.G. Isaak. Magnetic collapse in transition metal oxides at high pressure: Implications for the earth. *Science*, 275(654), 1997. 68, 76

[160] A. Mattila, J-P. Rueff, J. Badro, G. Vankó, and A. Shukla. Metal-ligand interplay in strongly correlated oxides: A parametrized phase diagram for pressure-induced spin transitions. *Phys. Rev. Lett.*, 98(196404), 2007. 68

[161] J. Kunes, A. V. Lukoyanov, V. I. Anisimov, R. T. Scalettar, and W. E. Pickett. Collapse of magnetic moment drives the mott transition in mno. *Nature Materials*, 7(198), 2008. 68

[162] J. Heyd, G. Scuseria, and M. Ernzerhof. Hybrid functionals based on a screened Coulomb potential. *J. Chem. Phys.*, 118(8207), 2003. 68, 70, 138

[163] J. Heyd, G. Scuseria, and M. Ernzerhof. Erratum: ”hybrid functionals based on a screened Coulomb potential” [J. Chem. Phys. 118, 8207 (2003)][162]. *J. Chem. Phys.*, 124(219906), 2006. 68, 70

[164] Aliaksandr V. Krukau, Oleg A. Vydrov, Artur F. Izmaylov, and Gustavo E. Scuseria. Influence of the exchange screening parameter on the performance of screened hybrid functionals. *J. Chem. Phys.*, 125(224106), 2006. 68, 70

[165] John P. Perdew, Kieron Burke, and Matthias Ernzerhof. Generalized gradient approximation made simple. *Phys. Rev. Lett.*, 77(3865–3868), 1996. 68, 70

[166] J. Zaanen, G. A. Sawatzky, and J. W. Allen. Band gaps and electronic structure of transition-metal compounds. *Phys. Rev. Lett.*, 55(418–421), 1985. 68

[167] I.A. Nekrasov, M.A. Korotin, and F. V.I. Anisimov. Coulomb interaction in oxygen *p*-shell in LDA+U method and its influence on calculated spectral and magnetic properties of transition metal oxides. *arXiv:0009107v1*, 2000. 69

[168] A. D. Becke. A new mixing of HartreeFock and local density-functional theories. *J. Chem. Phys.*, 98(1372), 1993. 69

[169] G. Kresse and J. Hafner. *Ab initio* molecular dynamics for open-shell transition metals. *Phys. Rev. B*, 48(13115–13118), 1993. 70

[170] Aliaksandr V. Krukau, Oleg A. Vydrov, Artur F. Izmaylov, and Gustavo E. Scuseria. Influence of the exchange screening parameter on the performance of screened hybrid functionals. *J. of Chem. Phys.*, 125(224106), 2006. 70

[171] M. Ernzerhof and G. E. Scuseria. Assessment of the PerdewBurkeErnzerhof exchange-correlation functional. *J. of Chem. Phys.*, 110(5029), 1999. 70

[172] C. Adamo and V. Barone. Toward reliable density functional methods without adjustable parameters: The PBE0 model. *J. of Chem. Phys.*, 110(6158), 1999. 70

[173] Francis Birch. Finite elastic strain of cubic crystals. *Phys. Rev.*, 71(809–824), 1947. 70

[174] M. T. Hutchings and E. J. Samuelsen. Measurement of Spin-Wave dispersion in NiO by inelastic neutron scattering and its relation to magnetic properties. *Phys. Rev. B*, 6(3447–3461), 1972. 71, 73, 83, 86, 89

[175] S. Sasaki, K. Fujino, Y. Takeguchi, and R. Sadanaga. Crystal physics, diffraction, theoretical and general crystallography. *Acta Crystallogr. A*, 36(904), 1980. 85

[176] Y. Noguchi, K. Kusaba, K. Fukuoka, and Y. Syono. Shock-induced phase transition of MnO around 90GPa. *Geophys. Res. Lett.*, 23(1469), 1996. 85

[177] R. Jeanloz and A. Rudy. Static compression of MnO manganosite to 60 GPa. *J. Geophys. Res.*, 92(11433), 1987. 85

[178] N.G. Schmahl, J. Barthel, and G.F. Eikerling. Röntgenographische untersuchungen an den systemen MgOCuO und NiO. *Z. Anorg. Allg. Chem.*, 332(230), 1964. 85

[179] E. Huang, K. Jy, and S.-C. Yu. Bulk modulus of nio. *J. Geophys. Soc. China*, 37(7), 1994. 85

[180] M. Marsman, J. Paier, A. Stroppa, and G. Kresse. Hybrid functionals applied to extended systems. *J. Phys.: Condens. Matter*, 20(064201), 2008. 73

[181] C. Franchini, R. Podloucky, J. Paier, M. Marsman, and G. Kresse. Ground-state properties of multivalent manganese oxides: Density functional and hybrid density functional calculations. *Phys. Rev. B*, 75(195128), 2007. 73

[182] T. M. Schuler, D. L. Ederer, S. Itza-Ortiz, G. T. Woods, T. A. Callcott, and J. C. Woicik. Character of the insulating state in NiO: A mixture of charge-transfer and Mott-Hubbard character. *Phys. Rev. B*, 71(115113), 2005. 80

[183] Abhay Shukla, Jean-Pascal Rueff, James Badro, Gyorgy Vanko, Aleksi Mattila, F. M. F de Groot, and Francesco Sette. Charge transfer at very high pressure in NiO. *Phys. Rev. B*, 67(081101), 2003. 80

[184] J. Kuneš, V. I. Anisimov, S. L. Skornyakov, A. V. Lukoyanov, and D. Vollhardt. NiO: Correlated band structure of a charge-transfer insulator. *Phys. Rev. Lett.*, 99(156404), 2007. 80

[185] John B. Goodenough. Theory of the role of covalence in the perovskite-type manganites [La,M(II)]MnO_3. *Phys. Rev.*, 100(564–573), 1955. 80

[186] J. Kanamori. Superexchange interaction and symmetry properties of electron orbitals. *J. Phys. Chem. Solids*, 10(87), 1959. 80

[187] M. Kohgi, Y. Ishikawa, and Y. Endoh. Inelastic neutron scattering study of spin waves in MnO. *Solid State Commun.*, 11(391), 1972. 83, 86, 89

[188] G. Pepy. Spin waves in MnO; from 4k to temperatures close to T_N. *J. Phys. Chem. Solids*, 35(433), 1974. 83, 86, 89

[189] M. E. Lines and E. D. Jones. Antiferromagnetism in the face-centered cubic lattice. ii. magnetic properties of MnO. *Phys. Rev.*, 139(A1313–A1327), 1965. 83, 86, 89

[190] R. Shanker and R. A. Singh. Analysis of the exchange parameters and magnetic properties of NiO. *Phys. Rev. B*, 7(5000–5005), 1973. 83, 86, 89

[191] A. I. Liechtenstein, M. I. Katsnelson, V. P. Antropov, and V. A. Gubanov. Local spin density functional approach to the theory of exchange interactions in ferromagnetic metals and alloys. *J. Magn. Magn. Mater.*, 67(65), 1987. 83

[192] G. Vignale and Mark Rasolt. Density-functional theory in strong magnetic fields. *Phys. Rev. Lett.*, 59(2360–2363), 1987. 83

[193] G. Vignale and Mark Rasolt. Current- and spin-density-functional theory for inhomogeneous electronic systems in strong magnetic fields. *Phys. Rev. B*, 37(10685–10696), 1988. 83

[194] Mark Rasolt and G. Vignale. Self-induced effective gauge fields in the copper-oxygen plane of high-T_c perovskites: A lattice and a continuum formulation. *Phys. Rev. Lett.*, 65(1498–1501), 1990. 83

[195] S. Y. Savrasov. Linear response calculations of spin fluctuations. *Phys. Rev. Lett.*, 81(2570–2573), 1998. 83

[196] K. Karlsson and F. Aryasetiawan. Spin-wave excitation spectra of nickel and iron. *Phys. Rev. B*, 62(3006–3009), 2000. 83

[197] R. Shanker and R. A. Singh. *A Guide to Monte Carlo Simulations in Statistical Physics*. Cambridge University Press, Cambridge, England, 2000. 87

[198] Roth W. L. Magnetic structures of MnO, FeO, CoO, and NiO. *Phys. Rev.*, 110(1333–1341), 1958. 89

[199] C. G. Shull, W. A. Strauser, and E. O. Wollan. Neutron diffraction by paramagnetic and antiferromagnetic substances. *Phys. Rev.*, 83(333–345), 1951. 89

[200] A proper comparison with our data cannot be drawn as the employed Heisenberg Hamiltonian and the J's are not reported. 90

[201] C. L. Bull, D. Gleeson, and K. S. Knight. Determination of B-site ordering and structural transformations in the mixed transition metal perovskites La_2CoMnO_6 and La_2NiMnO_6. *J. Phys. Condens. Matter*, 15(4927), 2003. 93, 94

[202] Kichizo Asai, Hisashi Sekizawa, and Shuichi Iida. Magnetization Measurements and ^{55}Mn NMR Studies of $LaNi_{0.5}Mn_{0.5}O_3$. *Journal of the Physical Society of Japan*, 47(1054), 1979. 93, 94

[203] John B. Goodenough. Theory of the Role of Covalence in the Perovskite-Type Manganites [La,M(II)]MnO_3. *Phys. Rev.*, 100(564), 1955. 93

[204] John B. and Goodenough. An interpretation of the magnetic properties of the perovskite-type mixed crystals $La_{1-x}Sr_xCoO_3$. *Journal of Physics and Chemistry of Solids*, 6(287), 1958. 93

[205] Junjiro and Kanamori. Superexchange interaction and symmetry properties of electron orbitals. *Journal of Physics and Chemistry of Solids*, 10(87), 1959. 93

[206] Masanobu Sonobe and Kichizo Asai. Magnetization Measurement and ^{55}Mn NMR Study of $La(Ni_{1-x}Mg_x)_{0.5}Mn_{0.5}O_3$. *Journal of the Physical Society of Japan*, 61(4193), 1992. 94, 95

[207] M. C. Sánchez, J. García, J. Blasco, G. Subías, and J. Perez-Cacho. Local electronic and geometrical structure of $LaNi_{1-x}Mn_xO_{3+\delta}$ perovskites determined by x-ray-absorption spectroscopy. *Phys. Rev. B*, 65(144409), 2002. 94, 95

[208] R. F. W. Bader. *Atoms in Molecules - A Quantum Theory.* Oxford University Press, 1990. 94, 99

[209] W. Tang, E. Sanville, and G. Henkelman. A grid-based Bader analysis algorithm without lattice bias. *J. Phys.: Condens. Matter*, 21(084204), 2009. 94, 99

[210] E. Sanville, S. D. Kenny, R. Smith, and G. Henkelman. An improved grid-based algorithm for Bader charge allocation. *J. Comp. Chem.*, 28(899), 2007. 94, 99

[211] G. Henkelman, A. Arnaldsson, and H. Jónsson. A fast and robust algorithm for Bader decomposition of charge density. *Comput. Mater. Sci.*, 36(254), 2006. 94, 99

[212] Korotin Dm., Kozhevnikov A., Skornyakov S., Leonov I., Binggeli N., Anisimov V., and Trimarchi G. Construction and solution of a Wannier-functions based Hamiltonian in the pseudopotential plane-wave framework for strongly correlated materials. *The European Physical Journal B - Condensed Matter and Complex Systems*, 65(91), 2008. 94, 103

[213] Perdew John P., Burke Kieron, and Ernzerhof Matthias. Generalized Gradient Approximation Made Simple. *Phys. Rev. Lett.*, 77(3865), 1996. 94

[214] Hena Das, Umesh V. Waghmare, T. Saha-Dasgupta, and D. D. Sarma. Electronic Structure, Phonons, and Dielectric Anomaly in Ferromagnetic Insulating Double Pervoskite La_2NiMnO_6. *Phys. Rev. Lett.*, 100(186402), 2008. 94

[215] Rogado N. S., Li J., Sleight A. W., and Subramanian M. A. Magnetocapacitance and Magnetoresistance Near Room Temperature in a Ferromagnetic Semiconductor: La_2NiMnO_6. *Advanced Materials*, 17(2225), 2005. 95, 96

[216] Wannier Gregory H. The Structure of Electronic Excitation Levels in Insulating Crystals. *Phys. Rev.*, 52(191), 1937. 100

[217] Nicola Marzari and David Vanderbilt. Maximally localized generalized Wannier functions for composite energy bands. *Phys. Rev. B*, 56(12847), 1997. 100

[218] Ku Wei, Rosner H., Pickett W. E., and R. T. Scalettar. Insulating Ferromagnetism in $La_4Ba_2Cu_2O_{10}$: An *Ab Initio* Wannier Function Analysis. *Phys. Rev. Lett.*, 89(167204), 2002. 100

[219] Dmitri Volja, Wei-Guo Yin, and Wei Ku. Charge ordering in half-doped manganites: Weak charge disproportion and leading mechanisms. *EPL*, 88(27008), 2010. 101

[220] A. V. Boris, Y. Matiks, E. Benckiser, A. Frano, P. Popovich, V. Hinkov, P. Wochner, M. Castro-Colin, E. Detemple, V. K. Malik, C. Bernhard, T. Prokscha, A. Suter, Z. Salman, E. Morenzoni, G. Cristiani, H.-U. Habermeier, and B. Keimer. Dimensionality Control of Electronic Phase Transitions in Nickel-Oxide Superlattices. *Science*, 332(937), 2011. 107, 108, 109, 110

[221] Jian Liu, S. Okamoto, M. van Veenendaal, M. Kareev, B. Gray, P. Ryan, J. W. Freeland, and J. Chakhalian. Quantum confinement of Mott electrons in ultrathin $LaNiO_3/LaAlO_3$ superlattices. *Phys. Rev. B*, 83(161102), Apr 2011. 107, 108, 112

[222] J. Liu, M. Kareev, S. Prosandeev, B. Gray, P. Ryan, J. W. Freeland, and J. Chakhalian. Effect of polar discontinuity on the growth of $LaNiO_3/LaAlO_3$ superlattices. *Appl. Phys. Lett.*, 96(133111), Apr 2010. 107, 108, 112

[223] J.M. Ziman. *Electrons and Phonons.* Oxford Unversity Press (London), 2001. 108, 112

[224] Georg K.H. Madsen and David J. Singh. BoltzTraP. A code for calculating band-structure dependent quantities. *Computer Physics Communications*, 175(67), 2006. 108

[225] Jiří Chaloupka and Giniyat Khaliullin. Orbital Order and Possible Superconductivity in $LaNiO_3/LaMO_3$ Superlattices. *Phys. Rev. Lett.*, 100(016404), 2008. 108, 111

[226] P. Hansmann, Xiaoping Yang, A. Toschi, G. Khaliullin, O. K. Andersen, and K. Held. Turning a Nickelate Fermi Surface into a Cupratelike One through Heterostructuring. *Phys. Rev. Lett.*, 103(016401), 2009. 108, 111, 112

[227] A. Filippetti, P. Delugas, M. J. Verstraete, I. Pallecchi, A. Gadaleta, D. Marré, D. F. Li, S. Gariglio, and V. Fiorentini. Thermopower in oxide heterostructures: the $SrTiO_3/LaAlO_3$ interface. *Phys. Rev. Lett*, submited, 2011. 108

[228] V. Yu. Irkhin and A. A. Katanin. Critical behavior and the néel temperature of quantum quasi-two-dimensional heisenberg antiferromagnets. *Phys. Rev. B*, 55(12318), 1997. 110

[229] Andrew Zangwill. *Physics at Surfaces.* Cambridge University Press (Cambridge), 1988. 111

[230] Blanca-Romero, Ariadna, and Pentcheva Rossitza. Confinement-induced metal-to-insulator transition in strained $LaNiO_3/LaAlO_3$ superlattices. *Phys. Rev. B*, 84(195450), 2011. 111

[231] P. Hansmann, A. Toschi, Xiaoping Yang, O. K. Andersen, and K. Held. Electronic structure of nickelates: From two-dimensional heterostructures to three-dimensional bulk materials. *Phys. Rev. B*, 82(235123), 2010. 112

[232] G. Colizzi, A. Filippetti, and V. Fiorentini. Multiferroicity and orbital ordering in $Pr_{0.5}Ca_{0.5}MnO_3$ from first principles. *PRB*, 82(140101), 2010. 118